Localization Error Bounds For 5G mm-Wave Systems Under Hardware Impairments

by

Fariba Ghaseminajm

A thesis presented to Lakehead University
in fulfillment of the thesis requirement for the degree of
DOCTOR OF PHILOSOPHY
in Electrical Engineering

Thunder Bay, Ontario, Canada, 2022

To Love of my life, Steve
and
my dear parents.

Declaration

I hereby declare that I am the sole author of this thesis. This is a true copy of the thesis, including any required final revisions, as accepted by my examiners. Most of this work has either been published or submitted in order to be published as a journal. The publications are listed as below.

Journal Publications

- F. Ghaseminajm, Z. Abu-Shaban, S. S. Ikki, H. Wymeersch and C. R. Benson, "Localization Error Bounds for 5G mmWave Systems Under I/Q Imbalance," *IEEE Transactions on Vehicular Technology*, vol. 69, no. 7, pp. 7971-7975, July 2020, doi: 10.1109/TVT.2020.2991377.
- F. Ghaseminajm, M. Alsmadi, S. S. Ikki, "Error Bounds for Localization in *mm*Wave MIMO Systems: Effects of Hardware Impairments Considering Perfect and Imperfect Clock Synchronization," Accepted in *IEEE systems journal*.
- F. Ghaseminajm, M. Alsmadi, S. S. Ikki, "RIS-aided Mobile Localization Error Bounds Under Hardware Impairments," Submitted in *IEEE Transaction on Vehicular Technology*.

Conference Publication

- F. Ghaseminajm, E. Saleh, M. Alsmadi and S. S. Ikki, "Localization Error Bounds For 5G mmWave Systems Under Hardware Impairments," *IEEE 32nd Annual International Symposium on Personal, Indoor and Mobile Radio Communications* (PIMRC), 2021, pp. 1228-1233, doi: 10.1109/PIMRC50174.2021.9569299.

Abstract

Localization and location aware systems are expected to be counted as one of the main services of 5G millimeter wave (mmWave) communication systems. mmWave communication systems are offering a large bandwidth from 30-300 GHz frequency band along with low latency communications. Although, they use massive number of antennas at their transmitters and receivers, their transceivers occupy a very small area, in order of centimeters. These features make 5G mmWave communication systems an exceptional candidate for the localization services. However, mmWave suffers from some limitations such as high vulnerability to the environment and hardware deficiency.

The hardware used in mmWave system's transceivers including power amplifiers and analog/digital converters, cannot be manufactured perfectly as of high costs. Therefore, it is highly probabilistic to see a non-linear behavior coming out of the mmWave transceivers, known as hardware impairments (HWIs). HWIs is generally caused as a result of non-linearity of transmitter power amplifier and receiver low noise amplifier (LNA) as well as analog to digital (ADC) and digital to analog converters (DAC). Moreover, HWIs is the general form of phase noise and In/Quadrature phase (I/Q) imbalance. Because of the mmWave's nature, even a slight shortcoming can cause severe effects on its performance. This thesis investigates the possible effects of HWIs on the user localization error bounds. Towards that and focusing on line-of-sight (LOS) path, we derive the Cramèr-Rao Lower Bound (CRLB) for the user equipment (UE)'s location and orientation by starting with a conventional two dimension (2D) scenario and then, we extend it to the realistic three dimensional (3D) scenario. Afterwards, by adding another deficiency, we examine the effect of HWIs on user localization under asynchronous conditions. In order to eliminate the time bias between the transmitter and the receiver, we pursued our goal for four other scenarios, categorized as one-way (OWL) and two-way localization methods (TWL). Each of these two, follow different approaches for cancelling the bias; the first one uses a second base station (BS) and the second one utilizes the both forward and backward transmissions. Two algorithms round trip (RLP) and collaborative localization protocols (CLP) are studied in TWL. Finally, in an effort to alleviate the enormous effects of HWIs on user localization, we explore the advantages of reconfigurable intelligent surfaces (RISs).

Our results show that HWIs have a strong effect on UE's localization. For each mentioned scenario, position (PEB) and orientation error bounds (OEB) of the UE stand at their minimum level, when there are no HWIs. Moreover, comparing different scenarios reveal that CLP has the finest performance facing HWIs. Through our findings, we confess that establishing few optimum spaced RISs give a lot of benefits to the localization performance.

Acknowledgements

First and foremost, all the praise belongs to God, who has always given me countless blessings and patience to make me moving forward. Besides, the success of this thesis would not be possible without support and guidance of many people. For this reason, I would like to express my gratitude and appreciation to each of them:

- My supervisor Prof. Salama Ikki for his continuous and tremendous support starting the application procedure and during each day of my Ph.D program and related research; without his patience, motivation, and immense knowledge, this would have not been done. I appreciate him for all the confidence and guidance, he has given me.

- My research collaborator, Dr. Malek Alsmadi, who has guided me with his constructive opinions, suggestions and feedback. His support helped me to become an independent researcher.

- Dr. Zohair Abu-Shaban, my previous research collaborator, for giving me the interest and attentiveness to the subject of this thesis. His timely support and feedback helped me digesting the research topic.

- My colleagues and classmates for their passionate advice and inspirations. Also, The Lakehead University for providing a remarkable environment for me and my research team being able to grow and advance.

- My strong and exceptional parents, Mina and Ali, and my sisters, for their endless and unparalleled love, help and support. I am always been indebted to them for giving me the chance to chase my dreams.

- Last but not least, my soulmate, Steve, for his daily support and cherish. His non-stop emotional words and being proud of me, were the reasons of my efforts.

Table of Contents

List of Figures

Chapter 1

Introduction

1.1 Millimeter wave communication and its limitations

It's been always a challenge to provide communication services to the rapidly growing number of users; as per Cisco annual internet report in March 2020, the number of internet users will reach to 5.3 billion users in 2023 [2]. Moreover, some studies revealed that the data traffic is expected to need 5000 times more capacity [3, 4], in which the current radio technologies are not capable to offer this capacity; this increasing demands strongly depends on spectral efficiency and bandwidth [5]. Therefore, a wide-range spectrum band is required, such as *millimeter wave (mmWave)* bands (30 GHz- 300 GHz). Communication at mmWave frequencies has opened a new stage in wireless communication system. Large-scale spectrum in this band leads to having larger bandwidth channel and consequently, higher data rate [6]. Moreover, mmWave supports establishing massive number of small antennas at the transceiver, resulting in more sophisticated multiple-input multiple-output

(MIMO) communication systems. Large antenna arrays' deployment creates narrow beams which highly interact with atmospheric constituents like Oxygen (O_2). In brief, some of the benefits and drawbacks of mmWave communication system are following.

- Large bandwidth in mmWave channels secures 1 Gbps data rate.
- mmWave provides low latency communication [7].
- It has low scattering nature which results in sparse channel with few paths [8, 9]. This means mmWave is rather influenced by line-of-sight (LoS) than non line-of-sight (NLOS) path.
- mmWave channels are sensitive to the blockage.
- Manufacturing small antennas requires more precision and cost [3,10,11]. Practically, these productions lead to some minor imperfections.
- Due to atmosphere absorption, mmWave transceivers cover a small range in order of few Kilometers [12, 13].

The energy and bandwidth efficiency of mmWave communication makes it an exceptional candidate for the fifth generation (5G). On the other hand, localization (i.e. finding the position and orientation of the user equipment (UE)) is one the main services of 5G, owing to deploying large number of antennas and the large bandwidth; these two key factors facilitate the location estimation process and consequently lead to [14]

1. Accurate localization using a single anchor [15–17]
2. Exploiting of enormous location aware applications such as vehicular communication [18, 19], smart health systems and target based applications [20].

3. Boosting network performance and beamforming schemes if the signal is directed to the user location [21–23].

1.2 Localization Evolution

Finding the location was one of the main concerns in the history of civilization. Early men used marked landscapes, such as mountains and shores. Later, sun and stars' observation using appropriate instruments became the most important sources for the location information.

Human's vast effort in order to discovering their location, pushed them towards to today's localization, which is using more complicated measurements to achieve the accurate position. In 1906, the Stone Radio and Telegraph Company accomplished the first attempt by installing the first navigation prototype on an American naval ship [24]. Later on, in 1962, USA made the first satellite navigation system, which could localize the user with the accuracy of almost 25 meters [25]. Subsequently, Global Positioning System (GPS) was the result of USA's effort in 1985 [26].

It has been few decades that localization is used in indoor and outdoor applications such as localization in emergency calls [27, 28], travel, asset management, shopping, workforce management and billing. Nowadays, localization is known as one of the main services of 5G mmWave communication systems and this fact is taking an anourmous attention [29–31] and a lot of companies such as Huawei [32], Nokia [33] and Ericsson [34] have launched their 5G networks. In the following section the techniques used in order to accomplish localization are explained in details.

1.3 Localization techniques

As it's mentioned before, localization is one of the main services of 5G mmWave communication systems. The goal in localization is to determine the position and orientation of an agent using single or multiple anchors. In this thesis, *agent* represent the UE with an unknown position and *anchor* is the device with a known location, attempting to locate the UE, i.e. base station (BS). The localization procedure can be done with variety of techniques through the earned data from beamforming [35], pilot assignment [36] and resource allocation [37].

Localization techniques can be categorized in different points of view as below [14,38,39].

1. **Localization methods:** The position of an agent can be estimated through some metrics. These metrics can be dependent to the distance parameter; in this case the localization is called *range-based*. For those techniques that the localization procedure does not rely on the distance, the method is called *range-free*. In the following, different range-based and range-free localization techniques are described.
    - **Range-free localization techniques:** There are two main categories in this type of localization:
        (a) **Fingerprinting:** This method is based on a prior entries in a database and mostly used in indoor circumstances. Some location based parameters such as the received power, are measured and collected from all the available agents during the training step. In the second step, positioning phases, the location of the agent is recognized by comparing, matching and mapping of the current metrics with the available database. This method suffers from some drawbacks including the time is needed for the matching process as

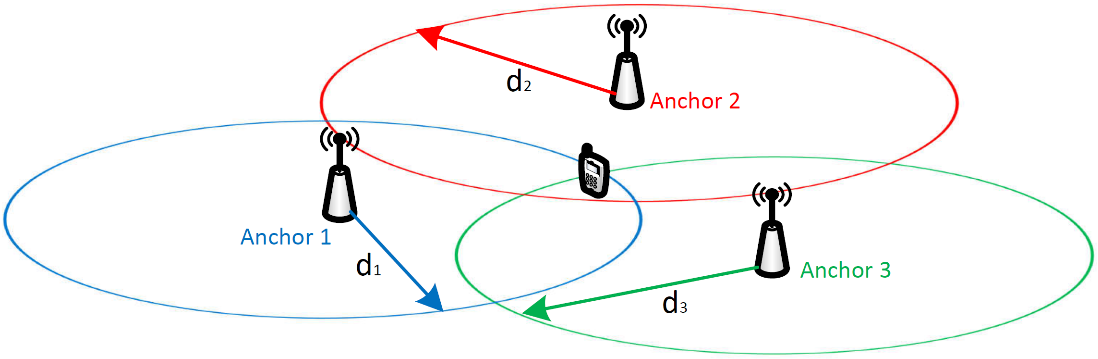

Figure 1.1: Range based localization using RSS or ToA.

well as changing the database due to the training phase changes.

(b) **Hop count:** Using a routing protocol, instead of other metrics, the number of hops from the anchors is counted by the agent. Consequently, the closest anchor is considered as a reference for the positioning. More details on hop count is available in [40].

- **Range-based localization techniques:** In this type of localization some distance related measurements is obtained. There are three main categories in range-based localization, including received signal strength (RSS), direction based localization and time based localization. These metrics' measurements are explained below.

  (a) **RSS** is one of the common localization methods in which the range of the agent is determined based on the received power. Moreover, a minimum of three anchors are needed in order to estimate the agent's position (see Fig. 1.1). Some of the applications which use this method are including mobile handover, resource allocation and RFID.

  (b) **Direction based localization:** Angle of arrival (AoA) estimation is one

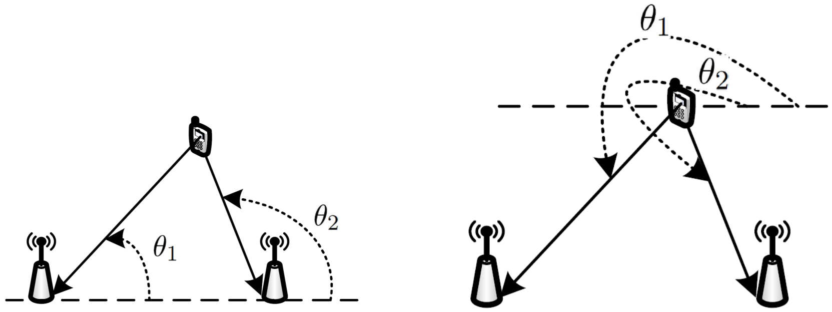

(a) Angle of arrival localization

(b) Angle of departure localization

Figure 1.2: Direction based localization technique.

of the localization methods in which the direction of the received signal at the receiver is measured. This technique, requires two or more antennas in the anchor or at least two single antenna anchors. As in Fig. 1.2a, the AoA and the possible UE's position is then determined through the intersection of lines of bearing (LoB) (Lines from multiple antennas/anchors to the receiver).

Angle of departure (AoD) is another direction based localization in which the direction of the departed signal from the transmitter is estimated (see Fig. 1.2b).

(c) **Time based localization:** Time of arrival (ToA) and time difference of arrival (TDoA) are two localization methods based on time. Both of these methods require synchronization between all the anchors, however the synchronization between the agent and the anchors is not required in TDoA. In ToA, three anchors derive the agent's range d_i, based on the signal delay τ_i; consequently, similar to the RSS in Fig. 1.1, the agent's location is estimated. In case of asynchronized transceivers, TDoA is preferred. In

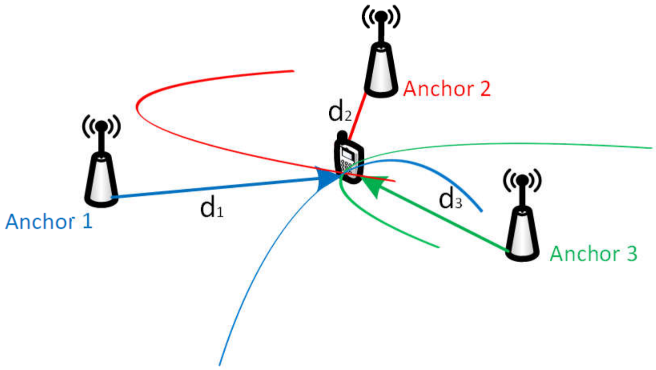

Figure 1.3: Time difference of arrival localization technique.

TDoA, after selecting one anchor as a reference point, the difference between the reference anchor's ToA and other anchors' ToA, is calculated, i. e, $\Delta\tau_{\mathrm{i}} = (\tau_{\mathrm{i}} - B) - (\tau_{\mathrm{Reference}} - B)$; in which B, the clock bias, will be disappeared. The intersection of three hyperbolas out of TDoA, locates the agent (Fig. 1.3).

(d) **Hybrid localization technique:** combination of the direction and time based localization called *hybrid localization*. In this technique, the range of the target is determined by time based localization such as ToA. ToA obtains a sphere/circle range for the target in 2 dimension (2D)/3D scenarios. Then, by estimating an angle using the same anchor and through direction based technique, the agent's location is found. In the other words, the position is the intersection of the line earned out of the angle estimation and the sphere/circle obtained by the range estimation (see Fig. 1.4).

2. **Agent cooperation:** In localization procedure agents can have passive or active roles. When the agent is acting passive role, it does not participate in the localization procedure, however in active mode, the agent is determining some measurements to

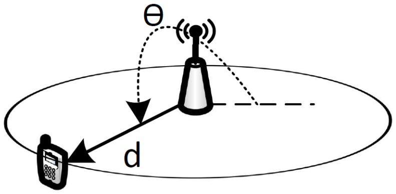

Figure 1.4: Hybrid localization technique using combination of direction and time based localization.

assist the position estimation. In the other words, there are signal exchanging in active mode which can be done uplink or downlink. In uplink, the anchor and in downlink, the agent performs the estimation calculations.

3. **Processing assumptions:** In the estimation procedure, sometimes, the probability density function (PDF) information is not employed and some methods such as least squares performs the estimation. In contrary, in some approaches, PDF of the received noise is deterministic and is considered as a prior knowledge profiting the positioning.

4. **User environment:** There are two environments in which the localization is processed: indoor and outdoor. In indoor positioning, in most of the cases, LOS path is blocked and the active localization is required. Instead, in outdoor scenarios, LOS plays a dominant role in positioning.

5. **Agent's gesture:** In the localization scenario the agent can be immobilized or mobilized. Localization in case of a mobile agent is known as *tracking*.

A summary of these classifications is presented in Fig. 1.5.

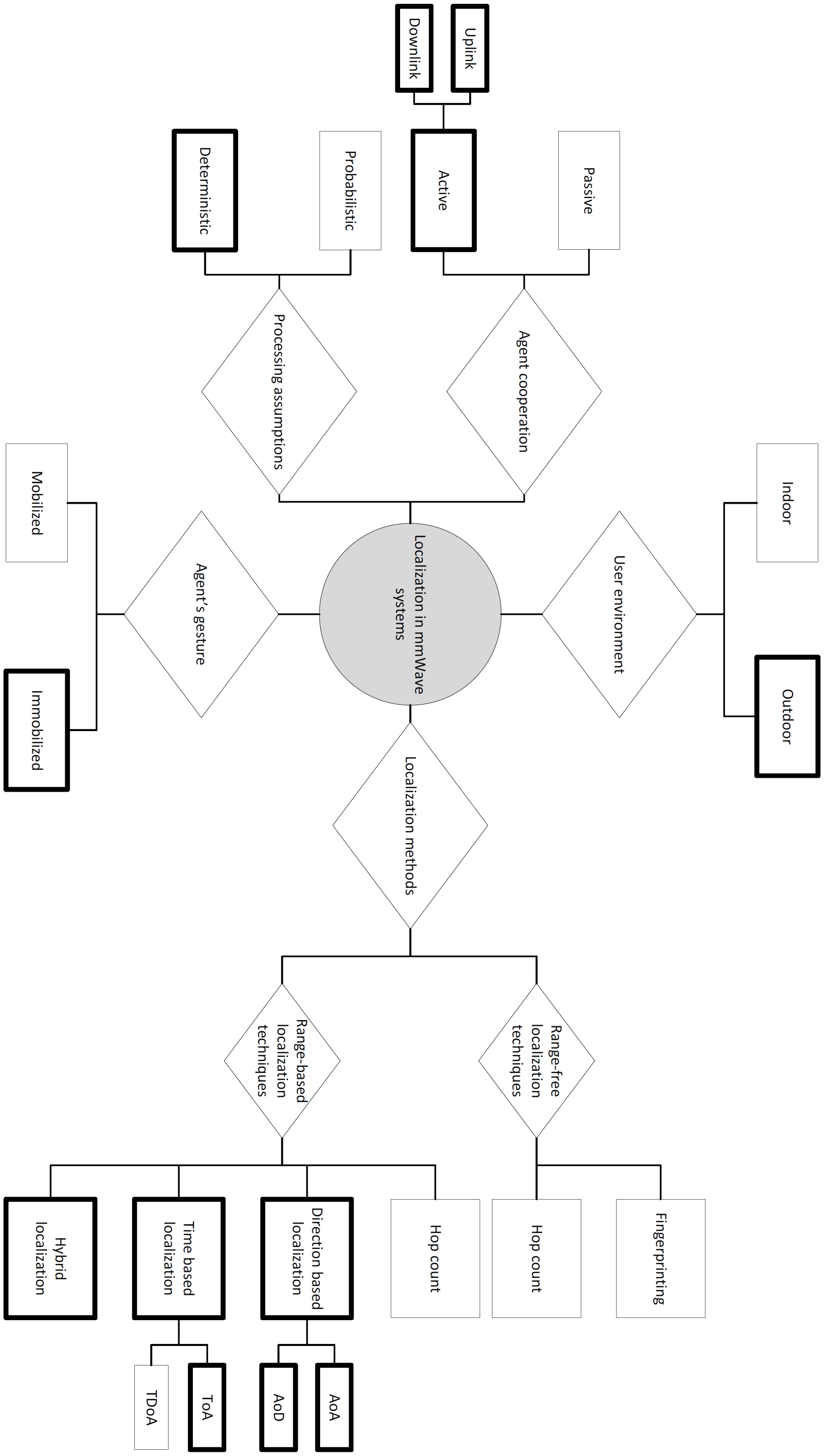

Figure 1.5: Classification of localization in different point of views. Thickened borders boxes are the ones considered in this thesis.

1.3.1 Localization challenges

From the previous sections, it is obvious that the accurate estimation of the agent's location is tremendously dependent on the channel specifications measurement such as AoA, AoD and ToA. However, some deficiencies such as any kind of impairments in the transceivers deteriorate the accurate channel estimation and consequently the location of the agent. In the following section, we discuss about different types of impairments that the localization system may face.

1.4 Classification of transceiver impairments

As we have explained so far, although mmWave communication systems offer higher data rate and larger spectrum, practical implementation of its hardware encounter enormous challenges and limitations in comparison with the sub-6 GHz communication systems; this is due to operating at higher frequency in mmWave than radio frequency (RF)-based systems. For instance, larger multiplication factors induced by higher frequencies escalate the phase noise and then path loss. Another example can be related to the high directionality of the mmWave beams causing higher penetration loss [41]. These constraints can lower the signal-to-noise ratio (SNR) and cause inefficiencies in the system's performance such as localization. In the following, we present an overview of these transceiver impairments.

- **Phase noise**

  Clock signals at the transmitter and receiver is generated by one of the important components of wireless communication systems, oscillators [42]. In mmWave orthogonal frequency division multiplexing (OFDM) communication systems, thermal noise can cause imperfections in the employed oscillators [43]. This can cause a time-varying drift and then frequency deviations which is referred to as *phase noise (PN)* [44]. PN is often seen in higher frequencies oscillators, like mmWave (30-300 GHz), as it is much harder to stabilize the oscillator. Moreover, PN results in phase rotation from one signal to another in the constellation. The effects of PN on OFDM communication systems are deeply studied in [45–52].

- **Nonlinear power amplifiers**

  Power amplifiers (PAs) are in charge of boosting power level of the transmitted signal in order to overcome the possible path loss. If we consider a PA as a filter, ideally more input power generates more output power and there is a linear relationship between the input and output power. However, this is not practical. In practice, in low level of input power, PA acts as a linear filter; as the input power increases and reaches to the threshold point, PA saturates; this causes non-linearity in the PA and distortions in amplitude and phase of the output signal. Nonlinear PAs' deterioration can be classified in two categories: amplitude modulation/amplitude modulation (AM/AM) and amplitude modulation/phase modulation (AM/PM) [42]. The first one discusses the input and output signal's amplitude relationship and the latter describes the input signal's amplitude and output signal's phase relationship.

- **I/Q imbalance**

  Quadrature amplitude modulation (QAM) is widely used in modern communication systems, particularly mmWave systems. In this modulation, in-phase (I) and quadrature (Q) components should be perfectly matched; this means, the phase difference between two I and Q branches should be 90° and also the signal's amplitude out of two branches should be consistent. However, due to limited accuracy in practical systems, a perfect match is rarely possible. This is known as *I/Q imbalance* and leads to performance degradation, including positioning. I/Q imbalance is usually modelled based on two types: frequency-independent model which examines quasi-linear impairments of the input signal and frequency-selective model which evaluates the analog components' behavior more precisely [42]. The effect of I/Q imbalance (IQI) on positioning was studied previously in several papers. For example, [53] uses time reversal for positioning based on channel impulse response (CIR) or channel frequency response (CFR). In this method, a database of fingerprints information is built and based on the correlation between results of CIR (or CFR) and the ones in the database, location is estimated.

- **Antenna array calibrations**

  Positioning using angular determination as AoA and AoD localization methods, requires antenna arrays. Ideally, for accurate positioning, the electrical and geometrical characteristics of the antennas in the array must be known. In practice, however, these features may alter over the time and it is not feasible to maintain each factor as designed. This necessitates a process called *antenna calibration* [54]. This process can be done by transmitting the known pilots from known locations [55].

- **Doppler effect**

  This impairment is applied in scenarios in which the agent is moving and is not stationary. The agent's motion with respect to the anchor makes a distortion called *Doppler effect*, which in turn causes fast time-varying multi path fading channel and issues in frequency synchronization. It worth mentioning that the Doppler effect in vehicular applications is much more worse than cellular scenarios [56]. A lot of articles such as [57–59] use different tracking methods to alleviate the distortion caused by Doppler effect.

- **Timing synchronisation**

  In most of the localization methods, the transmitter and the receiver is assumed to be synchronized. However, there is often a time offset between the transceivers, affecting the estimation procedure. Estimating the signal's delay is intensively dependent on the present clock offset. Although, this issue is mostly neglected in the literature, some papers such as [60, 61] proposed different methods for eliminating the effect of time asynchronism.

All of the mentioned deficiencies can cause either multiplicative or additive distortions at the received signal and can be generalized as *Hardware impairments (HWIs).* This thesis considers the general HWIs as the main distortion.

1.5 Thesis scope and overview

Although the effect of HWIs on different aspects of mmWave communication systems have been actively studied over the past decades, its effect on localization in different scenarios has not been discovered yet. Focusing on outdoor localization with an immobilized UE in 5G mmWave communication systems, this thesis examines and discuses the effect of HWIs on UE localization in different scenarios. In the other words, in each scenario the error bounds for UE location estimation with respect to the hardware deterioration is found. Moreover, this study provides a deep understanding of the factors which can alleviate the worsening effects of HWIs in order to be exploited for betterment and improvement of 5G communication systems design and even more, 6^{th} generation constitution.

The main contribution of this thesis is to show the disturbing consequences of having a minor malfunction in the hardware used in the transceivers. By examining this, our goal is to provide the algorithms and elements that need to be considered and reviewed to attain the high accuracy in UE positioning such as utilising reconfigurable intelligent surfaces (RISs). The considered localization scenario in this thesis, is based on the thickened boxes in Fig. 1.5. In brief, the calculations in this thesis is achieved for the active immobilized UE in an outdoor localization scenario using deterministic hybrid localization.

Research contributions

The research provided in this thesis is pursuing the following contributions:

1. Exploring the effect of HWIs on UE position and orientation error bounds in uplink two dimensional (2D) scenario.
2. Analyzing the effect of HWIs on UE localization in one way uplink localization using one anchor under perfect synchronization in 3D scenario.
3. Analyzing the effect of HWIs on UE localization in one way uplink localization using two anchors under imperfect synchronization in 3D scenario. The second anchor is used to eliminate the clock offset.
4. Analyzing the effect of HWIs on UE localization in two way localization (uplink and downlink transmissions) using round-trip localization protocol (RLP) under imperfect synchronization in 3D scenario. RLP is a protocol in which UE is contributing in its localization by estimating the ToA.
5. Analyzing the effect of HWIs on UE localization in two way localization using collaborative localization protocol (CLP) under imperfect synchronization in 3D scenario. CLP is a protocol in which UE is contributing in its localization by estimating the AoA, AoD and ToA.

6. Analyzing the alleviation of HWIs effect on UE uplink localization using RISs in 2D and 3D scenarios.

7. Analyzing the effect of number of passive elements in each RIS on improving the localization accuracy affected by HWIs.

8. Analyzing the effect of RIS inter-element space on improving the localization accuracy affected by HWIs.

Thesis Overview

The remainder of the thesis is structured as follows:

- **Chapter 2** obtains the necessary background in order to help clarifying some concepts used in the thesis. These concepts consist of a brief overview on array signal processing such as array manifold vector calculation in different types of antenna array, beamforming concepts including different phased array configuration and analog beamforming, general derivation of received signal model in MIMO systems, a brief revision on HWIs mathematical model and estimation in signal processing using Cramèr-Rao Lower Bound (CRLB). CRLB is a metric commonly used in judging the estimation algorithm. Also, this chapter provides an overview of RISs concept and functionality.

- **Chapter 3** examines the effect of HWIs on UE's position and orientation estimation accuracy. Considering 2D scenario and focusing on LOS path, the signal model affected by HWIs is obtained and after noise covariance calculation, the CRLB for the unknown parameters are achieved. Finally, the degradation for both position and orientation estimation is compared for the oriented and non-oriented UE.

- **Chapter 4** focuses on synchronized and asynchronized scenarios. In this chapter, the effect of HWIs on UE's localization error bounds in 3D scenario considering 5 different cases, has been studied. The first case explores the effect of HWIs on UE localization using a single anchor which is timely synchronized with the UE. While, the second and third cases evaluate the localization accuracy affected by HWIs using two anchors which are not synchronized with the UE. Finally, the fourth and the fifth cases, resolve the synchronization problem by two different algorithms RLP and CLP and study the effect of HWIs on localization performance. At the end, all of the 5 cases are compared to conclude the best resistant algorithm facing HWIs.

- **Chapter 5** studies the improvement of 5G/6G localization accuracy using RISs. Assuming 2D and 3D scenarios and using a single anchor and a Line or a wall of RISs (in 2D and 3D scenarios, respectively), the error bounds of UE localization under HWIs conditions are derived. Then, the effect of number of RISs elements and their distance towards the betterment of localization accuracy, have been examined.

- **Chapter 6** summarizes the important obtained results of the thesis and opens horizon on some future research directions.

Chapter 2

Background Concepts

Overview: The concepts of array signal processing, hardware impairments (HWIs), classical estimation theory and reconfigurable intelligent surfaces (RIS) are used frequently in this thesis. Accordingly, it is worthwhile to cover these concepts in this chapter. The chapter is commenced by providing an overview on the field of array signal processing, in which the concept of antenna array and its array manifold vector is introduced. Next, analog beamforming and the received signal model is provided. Afterwards, the practical non-linearity in hardware and its signal model is explained under hardware impairments (HWIs) section. Finally, calculation of a parameter's lower bound and parameters' transformation are explicated. At the end, an overview of the reconfigurable intelligent surfaces (RISs), a new technology for controlling the scattered and reflected radio waves, is given in the last section.

2.1 Background on array signal processing

One field of signal processing concentrates on array processing. An array consists of a group of sensors acting independently in a specific spatial configuration with the purpose of exploiting their signals. In the context of this thesis, the sensors that we will study are antennas. In array signal processing, there are four issues that need to be addressed [62]. The first issue concerns array configuration consisting of two parts: antenna pattern and array geometry. The second and third issues concern signal and interference structures, respectively and the fourth one is the noise structure (Gaussian for the purposes of this thesis).

There is a myriad of applications for applying these arrays including radars, communications, medical diagnosis, etc. In this section we simply investigate array signal processing in communication with purpose of localization.

2.1.1 Array Manifold Vector

In array design two aspects will be involved: firstly the array geometry, relating to how we place antennas beside each other and, secondly the complex weighting of each antenna. For the first aspect, we need to define the standard coordinate system. From Fig. 2.1, for $0 \leq \theta \leq \pi$, $0 \leq \phi < 2\pi$, and $\rho \geq 0$, we can write

$$x = \rho \sin\theta \cos\phi, \tag{2.1a}$$

$$y = \rho \sin\theta \sin\phi, \tag{2.1b}$$

$$z = \rho \cos\theta. \tag{2.1c}$$

Based on (2.1), we can define a unit vector pointing towards (x, y, z) as below

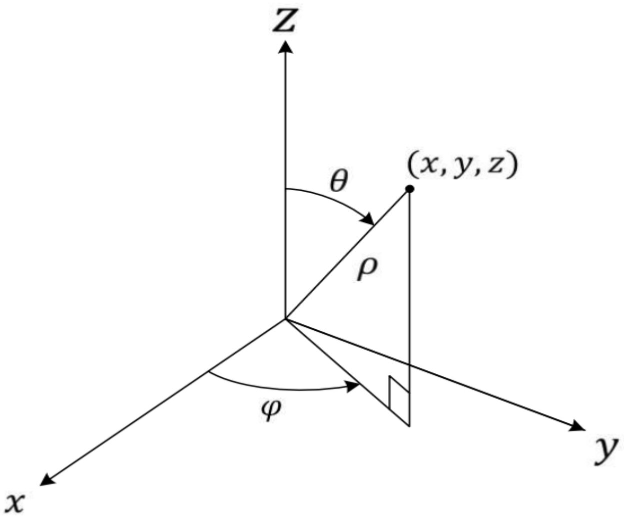

Figure 2.1: Spherical coordinate system

$$\boldsymbol{u} \triangleq [\sin\theta\cos\phi, \sin\theta\sin\phi, \cos\theta]^T,$$

Assuming having N antennas in an array, vector $\boldsymbol{\Delta}$ defines the location of each antenna in the coordinate system as

$$\boldsymbol{\Delta} = [\boldsymbol{u}_1, \boldsymbol{u}_2, ..., \boldsymbol{u}_{\mathrm{N}}] \in \mathbb{R}^{3\times N}, \tag{2.2}$$

in which $\boldsymbol{u}_{\mathrm{N}}$, represents the N^{th} antenna's unit vector.

Finally for an array consisting of isotropic antennas, the array manifold vector can be written as below [17, 62, 63]

$$\boldsymbol{a}(\theta,\phi) \triangleq \begin{bmatrix} e^{-j\boldsymbol{u}_1^{\mathrm{T}}\boldsymbol{k}} \\ \vdots \\ e^{-j\boldsymbol{u}_N^{\mathrm{T}}\boldsymbol{k}} \end{bmatrix} = \exp\left(-j\boldsymbol{\Delta}^{\mathrm{T}}\boldsymbol{k}(\theta,\phi)\right) \in \mathbb{C}^{N\times 1}, \tag{2.3}$$

where $\boldsymbol{k}$ is the wave number and is defined as below

$$\boldsymbol{k}(\theta,\phi) \triangleq \frac{2\pi}{\lambda}\boldsymbol{u} = \frac{2\pi}{\lambda}[\sin\theta\cos\phi, \sin\theta\sin\phi, \cos\theta]^{\mathrm{T}}. \tag{2.4}$$

in which λ is the wavelength. In order to normalize array manifold vector for having $\boldsymbol{a}^{\mathrm{T}}(\theta,\phi)\boldsymbol{a}(\theta,\phi) = 1$, we can write [17]

$$\boldsymbol{a}(\theta,\phi) = \frac{1}{\sqrt{N}}\exp\left(-j\boldsymbol{\Delta}^{\mathrm{T}}\boldsymbol{k}(\theta,\phi)\right). \tag{2.5}$$

The array manifold vector gives all the information about an array including geometry and wave direction [63]. Moreover, the defined array manifold vector will be used for the both transmitter and receiver.

In the following, we demonstrate how to obtain the array manifold vector for example geometries.

- **Planar or Two-Dimensional (2D) Array:**

  In the case of full azimuthal field of view (FOV), that is, $\theta \in [0°, 360°)$, a planar array will be applied. Two popular planar arrays are uniform rectangular array (URA), which is shown in Fig. 2.2 (right) and uniform circular array (UCA) [63].
  The FOV space of a planar array is shown to be

  $$\Omega = \{(\theta,\phi):\ \theta \in [0°, 360°), \phi \in [0°, 90°)\}$$

  In order to find the array manifold vector of the URA shown in Fig. 2.2 with $N = N_xN_z$ antennas, we first need to define the location of each antenna. N_x and N_z are

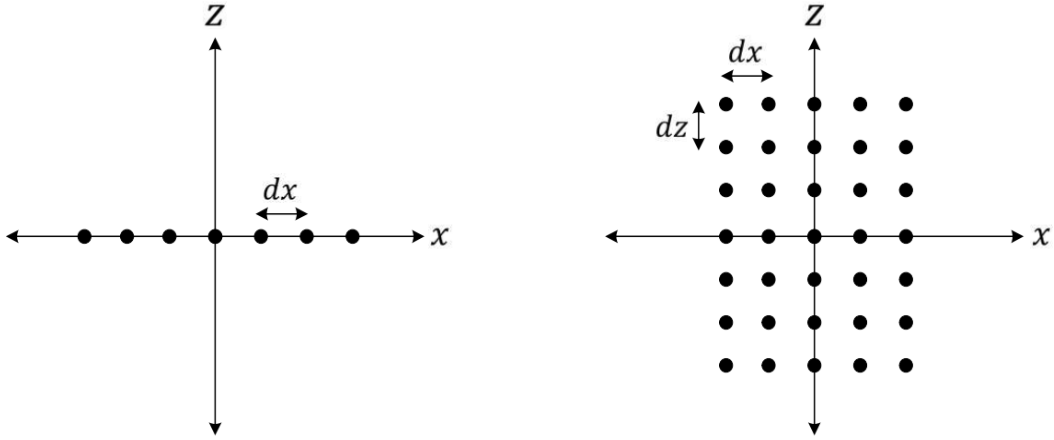

Figure 2.2: Left: ULA with 9 antennas and d_x inter-element spacing. When $d_x = \lambda/2$ it is called SLA. Right: URA with 45 antennas, consisting of 9 ULAs, each with 5 antennas and d_x inter-element spacing. Spacing between adjacent arrays is d_z.

the number of antennas in the x and z axis, respectively.

$$\boldsymbol{\Delta}^{\mathrm{T}} = [d_x \boldsymbol{x}, 0_N, d_z \boldsymbol{z}], \tag{2.6}$$

where

$$\boldsymbol{x} = \mathbf{1}_{N_z} \otimes \tilde{\boldsymbol{x}}, \tag{2.7a}$$

$$\boldsymbol{z} = \tilde{\boldsymbol{z}} \otimes \mathbf{1}_{N_x}, \tag{2.7b}$$

$$\tilde{\boldsymbol{x}} = \left[-\frac{N_x - 1}{2}, -\frac{N_x - 1}{2} + 1, ..., \frac{N_x - 1}{2}\right]^{\mathrm{T}}, \tag{2.7c}$$

$$\tilde{\boldsymbol{z}} = \left[-\frac{N_z - 1}{2}, -\frac{N_z - 1}{2} + 1, ..., \frac{N_z - 1}{2}\right]^{\mathrm{T}}, \tag{2.7d}$$

and $\otimes$ denotes the Kronecker product. Finally, we obtain

$$\boldsymbol{a}(\theta, \phi) = \frac{1}{\sqrt{N}} \exp\left(-j\frac{2\pi}{\lambda}(d_x \sin\theta \cos\phi \boldsymbol{x} + d_z \cos\theta \boldsymbol{z})\right). \tag{2.8}$$

Note that when $d_x = d_z = \lambda/2$, and $N_x = N_z$, the array is referred as a standard square array (SSA).

- **Linear or One-Dimensional Array:**

  The uniform linear array (ULA) is a group of antennas located in one line (see Fig. 2.2 (left)).
  For the ULA in Fig. 2.2, using (2.6) and (2.7) with $N_z = 1$ and $N = N_x$, we can write

  $$\boldsymbol{x} = \tilde{\boldsymbol{x}},\ \boldsymbol{z} = \mathbf{0}_N,\ \theta = \frac{\pi}{2} \tag{2.9}$$

  Therefore, the array response vector is given by

  $$\boldsymbol{a}(\phi) \triangleq \frac{1}{\sqrt{N}} \exp\left(-j\frac{2\pi d_x}{\lambda} \cos\phi \boldsymbol{x}\right). \tag{2.10}$$

  Note that when $d_x = \lambda/2$, the ULA is called standard linear array.

2.1.2 Beamforming

The advantages of array signal processing benefit us to be able to focus the transmission or reception of a signal on some distinct areas by directing the beams electronically rather than mechanically, used in traditional radars. This process called *beamforming*, in which the signal's amplitude and phase are changed at each antenna using complex weight, in such a way that the antenna gain is increased in the desired area.

To steer the main beam of the phased array antenna in mm-wave communication, there are different configurations for placing analog beam-formers. These configurations which are shown in Fig. 2.3 are known as radio frequency (RF) phase-shifting, intermediate frequency (IF) phase-shifting, local oscillator (LO) phase-shifting, and digital beam forming phased arrays [CMOS Phased Array Transceiver] [1]. In this research, we use the first model (RF phase shifting) in which modulation comes after analog beam-forming in the receiver side. RF phase shifting model is commonly used in the literature for studying the behavior of the mmWave communication systems; however other phase shifting models can be studied as a future research.

Analog Beamforming

In MIMO systems, a large number of antennas will be used to achieve more gain in a specific direction; however, as mentioned before, this specific direction will not be gained except by beamforming. In traditional antenna arrays, in order to steer the main beam towards the specific direction, the whole array have being rotated mechanically. Nowadays, by changing the phase of beams in antenna array, we can steer it electronically [64].

Under the simplest form of beamforming, by weighing gain to each antenna uniformly, the radiation pattern of the URA shown in Fig. 2.2, points towards $\theta = \phi = 90°$. Similarly, in the case of ULA along the x-axis, it points towards the broadside direction, $\phi = 90°$ [62].

There are two methods for beamforming; directional beamforming and random beamforming; the former directs the beams uniformly towards the covered area, however the latter spans the covered area randomly. In this thesis, we only consider directional beamforming with constant magnitude however with varying phase.

Generally, in order to steer the beam towards a direction (ϕ_0, θ_0), we can design the

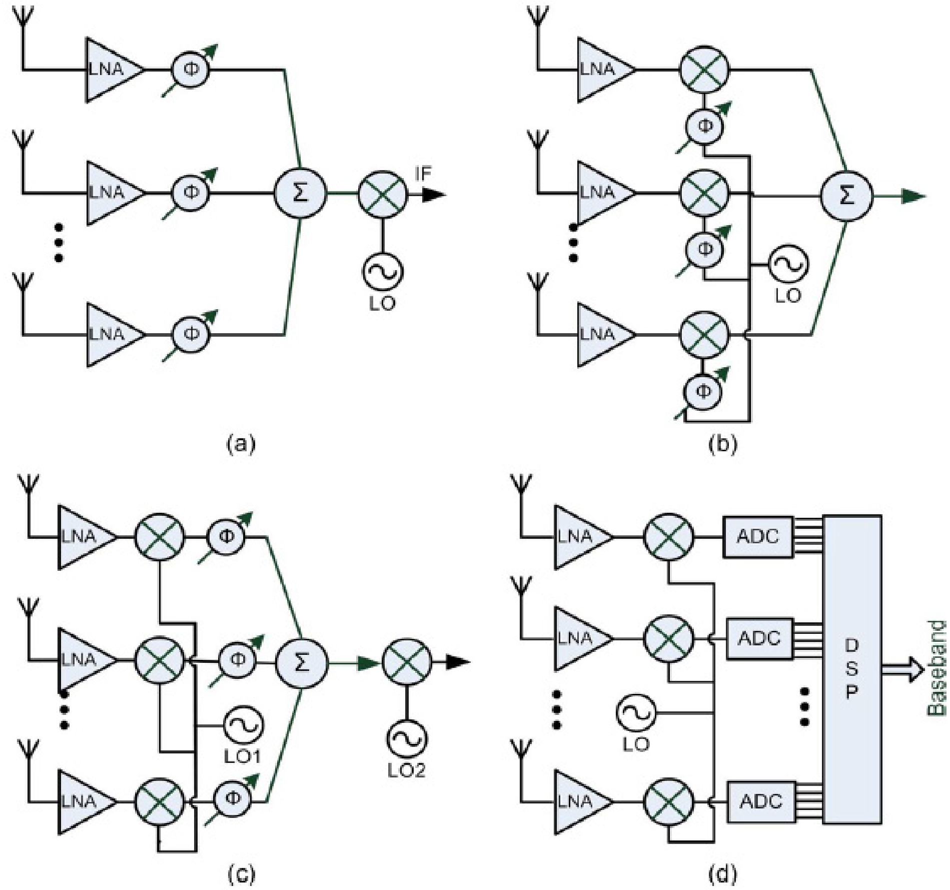

Figure 2.3: Different phased array configurations (a) RF phase-shifting, (b) LO phase-shifting (c) IF phase-shifting, and (d) digital beamforming array [1]

beamforming vector $\boldsymbol{f}$ as below [17]

$$\boldsymbol{f}(\phi_0, \theta_0) = \boldsymbol{a}(\phi_0, \theta_0), \tag{2.11}$$

so that, the beam gain in the direction (ϕ_0, θ_0) is given [62]

$$G(\theta_0, \phi_0) = 20 \log_{10} \left(\frac{\|\boldsymbol{f}^{\mathrm{H}} \boldsymbol{a}(\phi_0, \theta_0)\|}{\|\boldsymbol{f}\|} \right), \tag{2.12}$$

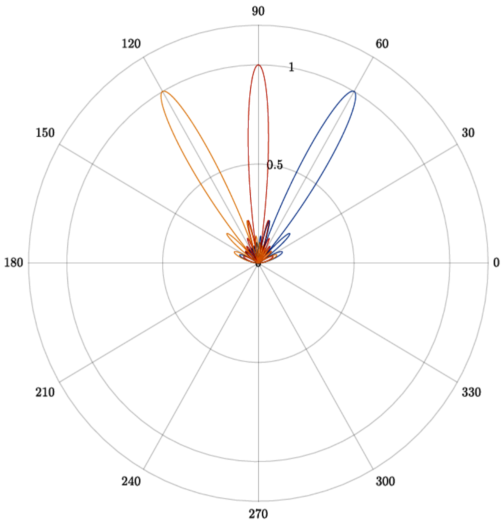

Figure 2.4: Radiation pattern of a 12-antenna ULA, steered to 60°, 90° and 120°

Using (2.12), the polar form of array factor of the 12-antenna ULA is shown in Fig. 2.4; in this figure, the beams are steered towards the directions 60°, 90°, and 120°.

2.1.3 Received signal Model in MIMO system

Considering RF-phase shifting configuration, the end-to-end MIMO channel model is shown in Fig. 2.5. In this subsection, we are going to present the channel model for the line of sight (LOS) path which is used in the rest of the thesis. Based on this model, signal $\boldsymbol{s}(t)$ is going to be transferred via N_{B} beams, through N_{T} antennas at the transmitter. Considering each beam directed towards horizontal and elevation angle $(\phi_{\mathrm{f,b}}, \theta_{\mathrm{f,b}})$, the transmit beamforming can be written as below

$$\boldsymbol{F} = [\boldsymbol{f}(\phi_{\mathrm{f,1}}, \theta_{\mathrm{f,1}}), \boldsymbol{f}(\phi_{\mathrm{f,2}}, \theta_{\mathrm{f,2}}), ..., \boldsymbol{f}(\phi_{\mathrm{f,N_B}}, \theta_{\mathrm{f,N_B}})], \ \in \mathbb{C}^{N_{\mathrm{T}} \times N_{\mathrm{B}}} \tag{2.13}$$

in which $\boldsymbol{f}(\phi_{\mathrm{f,b}}, \theta_{\mathrm{f,b}})$ is the transmit beamforming vector for the b^{th} beam. Finally, the

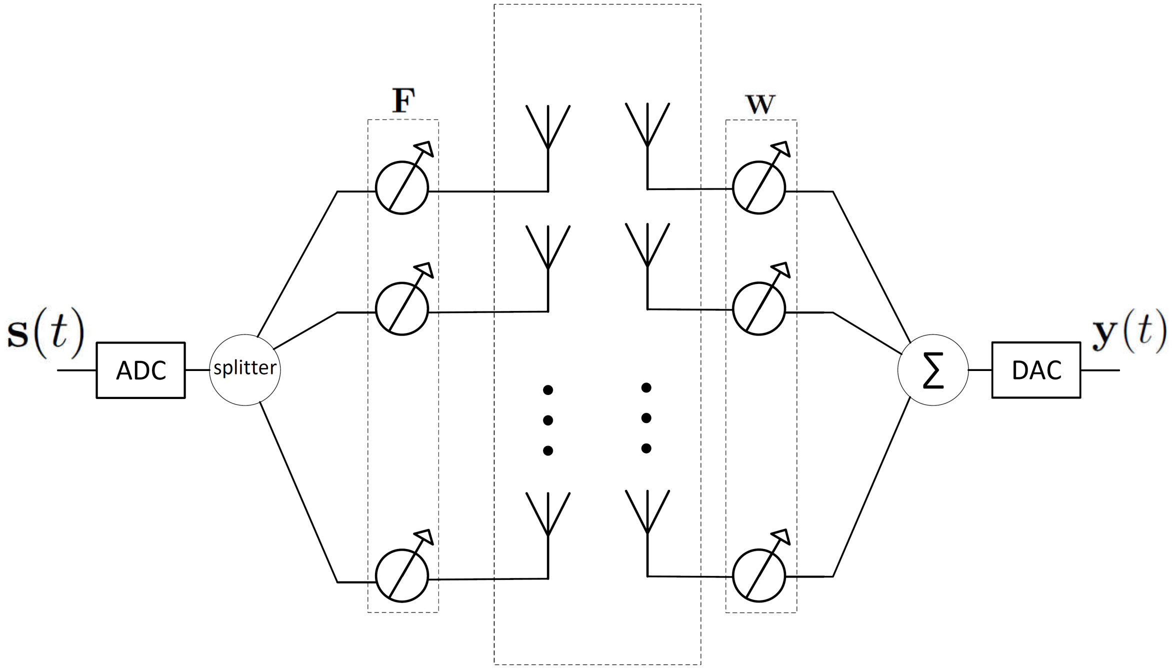

Figure 2.5: RF-phase shifting transceiver model.

signal $\boldsymbol{x}(t)$ is the result of the steered signal at the input of the transmitter antenna.

$$\boldsymbol{x}(t) = \boldsymbol{F}\boldsymbol{s}(t), \ \in \mathbb{C}^{N_\mathrm{T}} \tag{2.14}$$

Consequently, after passing signal $\boldsymbol{x}(t)$ through the transmitter antenna, we earn

$$\tilde{\boldsymbol{x}}(t) = \boldsymbol{a}_\mathrm{T}^\mathrm{H}(\phi_\mathrm{T}, \theta_\mathrm{T})\boldsymbol{F}\boldsymbol{s}(t), \tag{2.15}$$

The arrived signal at the receiver antenna is affected by the propagation delay τ, path gain β and the receiver noise $\boldsymbol{n}(t) \in \mathbb{C}^{N_\mathrm{R}}$. After passing through N_R receiver antennas at the direction $(\phi_{\mathrm{R}}, \theta_{\mathrm{R}})$, we have

$$\boldsymbol{r}_{\mathrm{o}}(t) = \beta \boldsymbol{a}_{\mathrm{R}}(\phi_{\mathrm{R}}, \theta_{\mathrm{R}}) \boldsymbol{a}_{\mathrm{T}}^{\mathrm{H}}(\phi_{\mathrm{T}}, \theta_{\mathrm{T}}) \boldsymbol{F} \boldsymbol{s}(t - \tau) + \boldsymbol{n}(t), \ \in \mathbb{C}^{N_{\mathrm{R}}} \tag{2.16}$$

Finally, the processed signal in direction $(\phi_{\mathrm{R}}, \theta_{\mathrm{R}})$ by the receiver beamformer is

$$\boldsymbol{y}(t) = \beta \boldsymbol{W}^{\mathrm{H}} \boldsymbol{a}_{\mathrm{R}}(\phi_{\mathrm{R}}, \theta_{\mathrm{R}}) \boldsymbol{a}_{\mathrm{T}}^{\mathrm{H}}(\phi_{\mathrm{T}}, \theta_{\mathrm{T}}) \boldsymbol{F} \boldsymbol{s}(t - \tau) + \boldsymbol{W}^{\mathrm{H}} \boldsymbol{n}(t), \ \in \mathbb{C}^{N_{\mathrm{B}}} \tag{2.17}$$

where $\boldsymbol{W} \in \mathbb{C}^{N_{\mathrm{R}} \times N_{\mathrm{B}}}$ is the receiver beamforming matrix and similar to (2.13), it can be written as below

$$\boldsymbol{W} = [\boldsymbol{w}(\phi_{\mathrm{w},1}, \theta_{\mathrm{w},1}), \boldsymbol{w}(\phi_{\mathrm{w},2}, \theta_{\mathrm{w},2}), \ldots, \boldsymbol{w}(\phi_{\mathrm{w},\mathrm{N_B}}, \theta_{\mathrm{w},\mathrm{N_B}})]. \tag{2.18}$$

2.2 Hardware Impairments

In the last section, the received signal has been derived assuming ideal hardware transceiver. In this section, first, we explain the existing hardware non-idealities in practical transceivers, which is known as *hardware impairments (HWIs)*. Secondly, we introduce a model which is reflecting HWIs into the described MIMO system in (2.17). Ideally, the pass-band signal is accurately generated from the base-band signal at the transmitter and the receiver demodulate it precisely. Also, the power amplifier (PA) at the transceiver acts as a linear amplifier; however, in practice, these cannot be fulfilled. The modulator and demodulator at the transmitter and receiver can be asynchronized in time and frequency. plus, the PA amplifies the more strength signals less than the attenuated signals. Moreover, having more ideal hardware leads to consuming more power and expense. These characteristics make the hardware used in the transceiver non-ideal. The HWIs which is considered in this thesis

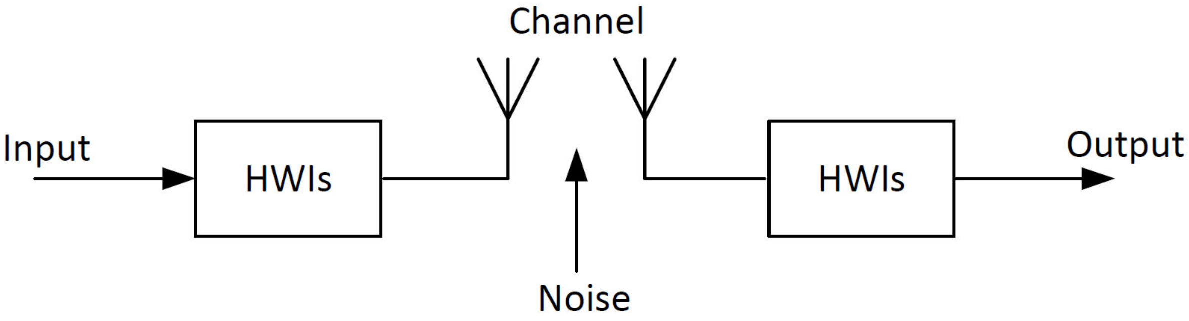

Figure 2.6: Transceiver HWIs model in SISO system.

(see Fig.2.6), is a general model for all the other impairments such as in-phase/quadrature phase (I/Q) imbalance.

2.2.1 Basic modeling for Hardware Impairments

In order to introduce the HWIs model, considering (single-input single-output) SISO system, we assume the input information $x \sim \mathcal{N}_{\mathbb{C}}(0, E)$ is entered to a non-ideal filter (e.g. PA at the antenna) under a non-linear function $g(.)$ [65]. Then, the output y is consisting of the correlation of the output and the input [66] and can be written as below.

$$y = \frac{\mathbb{E}\{yx^*\}}{E} x + \eta_{\mathrm{s}}, \tag{2.19}$$

note that η_{s} is the HWIs' distortion noise and is not the channel noise; the Gaussian noise will be added later at the receiver side. Also, it can be proven that the distortion η_{s} is uncorrelated with x, however it is not independent of the input x. Assuming that using some compensation algorithms, the power of the input and the output are kept the same

$\mathbb{E}\{|y|^2\} = \mathbb{E}\{|x|^2\} = E$, then the HWIs in Fig.2.6 can be modeled as below [65],

$$y = \sqrt{\kappa_\mathrm{s}}x + \eta_\mathrm{s}, \tag{2.20}$$

where $\eta_\mathrm{s} \sim \mathcal{N}_\mathbb{C}(0, (1-\kappa_\mathrm{s})E$ is the additive distortion noise at the transmitter. The dependence of distortion noise power to the signal power E makes η_s different from the receiver noise. Moreover, we take $\kappa \in (0, 1]$; When $\kappa_\mathrm{s} = 1$, then $y = x$ which is an ideal case for the hardware. Note that the HWIs κ_s represents the non-linearity of the PA causing amplitude variation.

Following (2.20), the input signal at the receiver antenna before adding the receiver noise is,

$$y_\mathrm{o} = \beta(\sqrt{\kappa_\mathrm{s}}x + \eta_\mathrm{s}), \tag{2.21}$$

where β is the channel gain. Now, for the receiver side, we need to apply (2.20) once more. So that, we substitute y_o into $r_\mathrm{o} = \sqrt{\kappa_\mathrm{r}}y_\mathrm{o} + \eta_\mathrm{r}$; in which $\kappa_\mathrm{r} \in (0, 1]$ and $\eta_\mathrm{r} \sim (0, (1-\kappa_\mathrm{r})E|\beta|^2)$ are the HWIs factor and the distortion noise at the receiver side, respectively. It's remarkable that, again, the distortion noise power in proportional to the power received at the antenna (i.e. $E|\beta|^2$). Finally, after adding the receiver Guassian noise n, the received signal will be

$$r = \sqrt{\kappa_\mathrm{s}\kappa_\mathrm{r}}\beta x + \sqrt{\kappa_\mathrm{r}}\beta\eta_\mathrm{s} + \eta_\mathrm{r} + n. \tag{2.22}$$

Equation (2.22) can be simply extended for the MIMO systems.

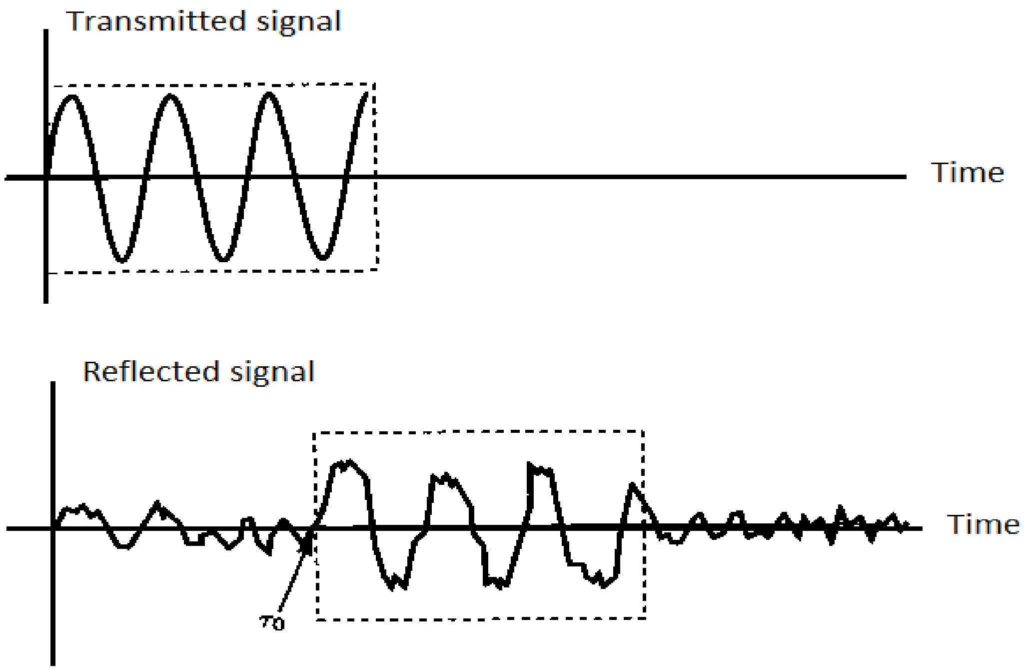

Figure 2.7: Transmitted signal to the aircraft and reflected signal from the aircraft

2.3 Estimation in signal processing

In estimation theory, we try to estimate a group of unknown parameters through some special methods. There are many applications for estimation including radar, image analysis, and sonar; one of the first systems in which estimation was applied. In radar, the aircraft's position is the main desire. To determine the position of the aircraft, radar will send a signal towards the goal and based on the measured delay of reflected signal, the range of the aircraft will be estimated. Fig. 2.7 shows the transmitted and reflected signals. As we can see, the delay can be obtained by the amplitude change in the reflected signal. In the following, we will introduce one of the tools for parameter estimation that works based on probability density function (PDF) of the observation. [67].

2.3.1 Cramèr-Rao Lower Bound (CRLB)

In the context of parameter estimation, a helpful technique for evaluating an estimator is CRLB. Besides, being able to find the lower bound for variance of a parameter (i.e. CRLB) can be used in exploring different system parameters' impact on the overall fulfillment of an estimator. In the next section, we are going to calculate the general CRLB in which the PDF of the parameter depends on the noise PDF. Later on, in the rest of this thesis, CRLB is being used to investigate the effect of HWIs on the performance of the estimators.

Derivation of General Gaussian CRLB

We assume a single sample x

$$x = \theta + w,$$

in which $w \sim \mathcal{N}(0, \sigma^2)$ is the white Gaussian noise. It is desired to estimate an unknown and deterministic parameter θ based on the known observation parameter x. Indeed, the better estimator, the lesser σ^2. CRLB is an estimator that gives the least variance for the unknown parameter θ. The CRLB for a scalar parameter is given by [67]

$$var(\hat{\theta}) \geq \frac{1}{-E[\frac{\partial^2 Lnp(x;\theta)}{\partial\theta^2}]},$$

where $\hat{\theta}$ is an unbiased estimator and $p(x;\theta)$ is the PDF of the observation x. PDF of x is dependent on the noise PDF and is given by

$$p(x;\theta) = \frac{1}{\sqrt{2\pi\sigma^2}} exp[-\frac{1}{2\sigma^2}(x-\theta)^2],$$

Furthermore, the unbiased estimator may be found through

$$\frac{\partial \ln p(x;\theta)}{\partial\theta} = I(\theta)(g(x)-\theta),$$

where $\hat{\theta} = g(x)$ is the estimator and the minimum variance is $\frac{1}{I(\theta)}$; in which, $I(\theta)$ is the *fisher information matrix* (FIM), so

$$I(\theta) = -E[\frac{\partial^2 \ln p(x;\theta)}{\partial\theta^2}],$$

For a vector sample $\boldsymbol{x}$, we assume $\boldsymbol{x} \sim \mathcal{N}(\boldsymbol{\mu}(\theta), \boldsymbol{C}(\theta))$, where $\boldsymbol{\mu}(\theta)$ is the $N \times 1$ mean vector and $\boldsymbol{C}(\theta)$ is the $N \times N$ co-variance matrix. Then, the PDF of the observation $\boldsymbol{x}$ is

$$p(\boldsymbol{x};\boldsymbol{\theta}) = \frac{1}{(2\pi)^{\frac{N}{2}} det^{\frac{1}{2}}(\boldsymbol{C}(\theta))} exp[-\frac{1}{2}(\boldsymbol{x}-\boldsymbol{\mu}(\theta))^T \boldsymbol{C}^{-1}(\theta)(\boldsymbol{x}-\boldsymbol{\mu}(\theta))],$$

in which unknown and deterministic vector $\boldsymbol{\theta} = \begin{bmatrix} \theta_k \\ \theta_l \end{bmatrix}$ is going to be estimated. In this case, the FIM is earned as below

$$[\boldsymbol{I}(\theta)]_{kl} = E[\frac{\partial Lnp(\boldsymbol{x};\boldsymbol{\theta})}{\partial\theta_k}\frac{\partial Lnp(\boldsymbol{x};\boldsymbol{\theta})}{\partial\theta_l}], \tag{2.23}$$

After evaluating (2.23), we will have

$$[\boldsymbol{I}(\theta)]_{kl} = \frac{\partial\boldsymbol{\mu}^T}{\partial\theta_k}\boldsymbol{C}^{-1}(\theta)\frac{\partial\boldsymbol{\mu}}{\partial\theta_l} + \frac{1}{2}\mathrm{tr}\left(\boldsymbol{C}^{-1}(\theta)\frac{\partial\boldsymbol{C}}{\partial\theta_k}\right)\mathrm{tr}\left(\boldsymbol{C}^{-1}(\theta)\frac{\partial\boldsymbol{C}}{\partial\theta_l}\right). \tag{2.24}$$

In chapters 3-5 we will use the obtained result to find the position and orientation bounds.

2.3.2 Transformation of Parameters

In this thesis, in order to derive the lower bounds for the unknown channel parameters, the CRLB is used; however, the interesting parameters are the location elements which are a function of the channel parameters. In consequence, the transformation of parameters is explained in this subsection.

Considering a problem in which the interesting unknown parameters $\boldsymbol{\psi} \triangleq [\psi_1, ..., \psi_{\mathrm{N_S}}]^{\mathrm{T}}$ are a function of the unknown parameters $\boldsymbol{\varphi} \triangleq [\varphi_1, ..., \varphi_{\mathrm{N_P}}]^{\mathrm{T}}$. Also, we assume that, finding the FIM of the parameters $\boldsymbol{\varphi}$ is easier. Then, the FIM of the interesting parameters, $\boldsymbol{J}_{\boldsymbol{\psi}}$, can be earned through the gained FIM of $\boldsymbol{\varphi}$, $\boldsymbol{J}_{\boldsymbol{\varphi}}$, using the following equation [67, 68]

$$\boldsymbol{J}_{\boldsymbol{\psi}} = \boldsymbol{\Lambda} \boldsymbol{J}_{\boldsymbol{\varphi}} \boldsymbol{\Lambda}^{\mathrm{T}}, \tag{2.25}$$

in which, $\boldsymbol{\Lambda}$ is the transformation matrix and can be found as below

$$\boldsymbol{\Lambda} \triangleq \frac{\partial \boldsymbol{\varphi}^{\mathrm{T}}}{\partial \boldsymbol{\psi}} = \begin{bmatrix} \frac{\partial \varphi_1}{\partial \psi_1} & \frac{\partial \varphi_2}{\partial \psi_1} & \cdots & \frac{\partial \varphi_{\mathrm{N_P}}}{\partial \psi_1} \\ \frac{\partial \varphi_1}{\partial \psi_2} & \ddots & \cdots & \frac{\partial \varphi_{\mathrm{N_P}}}{\partial \psi_2} \\ \vdots & \vdots & \ddots & \vdots \\ \frac{\partial \varphi_1}{\partial \psi_{\mathrm{N_S}}} & \cdots & \cdots & \frac{\partial \varphi_{\mathrm{N_P}}}{\partial \psi_{\mathrm{N_S}}} \end{bmatrix} \in \mathbb{R}^{N_{\mathrm{S}} \times N_{\mathrm{P}}}. \tag{2.26}$$

2.4 Reconfigurable Intelligent Surfaces (RISs)

The use of mobile communication systems is enormously grown in such a way that deploying more mmWave BSs is becoming challenging and energy consuming. One of the new promising technology is *reconfigurable intelligent surfaces (RISs)* that can boost the propagation environment by electronically controlled electromagnetic (EM) elements [69, 70].

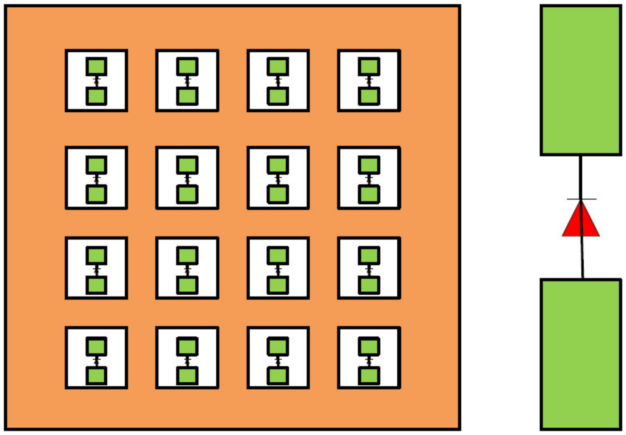

Figure 2.8: RIS architecture.

RISs are manufactured surfaces consisting of immense number of EM elements. These surfaces can be built in different shapes, depending on the application and location of the RIS. Fig.2.8 is showing the RIS architecture in which each element has one embeded diode and by altering its biasing voltage , the phase of the reflected signal is changed. Besides, one resistor is used in each element, so it can tune the amplitude of the reflected signal; however, in this thesis, the speed of propagated wave is assumed to be the same for all the frequencies. In addition, each element can independently change the amplitude and phase of the incident signal (i.e. $y_{\mathrm{n}} = \beta_{\mathrm{n}} e^{j\phi_{\mathrm{n}}}$); where y_{n} is the reflected signal from the nth element of RIS, x_{n} is the corresponding incident signal, $\beta_{\mathrm{n}} \in [0,1]$ and $\phi_{\mathrm{n}} \in [0,2\pi)$ indicate the amplitude attenuation and phase change factor, respectively. Wised altering of the reflecting parameters, can improve the received signal by the UE. Despite the current propagation environment, in which, different paths reflected from the obstacles, having destructive effects and worsening the communication efficiency, RISs can control the reflected or scattered radio waves and coherently combine them [71]. As a result, it's been shown in [70] that the received power in an environment without RIS is decreased with the fourth power of the user distance (i.e. $P_{\mathrm{r}} \propto \frac{1}{d^4}$); however, with RIS, the received power is boosted and is proportional to the second power of the user distance's reciprocal (i.e. $P_{\mathrm{r}} \propto \frac{1}{d^2}$). In general, some of the identifiable features of RISs include [70]:

- The RIS elements are passive and do not need any source of power. They can be fed by reflected or scattered radio signals.
- They are able to be programmed via a software.
- As they do not use any analog to digital (ADC) and digital to analog (DAC) converters, receiver noise does not affect them.
- They can respond to full-band frequency waves.
- They can be easily established.

These characteristics of RISs, make it practical and satisfying for the following indoor and outdoor applications [69]:

- If the line-of-sight (LOS) path is blocked between BS and UE, RIS is applicable for intelligent reflection of the signal.
- RISs can cancel the BS's signal to an inlegitimate user by non- RIS reflected signal; So, it can enhance the physical layer security.
- RISs are able to boost the signal strength for the UE located at the cell edge.
- In internet-of-things (IoT), RISs are useful to enhance the low power device to device signals.

In chapter 5, we will examine the effect of HWIs on the performance of RISs.

2.5 Summary

In this chapter, background on array signal processing and derivation of array manifold vector has been covered. As in this thesis, MIMO mmWave communication systems is used, the concept of analog beamforming in MIMO systems is introduced and consequently, the received signal has been modeled. HWIs has been introduced and mathematically presented. Afterwards, a tool for assessing the performance of an estimator, CRLB and FIM have been provided; these tools are going to be used in the rest of this thesis. At the end, a new-brand technology, RIS and its characteristics have been introduced. In brief, this chapter has provided a background information of all the concepts used in this thesis.

Chapter 3

Hardware Impairments Effects on 2D Mobile Localization under LOS Condition

Overview: Location-awareness is expected to be one of the main services in 5G millimeter-wave (mmWave) communication systems. In mm-Wave, multiple-input multiple-output (MIMO) systems will be used, leading to the deployment of antenna arrays in both transmitter and receiver. Hardware components being used in transceiver are commonly modeled as linear filters; but practically, this linearity is not fully satisfied. Power amplifiers and filters applied in antennas mostly show nonlinear behavior, causing loss in spectral efficiency (SE) and signal quality. This non-linearity is referred to hardware impairments (HWIs). Under HWIs model at both the transmitter and receiver, 2D localization performance is examined. Towards that, we derive position and orientation error bounds and study the effect of HWIs on the derived bounds. The numerical results reveal that HWIs have a significant effect on localization and it causes more than 100% degradation in both the transmitter and receiver. Also, the rate of degradation stays the same for both position and orientation error bounds except for the oriented UE.

3.1 Introduction

Evolution in modern communication technology has been accelerated as mmWave communication systems emerged. MmWave communication systems can provide higher data rates along with lower delays and constant connectivity for the next generation communication systems [72]. Moreover, mmWave attracted enormous researchers to investigate its capabilities, as offering more available spectrum from 30 GHz to 300 GHz [73].

In parallel, localization, the most game-changing development in wireless systems, is counted as one of the main services of 5G mmWave communication systems; this serves in variety of applications like vehicular communications and street macro applications [74]. For example, [75] estimated the position of a moving vehicle by mapping the 5G mmWave radio environment. It was shown that the error in positioning has the order of centimeters [76].

By employing large number of antennas in mmWave communication systems' transceiver and consequently estimation of the angle of arrival (AoA), angle of departure (AoD) [77] and time of arrival (ToA) [78] for positioning, location-aware communication will be possible. Single-anchor localization is frequently used in literature and it is a common strategy for 5G. For example, in [15], Cramér-Rao bound (CRB) for position and orientation from a single transmitter, have been derived and the possibility of estimating user's position has been demonstrated. Also, [16] and [17], with the same methodology of finding CRB but different approaches (the first for comparing multiple-input multiple-output (MIMO) and beamforming and the latter for the uplink and downlink performance), obtained the position error bound (PEB) and orientation error bound (OEB) for 3D localization in 5G mmWave systems.

The power amplifiers used in the wireless communication transceiver are widely assumed as a linear filter. This ideal condition is hardly satisfied and in practice, manufacturing ideal hardware is more challenging [65]; this leads to the performance degradation, including positioning. The effect of hardware impairments (HWIs) on different aspects of performance were studied before; for example, [79] investigated the effect of HWIs on spectral efficiency in a hybrid precoding system and [80] proposed an algorithm for compensating deteriorated bit error rate (BER) caused by HWIs. It is noted in [81] that these impairments cause non-negligible degradation. Plus, [82] reformulated the estimation of the channel parameters affected by HWIs from a Bayesian perspective to recover the sparsity of angular domain channel in multi-path communication.

To the best of our knowledge, the effect of HWIs, on mmWave systems, such as an asynchronous transceiver and I/Q imbalance have been studied before in [60] and [83], respectively, but its effect on localization using combination of AoA, AoD and ToA, has not been investigated yet. This implies that exploring localization under HWIs is pivotal in 5G context. In this chapter, we consider a 2D scenario with uplink transmission and study the effect of HWIs on user equipment (UE) positioning.

The rest of the chapter is organized as follows: The received signal is obtained and the localization problem is determined in Section 3.2. After calculating the received noise variance, Fisher information matrix (FIM) of channel parameters is derived in Section 3.3. Subsequently, Section 3.4 presents the transformed channel to the location parameters' equivalent FIM (EFIM). The resulting PEB and OEB degradation is discussed in Section 3.5. Finally, Section 3.6 concludes the chapter.

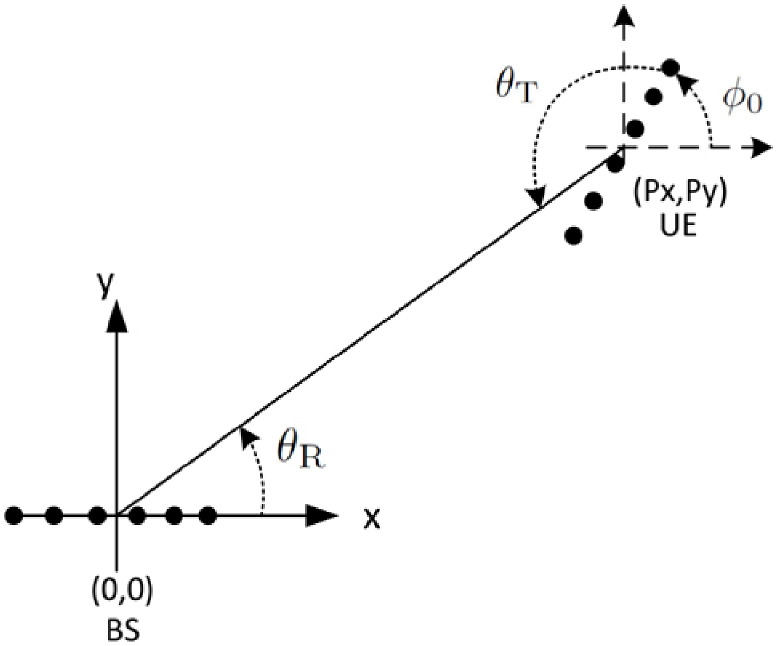

Figure 3.1: Considered scenario including UE as a transmitter and BS as a receiver equipped with linear array with N_{T} and N_{R} antennas respectively.

3.2 Problem Formulation

We consider an uplink transmission scenario consisting of a base station (BS) with N_{R} antennas and a UE with N_{T} antennas. Both are arranged as a uniform linear array (ULA) lying on the x-axis. The BS is placed at origin and UE's position $\boldsymbol{p} = [p_x, p_y]^{\mathrm{T}}$ is unknown with unknown orientation ϕ_0 measured from the positive x-axis. Also, we assume one line of sight (LOS) path [1] between the BS and the UE.

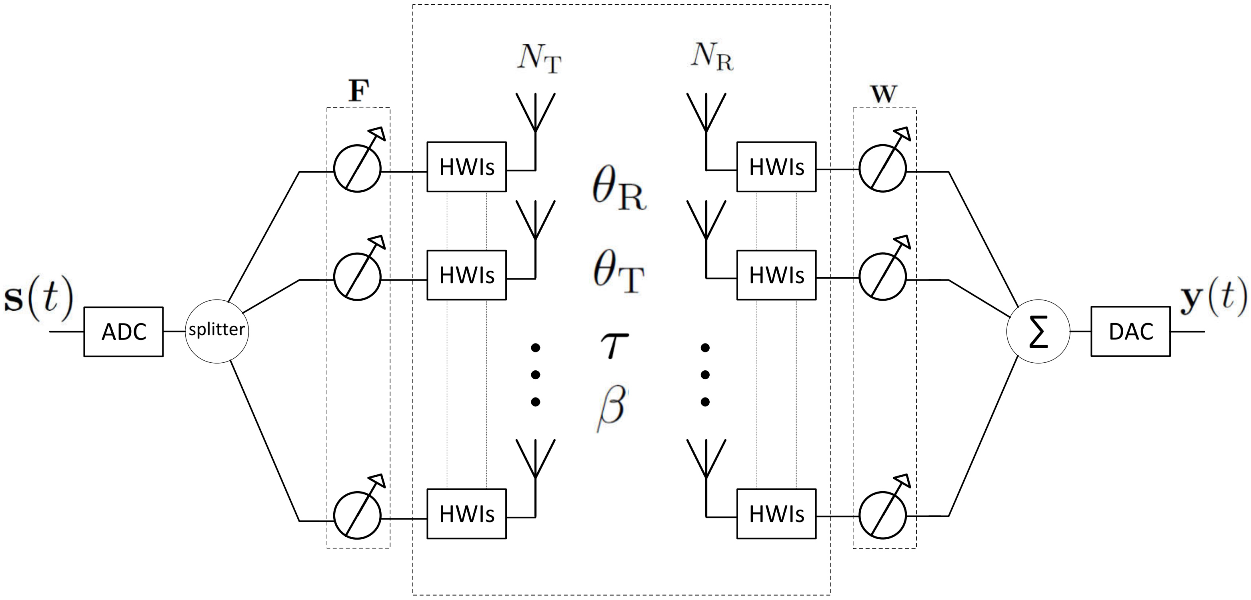

Figure 3.2: 5G mmWave transceiver structure under hardware impairments.

3.2.1 System and Signal Models

The transceiver structure under HWIs is shown in Fig. 3.2. Based on [65], the transmitted signal $\boldsymbol{x}(t) \triangleq [x_1(t), \cdots, x_{N_{\mathrm{T}}}(t)]^{\mathrm{T}}$ at the output of the impaired transmitter hardware component, can be written as

$$\boldsymbol{x}(t) = \sqrt{\kappa_s}\boldsymbol{F}\boldsymbol{s}(t) + \boldsymbol{\eta}_s, \tag{3.1}$$

where $\boldsymbol{s}(t) \triangleq [s_1(t), \cdots, s_{N_{\mathrm{B}}}(t)]^{\mathrm{T}}$ is the transmitted complex baseband signal with power $\mathbb{E}\{|\boldsymbol{s}|^2\} = E\boldsymbol{I}_{N_{\mathrm{B}}}$ and N_{B} is the number of transmitted beams. Also, $\boldsymbol{\eta}_s \sim \mathcal{CN}(0, (1 - \kappa_s)E\boldsymbol{I}_{\mathrm{N_T}})$ and κ_s represent the complex additive distortion noise and the HWIs factor at the transmitter, respectively [65]; in which $\boldsymbol{I}_{\mathrm{N_T}}$ serves as identity matrix with $N_{\mathrm{T}} \times N_{\mathrm{T}}$ elements.

---

[1] This is a strong assumption, as for studying the effect of HWIs on localization, LOS is quite more informative than non-LoS (NLoS) paths.

Analog directional beamforming (DBF) in transmitter with N_{B} beams are identified by $\boldsymbol{F} = [\boldsymbol{f}_1, \cdots, \boldsymbol{f}_{N_{\mathrm{B}}}] \in \mathbb{C}^{N_{\mathrm{T}} \times N_{\mathrm{B}}}$. Note that for making unit transmitted power, we set $Tr(\boldsymbol{F}^{\mathrm{H}}\boldsymbol{F}) = 1$ in which $Tr(.)$ stands for the matrix trace. It is noticeable that, in the ideal case, $\kappa_s = 1$ and $\boldsymbol{\eta}_s = 0$ resulting in $\boldsymbol{x}(t) = \boldsymbol{F}\boldsymbol{s}(t)$.

Similar to common used model (e.g., [73], [83], [17]) by denoting the AoD, AoA and propagation delay as θ_{T}, θ_{R} and τ, respectively, the recieved signal $\boldsymbol{y}(t) \in \mathbb{C}^{N_{\mathrm{B}}}$ can be expressed as

$$\begin{aligned} \boldsymbol{y}(t) = & \underbrace{\sqrt{\kappa_s\kappa_r}\beta \boldsymbol{W}^{\mathrm{H}}\boldsymbol{a}_{\mathbf{R}}(\theta_{\mathrm{R}})\boldsymbol{a}_{\mathbf{T}}{}^{\mathrm{H}}(\theta_{\mathrm{T}})\boldsymbol{F}\boldsymbol{s}(t-\tau)}_{\text{Desired signal}} + \underbrace{\sqrt{\kappa_r}\beta \boldsymbol{W}^{\mathrm{H}}\boldsymbol{a}_{\mathbf{R}}(\theta_{\mathrm{R}})\boldsymbol{a}_{\mathbf{T}}{}^{\mathrm{H}}(\theta_{\mathrm{T}})\boldsymbol{\eta}_s}_{\text{Transmitter distortion noise}} \\ & + \underbrace{\boldsymbol{W}^{\mathrm{H}}\boldsymbol{\eta}_r}_{\text{Receiver distortion noise}} + \underbrace{\boldsymbol{W}^{\mathrm{H}}\boldsymbol{n}(t)}_{\text{Noise}}, \end{aligned} \tag{3.2}$$

such that $\beta = \beta_{\mathrm{R}} + j\beta_{\mathrm{I}}$ is the complex path gain. Also, transmit array vector $\boldsymbol{a}_{\mathrm{T}}(\theta_{\mathrm{T}})$ is given below

$$\boldsymbol{a}_{\mathrm{T}}(\theta_{\mathrm{T}}) = \frac{1}{\sqrt{N_{\mathrm{T}}}} e^{-j\frac{2\pi d}{\lambda}\cos(\theta_{\mathrm{T}})\boldsymbol{x}_{\mathrm{T}}}, \tag{3.3}$$

where d is the inter-element spacing, and $\boldsymbol{x}_{\mathrm{T}} \triangleq \left[-\frac{N_{\mathrm{T}}-1}{2}, -\frac{N_{\mathrm{T}}-1}{2}+1, ..., \frac{N_{\mathrm{T}}-1}{2}\right]$ is the vector indicating the antenna location at the transmitter. $\boldsymbol{a}_{\mathrm{R}}(\theta_{\mathrm{R}})$ can be similarly defined as well. In addition, similar to the transmitter side, analog receive beamforming with N_{B} beams is noted by $\boldsymbol{W} = [\boldsymbol{w}_1, \cdots, \boldsymbol{w}_{N_{\mathrm{B}}}] \in \mathbb{C}^{N_{\mathrm{R}} \times N_{\mathrm{B}}}$. Moreover, the elements of $\boldsymbol{n}(t) \triangleq [n_1(t), n_2(t), ..., n_{N_{\mathrm{R}}}(t)]^{\mathrm{T}} \in \mathbb{C}^{N_{\mathrm{R}}}$ are identified as proper zero-mean additive white Gaussian noise with spectral density σ_{n}^2.

For simplicity of exposition and due to the sparse transmission in 5G mmWave channels [73], we assume orthogonal beams for the receiver, such that $\boldsymbol{W}^{\mathrm{H}}\boldsymbol{W} = \boldsymbol{I}_{N_{\mathrm{B}}}$ and unit power for array response vectors $\boldsymbol{a}_{\mathrm{R}}(\theta_{\mathrm{R}})$ and $\boldsymbol{a}_{\mathrm{T}}(\theta_{\mathrm{T}})$. Consequently, the covariance matrix of the reciever complex additive distortion noise can be written as

$$\boldsymbol{\Sigma}_{\boldsymbol{\eta}_{\mathbf{r}}} = (1-\kappa_{\mathrm{r}})|\beta|^2 E \boldsymbol{I}_{N_{\mathrm{R}}}.$$

3.2.2 2D localization problem

Finding the bounds of the position and orientation errors at the UE is our desire. Towards that, we find the received noise variance first and then we calculate Fisher information of observed parameters $\boldsymbol{\varphi}_{\mathrm{C}} \triangleq \{\theta_{\mathrm{R}}, \theta_{\mathrm{T}}, \tau, \beta_{\mathrm{R}}, \beta_{\mathrm{I}}, \kappa\}$. Next step will be transformation of the observed Fisher information parameters into the position and orientation domain.

3.3 FIM of Channel Parameters

The noise covariance matrix can be calculated as follows. Defining $\kappa = \sqrt{\kappa_{\mathrm{r}}\kappa_{\mathrm{s}}}$, the received signal $\boldsymbol{y}(t)$ in (3.2) can be divided into two parts; the mean function $\boldsymbol{\mu}(t)$ and the aggregated noise $\boldsymbol{z}(t)$. They can be expressed as below

$$\boldsymbol{\mu}(t) = \kappa\beta \boldsymbol{W}^{\mathrm{H}} \boldsymbol{a}_{\mathbf{R}}(\theta_{\mathrm{R}}) \boldsymbol{a}_{\mathbf{T}}{}^{\mathrm{H}}(\theta_{\mathrm{T}}) \boldsymbol{F}\boldsymbol{s}(t-\tau), \tag{3.4}$$

and

$$\boldsymbol{z}(t) = \sqrt{\kappa_{\mathrm{r}}}\beta \boldsymbol{W}^{\mathrm{H}} \boldsymbol{a}_{\mathbf{R}}(\theta_{\mathrm{R}}) \boldsymbol{a}_{\mathbf{T}}{}^{\mathrm{H}}(\theta_{\mathrm{T}}) \boldsymbol{\eta}_{\mathrm{s}} + \boldsymbol{W}^{\mathrm{H}} \boldsymbol{\eta}_{\mathrm{r}} + \boldsymbol{W}^{\mathrm{H}} \boldsymbol{n}(t), \tag{3.5}$$

With the same mentioned assumption for the orthogonality of the received beams, the covariance matrix of $\boldsymbol{z}(t)$ can be computed as below

$$\boldsymbol{\Sigma}_{\mathrm{z}} = \underbrace{\left(E(\beta_{\mathrm{R}}^2 + \beta_{\mathrm{I}}^2)(1-\kappa^2) + \sigma_{\mathrm{n}}^2\right)}_{\triangleq \sigma_{\mathrm{z}}^2} \boldsymbol{I}_{N_B}. \tag{3.6}$$

Note that κ can only take values between zero and one. From (3.6), it can be seen that as κ gets closer to zero, the noise covariance at the receiver worsens.

According to the introduced observed parameters $\boldsymbol{\varphi}_{\mathrm{C}}$, the corresponding FIM matrix can be built as

$$\boldsymbol{J}_{\mathrm{C}} = \begin{bmatrix} J_{\theta_{\mathrm{R}}\theta_{\mathrm{R}}} & J_{\theta_{\mathrm{R}}\theta_{\mathrm{T}}} & \cdots & J_{\theta_{\mathrm{R}}\kappa} \\ J_{\theta_{\mathrm{T}}\theta_{\mathrm{R}}} & \ddots & \cdots & J_{\theta_{\mathrm{T}}\kappa} \\ \vdots & \vdots & \ddots & \vdots \\ J_{\kappa\theta_{\mathrm{R}}} & \cdots & \cdots & J_{\kappa\kappa} \end{bmatrix} \in \mathbb{R}^{6\times 6}. \tag{3.7}$$

There are two groups of elements in (3.7) in which their values depend on whether the noise covariance in (3.6) is a function of their corresponding parameters or not. From (3.6), it is obvious that $\Sigma_{\boldsymbol{z}}$ is a function of parameters $\{\beta_{\mathrm{R}}, \beta_{\mathrm{I}}, \kappa\}$. Therefore, for $x, y \in \{\beta_{\mathrm{R}}, \beta_{\mathrm{I}}, \kappa\}$ [84],

$$\begin{aligned} J_{\mathrm{x,y}} =& \frac{\mathrm{T}_0 N_B^2}{(\sigma_{\mathrm{z}}^2)^2} \left(\frac{\partial}{\partial \mathrm{x}}\sigma_{\mathrm{z}}^2\right)\left(\frac{\partial}{\partial \mathrm{y}}\sigma_{\mathrm{z}}^2\right) \\ &+ \frac{1}{\sigma_{\mathrm{z}}^2}\int_0^{T_0} \left[\left(\frac{\partial}{\partial \mathrm{x}}\boldsymbol{\mu(t)}\right)^{\mathrm{H}}\left(\frac{\partial}{\partial \mathrm{y}}\boldsymbol{\mu(t)}\right) + \left(\frac{\partial}{\partial \mathrm{y}}\boldsymbol{\mu(t)}\right)^{\mathrm{H}}\left(\frac{\partial}{\partial \mathrm{x}}\boldsymbol{\mu(t)}\right)\right]\mathrm{d}t, \end{aligned} \tag{3.8}$$

While for the remaining parameters $x', y' \in \{\theta_{\mathrm{R}}, \theta_{\mathrm{T}}, \tau\}$ [84],

$$J_{\mathrm{x',y'}} = \frac{1}{\sigma_{\mathrm{z}}^2}\int_0^{T_0} \left[\left(\frac{\partial}{\partial \mathrm{x'}}\boldsymbol{\mu(t)}\right)^{\mathrm{H}}\left(\frac{\partial}{\partial \mathrm{y'}}\boldsymbol{\mu(t)}\right) + \left(\frac{\partial}{\partial \mathrm{y'}}\boldsymbol{\mu(t)}\right)^{\mathrm{H}}\left(\frac{\partial}{\partial \mathrm{x'}}\boldsymbol{\mu(t)}\right)\right]\mathrm{d}t, \tag{3.9}$$

where $T_0 \approx N_\mathrm{s} T_\mathrm{s}$ is the observation time in which N_s and T_s are the number of pilot symbols and the symbol period, respectively. The elements of (3.7) is given in Appendix.

The FIM matrix in (3.7), contains the interaction between all the parameters; but we need to focus on those parameters which give us information regarding positioning. Using the concept of equivalent FIM [17] and by dividing the parameters in $\boldsymbol{\varphi}_\mathrm{C}$ into two groups, we can exclude the information corresponding to the non-interested parameters. In this chapter, we call the parameters of our interest as geometrical parameters.
Similar to [83], by defining geometrical parameters as $\boldsymbol{\varphi}_\mathrm{G} \triangleq \{\theta_\mathrm{R}, \theta_\mathrm{T}, \tau\}$ and nuisance parameters as $\boldsymbol{\varphi}_\mathrm{N} \triangleq \{\beta_\mathrm{R}, \beta_\mathrm{I}, \kappa\}$, we can write (3.7) in block form as

$$\boldsymbol{J}_\mathrm{C} = \begin{bmatrix} \boldsymbol{J}_\mathrm{G} & \boldsymbol{J}_\mathrm{GN} \\ \boldsymbol{J}_\mathrm{GN}^\mathrm{T} & \boldsymbol{J}_\mathrm{N} \end{bmatrix} \in \mathbb{R}^{6\times 6}, \tag{3.10}$$

in which $\boldsymbol{J}_\mathrm{G}, \boldsymbol{J}_\mathrm{N} \in \mathbb{R}^{3\times 3}$ are geometrical and nuisance parameters' FIM, respectively; while $\boldsymbol{J}_\mathrm{GN} \in \mathbb{R}^{3\times 3}$ is the mutual information of $\boldsymbol{\varphi}_\mathrm{G}$ and $\boldsymbol{\varphi}_\mathrm{N}$. Hence, using Schur complement [85], the EFIM of $\boldsymbol{\varphi}_\mathrm{G}$ can be derived as below

$$\boldsymbol{J}_\mathrm{G}^\mathrm{e} = \boldsymbol{J}_\mathrm{G} - \boldsymbol{J}_\mathrm{GN} \boldsymbol{J}_\mathrm{N}^{-1} \boldsymbol{J}_\mathrm{GN}^\mathrm{T}. \tag{3.11}$$

3.4 FIM of Location Parameters

In this section, we are going to perform the last step for deriving final PEB and OEB. Towards that and using the transformation matrix Λ, we need to transform the EFIM of our desired channel parameters AoA, AoD and ToA in (3.11) into the EFIM of location parameters $\boldsymbol{\varphi}_{\mathrm{L}}$. Namely, define

$$\boldsymbol{\varphi}_{\mathrm{L}} \triangleq [p_x, p_y, \phi_0]^{\mathrm{T}}, \tag{3.12}$$

Then, the corresponding EFIM can be obtained as [67]

$$\boldsymbol{J}_{\mathrm{L}}^{\mathrm{e}} \triangleq \boldsymbol{\Lambda} \boldsymbol{J}_{\mathrm{G}}^{\mathrm{e}} \boldsymbol{\Lambda}^{\mathrm{T}}, \tag{3.13}$$

where,

$$\boldsymbol{\Lambda} = \frac{\partial \boldsymbol{\varphi}_{\mathrm{G}}^{\mathrm{T}}}{\partial \boldsymbol{\varphi}_{\mathrm{L}}} = \begin{bmatrix} \frac{\partial \theta_{\mathrm{R}}}{\partial p_{\mathrm{x}}} & \frac{\partial \theta_{\mathrm{T}}}{\partial p_{\mathrm{x}}} & \frac{\partial \tau}{\partial p_{\mathrm{x}}} \\ \frac{\partial \theta_{\mathrm{R}}}{\partial p_{\mathrm{y}}} & \frac{\partial \phi_{\mathrm{T}}}{\partial p_{\mathrm{y}}} & \frac{\partial \tau}{\partial p_{\mathrm{y}}} \\ \frac{\partial \theta_{\mathrm{R}}}{\partial \phi_0} & \frac{\partial \theta_{\mathrm{T}}}{\partial \phi_0} & \frac{\partial \tau}{\partial \phi_0} \end{bmatrix} \in \mathbb{R}^{3\times 3}. \tag{3.14}$$

The elements of transformation matrix $\boldsymbol{\Lambda}$ can be found through the relationship between channel and location parameters [83]. Based on Fig. 3.1,

$$\theta_{\mathrm{R}} = \tan^{-1}\left(\frac{p_y}{p_x}\right), \tag{3.15a}$$

$$\theta_{\mathrm{T}} = \tan^{-1}\left(\frac{p_y}{p_x}\right) + \pi - \phi_0, \tag{3.15b}$$

$$\tau = \frac{\|\boldsymbol{p}\|}{c}, \tag{3.15c}$$

where c is the propagation speed. In consequence, the PEB and OEB can be obtained as

$$\mathrm{PEB} = \sqrt{[\mathbf{C}]_{1,1} + [\mathbf{C}]_{2,2}}, \tag{3.16a}$$

$$\mathrm{OEB} = \sqrt{[\mathbf{C}]_{3,3}}, \tag{3.16b}$$

where $[\mathbf{C}]_{i,j}$ is the $(i,j)^{th}$ element of $\boldsymbol{C} = (\boldsymbol{J}_{\mathrm{L}}^{\mathrm{e}})^{-1}$.

3.5 Numerical results

3.5.1 Simulation setup

In this work, we consider a mmWave scenario including a BS with $N_{\mathrm{R}} = 64$ antennas located at the origin, and a UE, operating at $f = 38$ GHz, with $N_{\mathrm{T}} = 32$ antennas located in a square area (10 m×10 m), defined by $(p_x, p_y) \in \{(x,y) : y \geq |x| \cap y \leq 10\sqrt{2} - |x|\}$. In this investigation, UE is tilted by an orientation angle of 0 or 10 in azimuth. We use directional beamforming for both transmitter and receiver with $N_{\mathrm{B}} = 18$ beams, steering the transmission beams towards the azimuth angles $\phi_{\mathrm{T},l}, 1 \leq l \leq N_{\mathrm{B}}$ as

$$\boldsymbol{f}_l \triangleq \frac{1}{\sqrt{N_{\mathrm{B}}}} \boldsymbol{a}_{\mathrm{T}}(\phi_{\mathrm{T},l}),$$

where $\boldsymbol{a}_{\mathrm{T}}(\phi_{\mathrm{T},l})$ is the array response vector towards angle $\phi_{\mathrm{T},l}$. Receive beamforming $\boldsymbol{w}_l$ can be found in the same way. The propagated beams span the square area where UE is being moved (Fig.3.3). Moreover, the transmitted signal is assumed to be passed through a unit energy ideal *sinc* pulse shaping filter with bandwidth $W = 125$ MHz and $N_{\mathrm{s}} = 16$, and the noise variance $\sigma_{\mathrm{n}}^2 = -79$ dBm. The noise variance value has been experimentally chosen in order to gain an appropriate SNR. Furthermore, the practical range for HWIs factor κ is chosen based on error vector magnitude (EVM) metric on the transceivers. It is shown in [65] that for 4- phased shift keying (PSK) transceiver, EVM must be less than 0.0175. Consequently, $\kappa = 1 - \mathrm{EVM}^2 \geq 0.97$.

The simulations are performed in Matlab and averaged on 120 UE locations in order

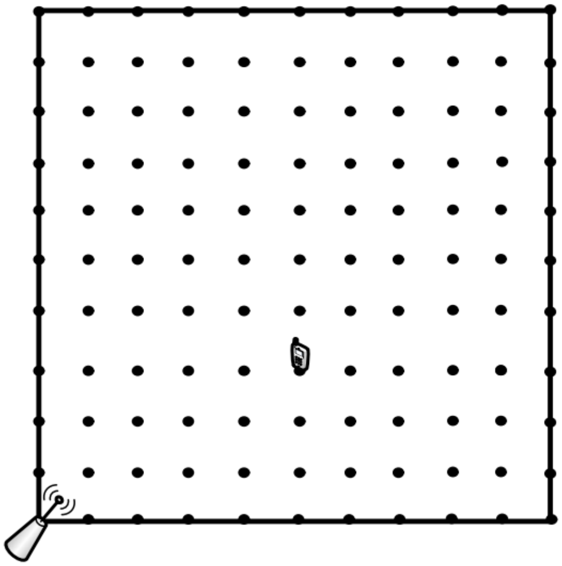

Figure 3.3: The spanned propagated beams on the UE locations.

to calculate the PEB and OEB degradation due to HWIs as in the following equations

$$\mathrm{PEB}_{\mathrm{deg}} = \left(\frac{\mathrm{PEB}_{\mathrm{HWIs}}}{\mathrm{PEB}_{\mathrm{ideal}}} - 1 \right) \times 100\%, \tag{3.17}$$

$$\mathrm{OEB}_{\mathrm{deg}} = \left(\frac{\mathrm{OEB}_{\mathrm{HWIs}}}{\mathrm{OEB}_{\mathrm{ideal}}} - 1 \right) \times 100\%, \tag{3.18}$$

where $\mathrm{PEB}_{\mathrm{ideal}}$ and $\mathrm{OEB}_{\mathrm{ideal}}$ are obtained using (3.16) after dropping off HWIs factor κ from $\boldsymbol{\varphi}_{\mathrm{N}}$ and setting it to one.

3.5.2 Performance Analysis

Fig. 3.4 and Fig. 3.5 present the PEB and its percentage degradation (calculated in (3.16a) and (3.17), respectively) with respect to HWIs factor κ for the considered scenario. For this simulation, the HWIs factor κ is changed uniformly between 0.9 to 1, for two different values of orientation angle ϕ_0. It can be seen that the minimum error bound and its degradation

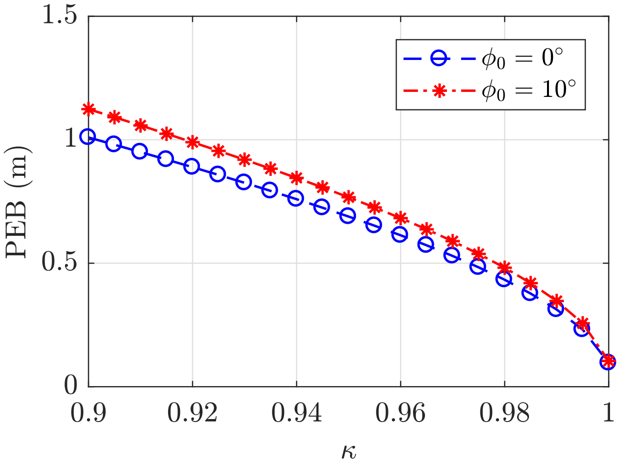

Figure 3.4: PEB with respect to κ at different orientation angles.

occurs at $\kappa = 1$, where there is ideal hardware. Plus, the both PEB and its degradation increase rapidly as the HWIs factor deteriorates by diverging from the ideal point. Also, as it is expected, the PEB worsens by increasing the UE orientation angle. This is the result of the reduced area covered by the transmitted beams and consequently missing the BS. Moreover, more impairment causes more degradation for $\phi_0 = 10°$ compared with $\phi_0 = 0°$. For instance, $0.2 \times 100\%$ degradation difference between the two curves can be noticed when $\kappa = 0.95$ compared with $0.3 \times 100\%$ when $\kappa = 0.9$; the same concept applies for the PEB. Also, from the simulation, it worth mentioning that in the case of ideal hardware, the PEB for $\phi_0 = 0°$ and $\phi_0 = 10°$ is 9.6 cm and 10.4 cm, while when $\kappa = 0.9$ these amounts are 100 cm and 112 cm, respectively. Fig. 3.6 and Fig. 3.7 show the OEB and its percentage degradation (calculated in (3.16b) and (3.18), respectively) with respect to the impairment factor κ. Except for the tilted UE, both PEB and OEB indicate the same behavior to non-ideal hardware, with $9.5 \times 100\%$ degradation at $\kappa = 0.9$. The two curves in these figures widen more in comparison with the ones in Fig. 3.4 and Fig. 3.5; meaning that, by tilting UE, the orientation estimation becomes more sensitive to

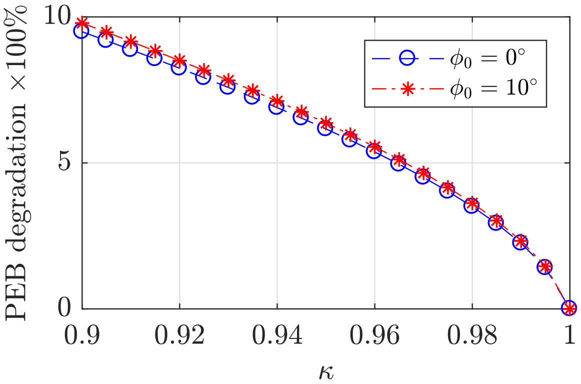

Figure 3.5: PEB degradation with respect to κ at different orientation angles.

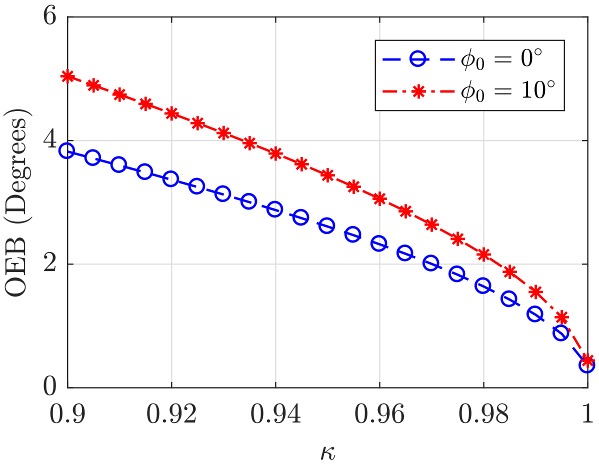

Figure 3.6: OEB with respect to κ at different orientation angles.

the HWIs than the position estimation. For instance, $0.61 \times 100\%$ degradation difference in the orientation estimation can be noticed when $\kappa = 0.9$ compared with $0.3 \times 100\%$ difference in position estimation. Also, from the simulation, in case of ideal hardware, for two different orientations 0° and 10°, the value of OEB is 0.35° and 0.44°, while in the case of $\kappa = 0.9$, these values change to 3.82° and 5.04°, respectively. SNR with respect to impairment factor κ is plotted in Fig. 3.8. As it is expected, maximum SNR occurs at the

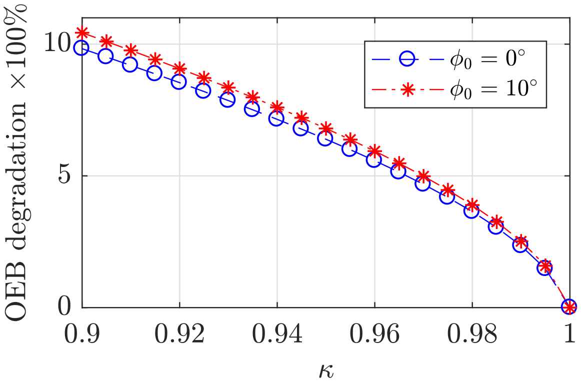

Figure 3.7: OEB degradation with respect to κ at different orientation angles.

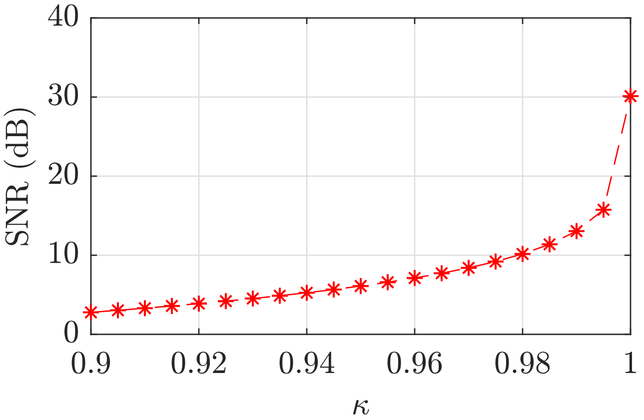

Figure 3.8: SNR with respect to κ when $\phi_0 = 0$ and $N_{\mathrm{B}} = 18$.

ideal point $\kappa = 1$ with amount 30.12 dB. As shown in this figure, there is 27.34 dB drop in SNR when $\kappa = 0.9$. In addition, PEB, OEB and SNR degradation in Fig. 3.5, Fig. 3.7 and Fig. 3.8 show the same behavior indicating that the value of κ corresponding to the maximum SNR matches with the one for the minimum value of PEB and OEB.

3.6 Conclusion

In this chapter the effect of HWIs on the localization error bounds for 2D 5G mmWave has been presented. Considering uplink transmission, our results show that with no orientation, PEB and OEB worsen by HWIs with the same amount of $9.5 \times 100\%$. However tilting UE, causes more effect on OEB than PEB. Moreover, the minimum degradation occurs at the ideal point for all of the cases. For the future work, we will consider uniform rectangular array (URA) antenna for both UE and BS in the 3D scenario and two way transmission.

3.7 Publications Resulted from This Chapter

- F. Ghaseminajm, E. Saleh, M. Alsmadi and S. S. Ikki, "Localization Error Bounds For 5G mmWave Systems Under Hardware Impairments," 2021 IEEE 32nd Annual International Symposium on Personal, Indoor and Mobile Radio Communications (PIMRC), 2021, pp. 1228-1233, doi: 10.1109/PIMRC50174.2021.9569299.

Chapter 4

Hardware Impairments Effects on 3D Mobile Localization Considering Perfect and Imperfect Clock Synchronization

Overview: Localization demands high-accuracy positioning, and this rings especially true in the context of 5G millimeter-wave (mmWave) systems. However, it is easier said than done. mmWave systems require a large number of antennas to be deployed at the transceiver, so having ideal hardware components at each antenna is unrealistic. Degradation in the received signal, caused by hardware impairments (HWIs), affects the spectral efficiency (SE), which in turn influences user positioning. Moreover, a high level of clock synchronization between the base station (BS) and the user equipment (UE) is rarely achieved. In this chapter, we investigate the effect of HWIs on UE localization under synchronous and asynchronous conditions. In order to minimize imperfect synchronization, two anchors or two-way localization protocols, a round-trip (RLP) as well as a collaborative localization protocol (CLP) are used. Conducting the localization process using the BS, we find the position and orientation bounds. We then study the effect of HWIs on the error bounds under the mentioned scenarios. Our numerical results show that HWIs have a significant impact on localization in all conditions, localization using two anchors and the CLP being more robust, however, against HWIs. Based on our outcome, compensating for imperfect synchronization using RLP does not increase the resilience of the system against HWIs.

4.1 Introduction

Millimeter-wave (mmWave) communication systems have triggered a fast-tracked evolution in modern communication systems. The spectrum available for mmWave (30 GHz-300 GHz), which is unrivaled compared to the other wireless networks, satisfies the high demand for media consumption by offering high data rates and lower latency [72]. This spectrum could then cater to the demand for high-area spectral efficiency (SE) and throughput for each user equipment (UE) [86]. Furthermore, mmWave communications have garnered considerable attraction from researchers because of their ability to operate at high frequencies. [73].

Localization is one of the main services of mmWave communication systems. Fifth generation (5G) networks will be the first to profit from location information. However, crucial challenges to signal processing must be overcome to allow for its accurate prediction [87]. This location data can be determined, for instance, through beamforming [35], pilot assignment [36] and resource allocation [37].

Because mmWave multiple-input multiple-output (MIMO) communication systems deploy a large number of antennas at the transceiver, estimations for the angles of departure (AoD) and arrival (AoA) are achievable using a single base station (BS) [77]. Furthermore, mmWave systems boast of large bandwidths, so we can very accurately estimate the time of arrival (ToA) [88–91]. Therefore, single-anchor localization of the UE is applicable by merging angular and temporal data. For example, position estimation and Cramér-Rao bounds (CRB) for both position (PEB) and orientation error bounds (OEB), using single-anchor and a combination of AoD, AoA and ToA, were found by [15]. Even more, [17] and [16] used the same method to find the PEB and OEB.

Ideally, modulated passband signals are reliably generated from the baseband samples at the transmitter side and are then demodulated at the receiver side [65]. The reality, however, is that manufacturing the transceiver's hardware inevitably results in some minor deficiencies that cause major degradation to the system's performance. These impairments can be denoted in terms of multiplicative and additive distortions, where the former shifts the signal's phase and the latter is added to the signal as a distortion noise [86]. Consequently, the assumption of linearity in the power amplifier deployed in the transceiver's antennas is hardly ever satisfied [65].

One localization requirement that is often overlooked in the literature is synchronization between the BS and the UE. In other words, most papers assume that the BS and UE are perfectly synchronized; for example, [15], [17] and [92], presume that the clock offset between the transmitter and receiver is zero. However, in this chapter, we do not neglect this important consequence of hardware impairments (HWIs). Considering localization using a combination of ToA, AoD and AoA, the effects of hardware disorders such as I/Q imbalance and asynchronous transceivers were studied in [61] and [83], respectively. The effects of HWIs on various components of the system were also studied in the literature; for instance, [82] and [93] estimated the channel under HWIs. The first article used Bayesian compressive sensing and least square estimation methods, and the latter reformulated the estimation algorithm to compensate for the sparsity of the channel spatial domain.

Even more, [80] compensated for the degraded signal-to-noise ratio (SNR) caused by HWIs, and they did this by optimizing the beamforming in intelligent reflecting surfaces (IRS). [86] studied the effect of transceiver HWIs on the SE and energy efficiency (EE), also in the presence of IRS. Furthermore, the impact of HWIs on the hybrid beamforming performance was studied in [94] and [79]. Moreover, [95] examined the effects of HWIs on the coverage probability of a multi-tier multi-user geometry. In addition, [81] ascertained that HWIs cause a non-negligible deterioration in the system performance.

To the best of our knowledge, the effect of HWIs on positioning under asynchronous conditions has not yet been evaluated. In this chapter, we present a scenario in which both HWIs and the lack of synchronization are taken into consideration. Surveying localization at the BS, and considering line of sight (LOS) communication, the main contributions of this work can be enumerated as follows

- Evaluating the effect of HWIs on one-way localization (OWL) in a three-dimensional scenario under perfect synchronization.
- Evaluating the effect of HWIs on OWL using two anchors in a three-dimensional scenario under imperfect synchronization. In this method, the second anchor is used to eliminate the clock offset between the transceivers. This evaluation is studied for two different cases.
- Evaluating the effect of HWIs on two-way localization (TWL) using a round-trip localization protocol (RLP) under imperfect synchronization. In the RLP, localization

is done using forward and backward temporal estimation as well as backward angular estimation.

- Evaluating the effect of HWIs on TWL using a collaborative localization protocol (CLP) under imperfect synchronization. In the CLP, localization is carried out using forward and backward temporal and angular estimation.

The rest of the chapter is structured as follows: The localization problem is outlined, and the forward and backward channel specifications along with the general formula for the received signals at the both transmissions is obtained, in Section 4.2. The channel parameters' Fisher information matrices (FIM) for the studied cases (i.e. OWL cases 1-3, RLP and CLP) are presented in Section 4.3. Section 4.4 presents the transformation of the channel to the location parameters' equivalent FIM (EFIM). The resulting PEB, OEB and their degradation are analyzed in Section 4.5. Finally, Section 4.6 concludes the chapter.

4.2 System Model and Problem Formulation

Let us consider the LOS two-way transmission scenario depicted in Fig. 4.1. There are the two devices: D_1 acts as an initiator with $N_1 = N_{1,\mathrm{x}} \times N_{1,\mathrm{z}}$ antennas, and D_2 acts as a responder with $N_2 = N_{2,\mathrm{x}} \times N_{2,\mathrm{z}}$ antennas. The initiator is located at the origin and the responder at an unknown position $\boldsymbol{p} \triangleq [p_\mathrm{x}, p_\mathrm{y}, p_\mathrm{z}]^\mathrm{T}$ and orientation $\boldsymbol{o} \triangleq [\phi_0, \theta_0]^\mathrm{T}$. Our goal is to investigate the effect of HWIs on the error bounds for position $\boldsymbol{p}$ and orientation $\boldsymbol{o}$. We do so using 1) ToA, AoA and AoD under the OWL with a synchronous transceiver and 2) the two anchors or the RLP and CLP under TWL with imperfect synchronization between the communicating devices.

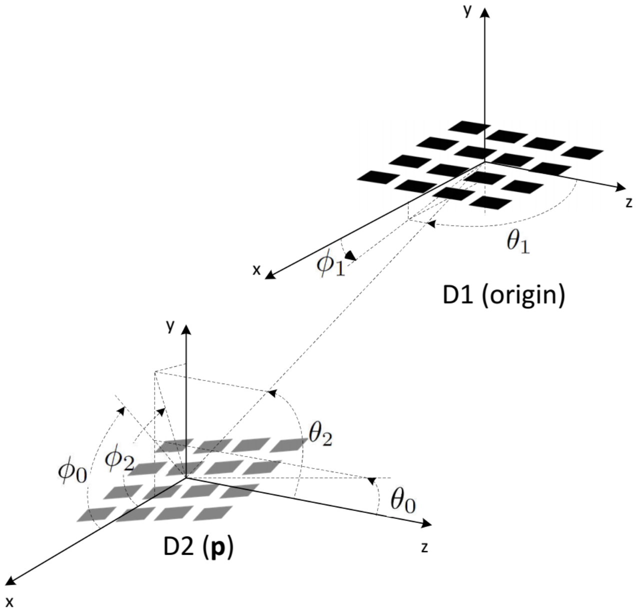

Figure 4.1: Considered scenario including the both devices D_1 and D_2 in the forward transmission.

To that effect, we assume that the employed power amplifiers in both D_1 and D_2 for the two transmissions are impaired by factors κ_1 and κ_2, as well as by the initiate complex additive distortion noises $\boldsymbol{\eta}_1^{\mathrm{f}}$ and $\boldsymbol{\eta}_2^{\mathrm{b}}$, respectively. The superscripts "f" and "b" stand for the forward and backward transmission, and the subscripts "1" and "2" denote devices D_1 and D_2, respectively. The received signals in the forward and backward channel are mathematically formulated.

4.2.1 System and signal model in forward transmission

In this subsection, the general formulas for the forward received signal in the two-way transmission are presented. Then, in order to determine the error bounds, the covariance matrix of the received noise is calculated. Note that this is not applicable in the one way transmission model; the signal model for this transmission is given in the next subsection.

As can be seen from Fig. 4.2, in all of the studied scenarios, localization is performed at device D_1. Figs. 4.2b and 4.2c illustrate the TWL protocols in which D_1 transmits the impaired signal $\boldsymbol{x_1}(t) = \kappa_1 \boldsymbol{F}^{\mathrm{f}} \boldsymbol{s_1}(t) + \boldsymbol{\eta}_1^{\mathrm{f}}$ at $t = 0$, which is then received by D_2 as $\boldsymbol{y_2}(t)$ at $t = \tau^{\mathrm{f}}$ [65]. Here, $\boldsymbol{s}_1(t) \triangleq [s_{1,1}(t), \cdots, s_{1,N_{\mathrm{B}}}(t)]^{\mathrm{T}}$ is the transmitted complex baseband signal with power $\mathbb{E}\{|\boldsymbol{s}_1|^2\} = E\boldsymbol{I}_{N_{\mathrm{B}}}$ ($\mathbb{E}$ is the expectation operator) and N_{B} is the number of transmitted beams. The covariance matrix of the forward additive distortion noise η_1^{f} is calculated as $\boldsymbol{\Sigma}_{\boldsymbol{\eta}_1^{\mathrm{f}}} = (1-\kappa_1^2)E\boldsymbol{I}_{N_1}$. $\boldsymbol{F}^{\mathrm{f}}$ is the forward transmit beamforming matrix, which is defined as $\boldsymbol{F}^{\mathrm{f}} \triangleq [\boldsymbol{f}_1^{\mathrm{f}}, \cdots, \boldsymbol{f}_{N_{\mathrm{B}}}^{\mathrm{f}}] \in \mathbb{C}^{N_1 \times N_{\mathrm{B}}}$. Here, $\boldsymbol{f}_{\mathrm{b}}^{\mathrm{f}}, 1 \leq b \leq N_{\mathrm{B}}$ is the b^{th} beam of D_1. Moreover, $\tau^{\mathrm{f}} = \tau + B$ is the local ToA in the forward channel at D_2, and B is an unknown clock offset between D_1 and D_2.

The impaired received signal $\boldsymbol{y_2}(t)$ can hence be written as [65]

$$\begin{aligned}\boldsymbol{y_2}(t) &= \beta\kappa_1\kappa_2 \boldsymbol{W}^{\mathrm{f}^{\mathrm{H}}} \boldsymbol{a}_2(\boldsymbol{v}_2^{\mathrm{f}}) \boldsymbol{a}_1^{\mathrm{H}}(\boldsymbol{v}_1^{\mathrm{f}}) \boldsymbol{F}^{\mathrm{f}} \boldsymbol{s_1}(t-\tau^{\mathrm{f}}) \\ &\quad + \beta\kappa_2 \boldsymbol{W}^{\mathrm{f}^{\mathrm{H}}} \boldsymbol{a}_2(\boldsymbol{v}_2^{\mathrm{f}}) \boldsymbol{a}_1^{\mathrm{H}}(\boldsymbol{v}_1^{\mathrm{f}}) \boldsymbol{\eta}_1^{\mathrm{f}} + \boldsymbol{W}^{\mathrm{f}^{\mathrm{H}}} \boldsymbol{\eta}_2^{\mathrm{f}} + \boldsymbol{W}^{\mathrm{f}^{\mathrm{H}}} \boldsymbol{n}_2(t), \end{aligned} \tag{4.1}$$

where $\boldsymbol{W}^{\mathrm{f}} \in \mathbb{C}^{N_2 \times N_{\mathrm{B}}}$ represents the receive analog beamforming matrix of a forward channel containing N_{B} beams. $\boldsymbol{n}_2(t)$ is the proper additive white Gaussian noise (AWGN) vector with a zero mean and covariance matrix $N_0\boldsymbol{I}_{\mathrm{N}_2}$. β is the channel gain with real and imaginary parts β_{R} and β_{I}, respectively. Furthermore, $\boldsymbol{a}_1(\boldsymbol{v}_1^{\mathrm{f}}) \in \mathbb{C}^{\mathrm{N}_1}$ is the array manifold vector of D_1. It is also a function of the vector $\boldsymbol{v}_1^{\mathrm{f}} \triangleq \{\phi_1, \theta_1\}$, consisting of the horizontal and elevation angles of AoD in the forward transmission. This can be calculated for the uniform rectangular array (URA) lying on the xz-plane, as

$$\boldsymbol{a}_1(\boldsymbol{v}_1^{\mathrm{f}}) = \frac{1}{\sqrt{N_1}} e^{-j\frac{2\pi}{\lambda}(d_{\mathrm{x}}\sin(\theta_1)\cos(\phi_1)\boldsymbol{x}_1 + d_{\mathrm{z}}\cos(\theta_1)\boldsymbol{z}_1)}, \tag{4.2}$$

where $d_{\mathrm{x}} = d_{\mathrm{z}} = \lambda/2$ is the inter-element spacing, and $\boldsymbol{x}_1$ and $\boldsymbol{z}_1$ are the antenna elements' locations on the x and z-axis, as defined below [14]

$$\boldsymbol{x}_1 = \mathbf{1}_{\mathrm{N}_{1,\mathrm{z}}} \otimes \tilde{\boldsymbol{x}}_1,$$
$$\boldsymbol{z}_1 = \tilde{\boldsymbol{z}}_1 \otimes \mathbf{1}_{\mathrm{N}_{1,\mathrm{x}}},$$

where $\otimes$ denotes the Kronecker products,

$$\tilde{\boldsymbol{x}}_1 \triangleq \left[-\frac{N_{1,\mathrm{x}}-1}{2}, -\frac{N_{1,\mathrm{x}}-1}{2}+1, \cdots, \frac{N_{1,\mathrm{x}}-1}{2}\right]^{\mathrm{T}}, \tag{4.3}$$

and

$$\tilde{\boldsymbol{z}}_1 \triangleq \left[-\frac{N_{1,\mathrm{z}}-1}{2}, -\frac{N_{1,\mathrm{z}}-1}{2}+1, \cdots, \frac{N_{1,\mathrm{z}}-1}{2}\right]^{\mathrm{T}}. \tag{4.4}$$

Similarly, the responder's array manifold vector $a_2(\boldsymbol{v}_2^{\mathrm{f}}) \in \mathbb{C}^{\mathrm{N}_2}$ is a function of the vector $\boldsymbol{v}_2^{\mathrm{f}} \triangleq \{\phi_2, \theta_2\}$, consisting of the horizontal and elevation angles of AoA in the forward transmission and can be calculated as $a_1(\boldsymbol{v}_1^{\mathrm{f}})$ in (4.2). Note that based on our definition in (4.2), $\boldsymbol{a_1}^{\mathrm{H}}\boldsymbol{a_1} = \boldsymbol{a_2}^{\mathrm{H}}\boldsymbol{a_2} = 1$.

Using $\boldsymbol{\Sigma}_{\boldsymbol{\eta}_1^{\mathrm{f}}}$, the covariance matrix of the forward noise distortion at device D_2 is given as

$$\boldsymbol{\Sigma}_{\boldsymbol{\eta}_2^{\mathrm{f}}} = (1-\kappa_2^2)|\beta|^2 E \boldsymbol{I}_{N_2}. \tag{4.5}$$

Therefore, the signal and noise components of the received signal in (4.1) can be separated as

$$\boldsymbol{\mu_2}(t) = \beta\kappa_1\kappa_2 {\boldsymbol{W}^{\mathrm{f}}}^{\mathrm{H}} \boldsymbol{a}_2(\boldsymbol{v}_2^{\mathrm{f}})\boldsymbol{a}_1^{\mathrm{H}}(\boldsymbol{v}_1^{\mathrm{f}})\boldsymbol{F}^{\mathrm{f}}\boldsymbol{s_1}(t-\tau^{\mathrm{f}}), \tag{4.6}$$

$$\boldsymbol{z_2}(t) = \beta\kappa_2 {\boldsymbol{W}^{\mathrm{f}}}^{\mathrm{H}} \boldsymbol{a}_2(\boldsymbol{v}_2^{\mathrm{f}})\boldsymbol{a}_1^{\mathrm{H}}(\boldsymbol{v}_1^{\mathrm{f}})\boldsymbol{\eta}_1^{\mathrm{f}} + {\boldsymbol{W}^{\mathrm{f}}}^{\mathrm{H}}\boldsymbol{\eta}_2^{\mathrm{f}} + {\boldsymbol{W}^{\mathrm{f}}}^{\mathrm{H}}\boldsymbol{n}_2(t). \tag{4.7}$$

Using the covariance matrix of η_1^{f} and η_2^{f}, the covariance of the forwarded noise can be given as

$$\boldsymbol{\Sigma}_{\boldsymbol{z}_2(t)} = \underbrace{\left(E(\beta_{\mathrm{R}}^2+\beta_{\mathrm{I}}^2)(1-\kappa_1^2\kappa_2^2)+N_0\right)}_{\triangleq\sigma_{\mathrm{z}}^2} {\boldsymbol{W}^{\mathrm{f}}}^{\mathrm{H}}\boldsymbol{W}^{\mathrm{f}}. \tag{4.8}$$

4.2.2 System and signal model in backward transmission

In the backward transmission (the only transmission in the OWL), device D_2 transmits the impaired signal $\boldsymbol{x_2}(t) = \kappa_2\boldsymbol{F}^{\mathrm{b}}\boldsymbol{s_2}(t) + \boldsymbol{\eta}_2^{\mathrm{b}}$ at $t = t^{\mathrm{b}}$ which is going to be received by D_1 as $\boldsymbol{y_1}(t)$ at $t = \tau^{\mathrm{b}}$. Note that $\boldsymbol{x_2}(t)$, $\boldsymbol{s_2}(t)$ and the covariance matrix of $\boldsymbol{\eta}_2^{\mathrm{b}}$ can be defined in the same way that was seen in the forward transmission. For the OWL, $t_{\mathrm{b}} = 0$, while for the TWL, based on two-way protocols, t^{b} can either depend on a predetermined delay after receiving the forward signal, or it can be entirely independent from the forward transmission.

Based on this, the obtained signal through the backward transmission can be written as

$$\begin{aligned}\boldsymbol{y_1}(t) =& \beta\kappa_1\kappa_2 {\boldsymbol{W}^{\mathrm{b}}}^{\mathrm{H}} \boldsymbol{a}_1(\boldsymbol{v}_1^{\mathrm{b}})\boldsymbol{a}_2^{\mathrm{H}}(\boldsymbol{v}_2^{\mathrm{b}})\boldsymbol{F}^{\mathrm{b}}\boldsymbol{s_2}(t-\tau^{\mathrm{b}}) + \beta\kappa_1 {\boldsymbol{W}^{\mathrm{b}}}^{\mathrm{H}} \boldsymbol{a}_1(\boldsymbol{v}_1^{\mathrm{b}})\boldsymbol{a}_2^{\mathrm{H}}(\boldsymbol{v}_2^{\mathrm{b}})\boldsymbol{\eta}_2^{\mathrm{b}} \\ &+ {\boldsymbol{W}^{\mathrm{b}}}^{\mathrm{H}}\boldsymbol{\eta}_1^{\mathrm{b}} + {\boldsymbol{W}^{\mathrm{b}}}^{\mathrm{H}}\boldsymbol{n}_1(t),\end{aligned} \tag{4.9}$$

where $\boldsymbol{F}^{\mathrm{b}} \in \mathbb{C}^{N_2 \times N_{\mathrm{B}}}$ and $\boldsymbol{W}^{\mathrm{b}} \in \mathbb{C}^{N_1 \times N_{\mathrm{B}}}$ are the transmit and receive beamforming matrices in the backward transmission, respectively. $\boldsymbol{n}_1(t)$ has the same specifications as AWGN noise $\boldsymbol{n}_2(t)$ in (4.1). In addition, $\boldsymbol{v}_1^{\mathrm{b}} \triangleq \{\phi_1, \theta_1\}$ and $\boldsymbol{v}_2^{\mathrm{b}} \triangleq \{\phi_2, \theta_2\}$ are the AoA and AoD in the backward transmission, respectively. As for the forward transmission, the signal and noise parts can be set apart as

$$\boldsymbol{\mu}_1(t) = \beta\kappa_1\kappa_2 {\boldsymbol{W}^{\mathrm{b}}}^{\mathrm{H}} \boldsymbol{a}_1(\boldsymbol{v}_1^{\mathrm{b}}) \boldsymbol{a}_2^{\mathrm{H}}(\boldsymbol{v}_2^{\mathrm{b}}) \boldsymbol{F}^{\mathrm{b}} \boldsymbol{s}_2(t - \tau^{\mathrm{b}}), \tag{4.10}$$

$$\boldsymbol{z}_1(t) = \beta\kappa_1 {\boldsymbol{W}^{\mathrm{b}}}^{\mathrm{H}} \boldsymbol{a}_1(\boldsymbol{v}_1^{\mathrm{b}}) \boldsymbol{a}_2^{\mathrm{H}}(\boldsymbol{v}_2^{\mathrm{b}}) \boldsymbol{\eta}_2^{\mathrm{b}} + {\boldsymbol{W}^{\mathrm{b}}}^{\mathrm{H}} \boldsymbol{\eta}_1^{\mathrm{b}} + {\boldsymbol{W}^{\mathrm{b}}}^{\mathrm{H}} \boldsymbol{n}_1(t). \tag{4.11}$$

As in (4.8), the covariance matrix of $\boldsymbol{z}_1(t)$ can be given as

$$\boldsymbol{\Sigma}_{\boldsymbol{z}_1(t)} = \sigma_{\mathrm{z}}^2 {\boldsymbol{W}^{\mathrm{b}}}^{\mathrm{H}} \boldsymbol{W}^{\mathrm{b}}. \tag{4.12}$$

Note that the received noise $\boldsymbol{z}_1(t)$, including the additive distortion noise $\boldsymbol{\eta}_1^{\mathrm{b}}$, $\boldsymbol{\eta}_2^{\mathrm{b}}$ and the additive white Gaussian noise $\boldsymbol{n}_1(t)$, is unknown. However, to assess deviations for the FIM, only the covariance matrix $\boldsymbol{\Sigma}_{\boldsymbol{z}_1(t)}$ is needed. The same applies to the forward transmission.

4.3 Clock synchronization and FIM of channel parameters

Using OWL or one of the two protocols (RLP or CLP) in Fig. 4.2, different timing scenarios change the procedure of the localization and consequently the error bounds. In other words, the FIM elements of the channel and temporal parameters depend on the synchronization protocol. Since the contents of the forwarded and received signals do not rely on any timing

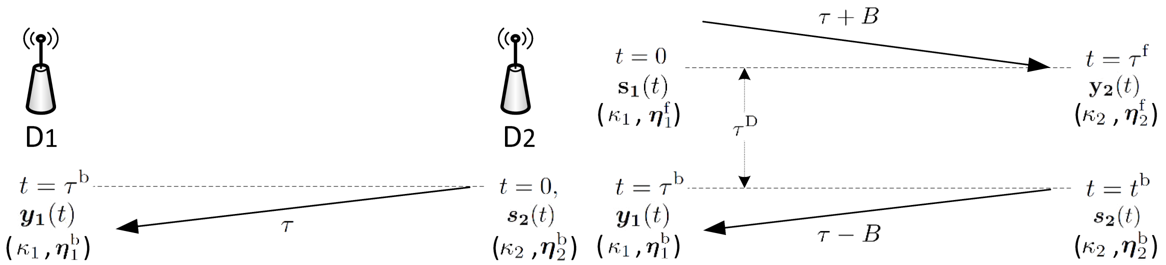

(a) One-way localization (b) Round-trip localization protocol

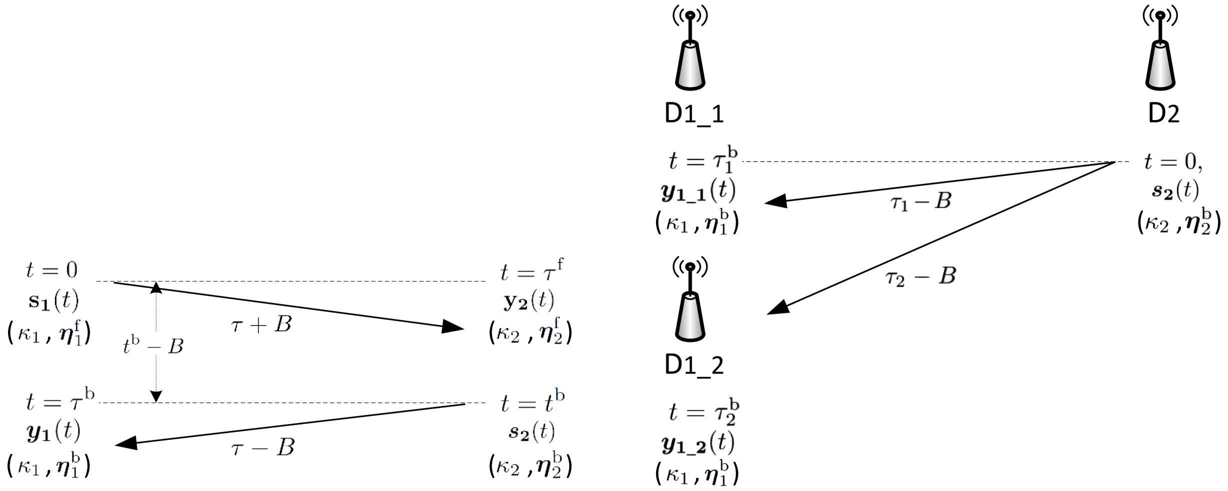

(c) Collaborative localization protocol (d) One-way localization with two anchors

Figure 4.2: Timing diagrams for the one-way and two-way localization protocols RLP and CLP.

protocols, for all of the following derivations, we assume that the temporal parameters are independent from the spatial ones.

4.3.1 One-Way Localization (OWL)- case 1

Considering one transmission in the OWL, the UE and BS are assumed to be synchronized. This can be used as a benchmark when assessing other techniques. Focusing only on the backward transmission (Fig. 4.2a), D_2 initiates communication by sending a signal $\boldsymbol{s_2}(t)$ at $t = 0$. After $\tau = \tau^{\mathrm{b}}$ seconds, the signal $\boldsymbol{y_1}(t)$ is received by D_1. At this point, the estimation procedure for the spatial parameters $\boldsymbol{\varphi}_{\mathrm{S-OWL}} \triangleq \{\boldsymbol{v}^{\mathrm{b}}, \boldsymbol{\beta}, \kappa\}$ and the temporal parameter τ is performed by D_1, where $\boldsymbol{v}^{\mathrm{b}} \triangleq \{\boldsymbol{v_1}^{\mathrm{b}}, \boldsymbol{v_2}^{\mathrm{b}}\}$, $\boldsymbol{\beta} \triangleq \{\beta_{\mathrm{R}}, \beta_{\mathrm{I}}\}$ and $\kappa \triangleq \kappa_1\kappa_2$. Finally, the corresponding FIM of the OWL parameters $\boldsymbol{\varphi}_{\mathrm{OWL}} \triangleq \{\boldsymbol{\varphi}_{\mathrm{S-OWL}}, \tau\}$ is given below

$$\boldsymbol{J}_{\boldsymbol{\varphi}_{\mathrm{OWL}}} = \begin{bmatrix} \boldsymbol{J}_{\boldsymbol{v}^{\mathrm{b}}\boldsymbol{v}^{\mathrm{b}}} & \boldsymbol{J}_{\boldsymbol{v}^{\mathrm{b}}\boldsymbol{\beta}} & \boldsymbol{j}_{\boldsymbol{v}^{\mathrm{b}}\kappa} & \boldsymbol{0} \\ \boldsymbol{J}_{\boldsymbol{\beta}\boldsymbol{v}^{\mathrm{b}}} & \boldsymbol{J}_{\boldsymbol{\beta}\boldsymbol{\beta}} & \boldsymbol{j}_{\boldsymbol{\beta}\kappa} & \boldsymbol{0} \\ \boldsymbol{j}_{\kappa\boldsymbol{v}^{\mathrm{b}}} & \boldsymbol{j}_{\kappa\boldsymbol{\beta}} & J_{\kappa\kappa} & 0 \\ \boldsymbol{0} & \boldsymbol{0} & 0 & J_{\tau\tau} \end{bmatrix} \in \mathbb{R}^{8\times 8}. \tag{4.13}$$

Note that $\boldsymbol{J}$, $\boldsymbol{j}$ and J represent matrix, vector and scalar, respectively. The scalar elements inside $\boldsymbol{J}_{\boldsymbol{\varphi}_{\mathrm{OWL}}}$ are found using $\boldsymbol{\mu_1}(t)$ in (4.10) and through the following formula [84]

$$\begin{aligned} J_{\mathrm{x,y}} = & \frac{\mathrm{T}_0 N_B^2}{(\sigma_{\mathrm{z}}^2)^2}\left(\frac{\partial}{\partial \mathrm{x}}\sigma_{\mathrm{z}}^2\right)\left(\frac{\partial}{\partial \mathrm{y}}\sigma_{\mathrm{z}}^2\right) \\ & + \frac{1}{\sigma_{\mathrm{z}}^2}\int_0^{T_0}\Bigg[\left(\frac{\partial}{\partial \mathrm{x}}\boldsymbol{\mu_1(t)}\right)^{\mathrm{H}}(\boldsymbol{W}^{\mathrm{b}^{\mathrm{H}}}\boldsymbol{W}^{\mathrm{b}})^{-1}\left(\frac{\partial}{\partial \mathrm{y}}\boldsymbol{\mu_1(t)}\right) \\ & + \left(\frac{\partial}{\partial \mathrm{y}}\boldsymbol{\mu_1(t)}\right)^{\mathrm{H}}(\boldsymbol{W}^{\mathrm{b}^{\mathrm{H}}}\boldsymbol{W}^{\mathrm{b}})^{-1}\left(\frac{\partial}{\partial \mathrm{x}}\boldsymbol{\mu_1(t)}\right)\Bigg]\mathrm{d}t, \end{aligned} \tag{4.14}$$

where $T_0 \approx N_{\mathrm{s}}T_{\mathrm{s}}$ is the observation time with a number of symbols N_{s} and a symbol period T_{s}. Note that the output of (4.14) is a real scalar element. The full derivation of FIM entries is given in Appendix B.1.

Having noted the independence of the temporal parameter τ from the spatial parameters $\boldsymbol{\varphi}_{\mathbf{S-OWL}}$, and in order to focus on the channel parameter $\boldsymbol{v}^{\mathbf{b}}$, we remove the interaction of the nuisance parameters $\boldsymbol{\varphi}_{\mathrm{N}} \triangleq \{\boldsymbol{\beta}, \kappa\}$ from our desired channel parameters using the concept of equivalent FIM (EFIM) [17]. As a result, we write $\boldsymbol{J}_{\boldsymbol{\varphi}_{\mathrm{S-OWL}}}$ in block form as

$$\boldsymbol{J}_{\boldsymbol{\varphi}_{\mathrm{S-OWL}}} = \begin{bmatrix} \boldsymbol{J}_{\boldsymbol{\upsilon}^{\mathrm{b}}\boldsymbol{\upsilon}^{\mathrm{b}}} & \boldsymbol{J}_{\boldsymbol{\upsilon}^{\mathrm{b}}\mathrm{N}} \\ \boldsymbol{J}_{\boldsymbol{\upsilon}^{\mathrm{b}}\mathrm{N}}^{\mathrm{T}} & \boldsymbol{J}_{\mathrm{N}} \end{bmatrix}, \in \mathbb{R}^{7\times 7}, \tag{4.15}$$

where $\boldsymbol{J}_{\boldsymbol{\upsilon}^{\mathrm{b}}\boldsymbol{\upsilon}^{\mathrm{b}}} \in \mathbb{R}^{4\times 4}$ is the desired channel parameter matrix, $\boldsymbol{J}_{\mathrm{N}} \in \mathbb{R}^{3\times 3}$ is the nuisance parameter matrix, and $\boldsymbol{J}_{\boldsymbol{\upsilon}^{\mathrm{b}}\mathrm{N}} \in \mathbb{R}^{4\times 3}$ is the mutual information of the channel and nuisance parameters' matrix. Consequently, using the Schur complement [90], the EFIM of $\boldsymbol{J}_{\boldsymbol{\upsilon}^{\mathrm{b}}\boldsymbol{\upsilon}^{\mathrm{b}}}$ is obtained as

$$\boldsymbol{J}^{\mathrm{e}}_{\boldsymbol{\upsilon}^{\mathrm{b}}\boldsymbol{\upsilon}^{\mathrm{b}}} = \boldsymbol{J}_{\boldsymbol{\upsilon}^{\mathrm{b}}\boldsymbol{\upsilon}^{\mathrm{b}}} - \boldsymbol{J}_{\boldsymbol{\upsilon}^{\mathrm{b}}\mathrm{N}} \boldsymbol{J}_{\mathrm{N}}^{-1} \boldsymbol{J}_{\boldsymbol{\upsilon}^{\mathrm{b}}\mathrm{N}}^{\mathrm{T}} \quad \in \mathbb{R}^{4\times 4}. \tag{4.16}$$

4.3.2 One-Way Localization (OWL) using two anchors- case 2

In order to take into consideration the asynchronous OWL condition, and to compensate for the clock bias, two anchors with the same HWIs' factors, D_{1_1} and D_{1_2}, can be used. To ensure a fair comparison with the other protocols, the second anchor is assumed to be located at the known position $\boldsymbol{p_2}$ in the closest neighboring cell to the D_2 of the current cell (see Fig. 4.3).

Similar to what was seen in case 1, D_2 initiates communication by sending a signal $\boldsymbol{s_2}(t)$ to both anchors separately. Afterwards, signals $\boldsymbol{y_{1\_1}}(t)$ and $\boldsymbol{y_{1\_2}}(t)$ are received by anchors D_{1_1} and D_{1_2} after $\tau_1^{\mathrm{b}} = \tau_1 - B$ and $\tau_2^{\mathrm{b}} = \tau_2 - B$ seconds, respectively. In this case, we assume that only the temporal information of the second anchor is used. Therefore, the second anchor D_{1_2} estimates ToA as $\hat{\tau}_2^{\mathrm{b}}$ and forwards it to the first anchor D_{1_1} using

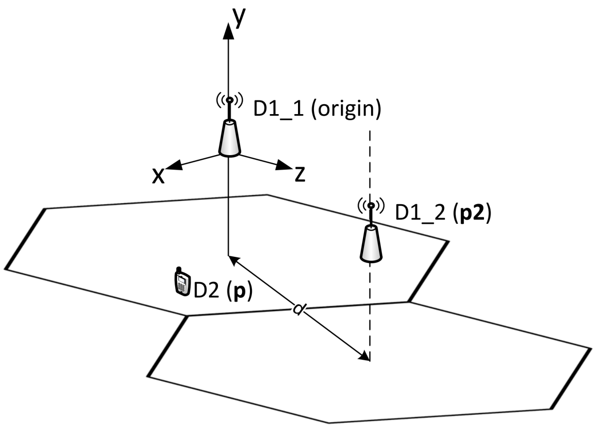

Figure 4.3: Considered scenario for the OWL including two anchors on two neighborhood cells.

an error-free link.

At this stage, D_{1_1} localizes D_2 using the temporal parameter of D_{1_2} as well as its own temporal and angular parameters, τ_1^{b} and $\boldsymbol{\varphi}_{\mathrm{S-OWL}}$, respectively. The FIM of the OWL parameters, $\boldsymbol{J}_{\boldsymbol{\varphi}_{\mathrm{S-OWL}}}$, and the EFIM of its angular parameters are the same ones seen in (4.15) and (4.16). In terms of the temporal component, based on Fig. 4.2d and using the time difference of arrival (TDoA)[1] technique, the clock offset can be eliminated as

$$\tau' \triangleq \hat{\tau}_1^{\mathrm{b}} - (\hat{\tau}_2^{\mathrm{b}}) = \tau_1 - \tau_2 + e, \tag{4.17}$$

where e is the estimation error. Both temporal parameters τ_1 and τ_2 are used in the localization procedure. Since they are gained through two independent paths, they are also transformed independently, as will be shown in the next section.

---

[1] In the TDoA technique, three anchors are needed to localize the user; however, in our scenario, TDoA is used to only estimate the temporal parameter, which is possible with just two anchors. We use the TDoA notation to explain the procedure.

4.3.3 One-Way Localization (OWL) using two anchors- case 3

Similar to case 2, two anchors are used here. The localization procedure in this case is identical to that of the second case; however, the angular information of the second anchor is used in addition to the other information gained in the last subsection. The FIM of the spatial parameters for anchor 1, $\boldsymbol{J}^{A1}_{\boldsymbol{\varphi}_{\mathrm{S-OWL}}}$, is the same as the one in (4.15) (i.e, $\boldsymbol{J}^{A1}_{\boldsymbol{\varphi}_{\mathrm{S-OWL}}} = \boldsymbol{J}_{\boldsymbol{\varphi}_{\mathrm{S-OWL}}}$) and therefore, ${\boldsymbol{J}^{\mathrm{e}}_{\boldsymbol{\upsilon}^{\mathrm{b}}\boldsymbol{\upsilon}^{\mathrm{b}}}}^{A1} = \boldsymbol{J}^{\mathrm{e}}_{\boldsymbol{\upsilon}^{\mathrm{b}}\boldsymbol{\upsilon}^{\mathrm{b}}}$. However, the FIM of the spatial parameters for anchor 2 is different from that of anchor 1 since the AoA, AoD and the channel gain will be different.

$$\boldsymbol{J}^{A2}_{\boldsymbol{\varphi}_{\mathrm{S-OWL}}} = \begin{bmatrix} \boldsymbol{J}^{A2}_{\boldsymbol{\upsilon}^{\mathrm{b}}\boldsymbol{\upsilon}^{\mathrm{b}}} & \boldsymbol{J}^{A2}_{\boldsymbol{\upsilon}^{\mathrm{b}}\mathrm{N}} \\ \\ {\boldsymbol{J}^{A2}_{\boldsymbol{\upsilon}^{\mathrm{b}}\mathrm{N}}}^{\mathrm{T}} & \boldsymbol{J}^{A2}_{\mathrm{N}} \end{bmatrix}, \in \mathbb{R}^{7\times 7}. \tag{4.18}$$

Consequently, the EFIM of the angles becomes

$${\boldsymbol{J}^{\mathrm{e}}_{\boldsymbol{\upsilon}^{\mathrm{b}}\boldsymbol{\upsilon}^{\mathrm{b}}}}^{A2} = \boldsymbol{J}^{A2}_{\boldsymbol{\upsilon}^{\mathrm{b}}\boldsymbol{\upsilon}^{\mathrm{b}}} - \boldsymbol{J}^{A2}_{\boldsymbol{\upsilon}^{\mathrm{b}}\mathrm{N}} {\boldsymbol{J}^{A2}_{\mathrm{N}}}^{-1} {\boldsymbol{J}^{A2}_{\boldsymbol{\upsilon}^{\mathrm{b}}\mathrm{N}}}^{\mathrm{T}}. \tag{4.19}$$

The temporal parameter FIM is similar to that of case 2. Afterwards, the obtained EFIM of the second anchor's angular and temporal parameters are added to the ones gained through the first anchor, as will be shown in the next section.

4.3.4 Round-Trip Localization Protocol (RLP)

According to Fig. 4.2b, the steps for D_2 positioning using the RLP can be summarized as follows [61]

- At $t = 0$ signal $\boldsymbol{s}_1(t)$ is sent by D_1.

- After $\tau^{\mathrm{f}} = \tau + B$ seconds, the signal $\boldsymbol{y}_2(t)$ arrives at D_2.
- At this point, D_2 estimates ToA as $\hat{\tau}^{\mathrm{f}}$ and after a pre-agreed delay τ^{D}, signal $\boldsymbol{s}_2(t)$ is sent at $t^{\mathrm{b}} = \hat{\tau}^{\mathrm{f}} + \tau^{\mathrm{D}}$.
- $\tau - B$ seconds later, the signal $\boldsymbol{y}_1(t)$ is received by D_1 at $\tau^{\mathrm{b}} = t^{\mathrm{b}} + \tau - B$.
- Finally, the spatial parameters $\boldsymbol{\varphi}_{\mathrm{S-RLP}} = \boldsymbol{\varphi}_{\mathrm{S-OWL}}$ and the temporal parameter τ^{b} are estimated by D_1.

Note that since the offset parameter B vanishes from $\boldsymbol{y}_1(t)$ after one round trip, there is no longer a need to estimate it. Hence, we can present the corresponding FIM of the RLP parameters $\boldsymbol{\varphi}_{RLP} \triangleq \{\boldsymbol{\varphi}_{\mathrm{S-RLP}}, \tau\}$, to be the same as the one in (4.13). Similar to the OWL, the elements of the spatial parameters $\boldsymbol{J}_{\boldsymbol{\varphi}_{\mathrm{S-RLP}}}$ are calculated through (4.14). Unlike OWL, the temporal FIM $J_{\tau\tau}$ is derived after some mathematical treatment from the forward and backward ToAs

$$J_{\tau\tau} = 4 \left(J^{-1}_{\tau^{\mathrm{f}}\tau^{\mathrm{f}}} + J^{-1}_{\tau^{\mathrm{b}}\tau^{\mathrm{b}}} \right)^{-1}, \tag{4.20}$$

where $J_{\tau^{\mathrm{f}}\tau^{\mathrm{f}}}$ and $J_{\tau^{\mathrm{b}}\tau^{\mathrm{b}}}$ are the forward and backward temporal FIM, respectively. The first one is found using $\boldsymbol{\mu_2}(t)$, while the latter is found through $\boldsymbol{\mu_1}(t)$. Note that by setting $J_{\tau\tau} = J_{\tau^{\mathrm{b}}\tau^{\mathrm{b}}}$, temporal FIM for the OWL is achieved.

Similar to what was seen in the OWL cases, we need to extract the channel information from the spatial parameter FIM. To that end, as in (4.16), $\boldsymbol{J}^{\mathrm{e}}_{\boldsymbol{v}^{\mathrm{b}}\boldsymbol{v}^{\mathrm{b}}}$ for RLP is derived.

4.3.5 Collaborative Localization Protocol (CLP)

As can be inferred from the name of this protocol, localization of D_2 is done at D_1 through the cooperation of both the forward and backward transmissions, in which the received signal at D_2 is assumed to be fed back to D_1 via an error-free link. Unlike the RLP protocol, t^{b} is a pre-agreed time at D_2 where $\boldsymbol{s}_2(t)$ is sent on a non-overlapping interval with the forward transmission.

Now, since t^{b} is selected independently of the forward transmission, the FIM of the spatial parameters in both transmissions can be added to give us more information about the location of D_2. Furthermore, in this protocol, because the localization is performed at both transmissions, the offset B needs to be estimated and is part of the following forward and backward CLP parameters:

$$\boldsymbol{\varphi}^{\mathrm{f}}_{\mathrm{CLP}} \triangleq \{\boldsymbol{\varphi}^{\mathrm{f}}_{\mathrm{S-CLP}}, \tau^{\mathrm{f}}, B\},$$
$$\boldsymbol{\varphi}^{\mathrm{b}}_{\mathrm{CLP}} \triangleq \{\boldsymbol{\varphi}^{\mathrm{b}}_{\mathrm{S-CLP}}, \tau^{\mathrm{b}}, B\},$$

where

$$\boldsymbol{\varphi}^{\mathrm{f}}_{\mathrm{S-CLP}} \triangleq \{\boldsymbol{\upsilon}^{\mathrm{f}}, \boldsymbol{\beta}, \kappa\},$$
$$\boldsymbol{\varphi}^{\mathrm{b}}_{\mathrm{S-CLP}} \triangleq \{\boldsymbol{\upsilon}^{\mathrm{b}}, \boldsymbol{\beta}, \kappa\},$$

and $\boldsymbol{\upsilon}^{\mathrm{f}} \triangleq \{\boldsymbol{\upsilon_1}^{\mathrm{f}}, \boldsymbol{\upsilon_2}^{\mathrm{f}}\}$.

The FIM of the CLP parameters for the forward transmission can be given as

$$\boldsymbol{J}^{\mathrm{f}}_{\boldsymbol{\varphi}_{\mathrm{CLP}}} = \begin{bmatrix} \boldsymbol{J}_{\boldsymbol{v}^{\mathrm{f}}\boldsymbol{v}^{\mathrm{f}}} & \boldsymbol{J}_{\boldsymbol{v}^{\mathrm{f}}\boldsymbol{\beta}} & \boldsymbol{j}_{\boldsymbol{v}^{\mathrm{f}}\kappa} & \mathbf{0} & \mathbf{0} \\ \boldsymbol{J}_{\boldsymbol{\beta}\boldsymbol{v}^{\mathrm{f}}} & \boldsymbol{J}_{\boldsymbol{\beta}\boldsymbol{\beta}} & \boldsymbol{j}_{\boldsymbol{\beta}\kappa} & \mathbf{0} & \mathbf{0} \\ \boldsymbol{j}_{\kappa\boldsymbol{v}^{\mathrm{f}}} & \boldsymbol{j}_{\kappa\boldsymbol{\beta}} & J_{\kappa\kappa} & 0 & 0 \\ \mathbf{0} & \mathbf{0} & 0 & J_{\tau^{\mathrm{f}}\tau^{\mathrm{f}}} & J_{\tau^{\mathrm{f}}B} \\ \mathbf{0} & \mathbf{0} & 0 & J_{\tau^{\mathrm{f}}B} & J_{BB} \end{bmatrix}, \in \mathbb{R}^{9\times 9} \tag{4.21}$$

where we define the rightmost bottom of the matrix in (4.21) as $\boldsymbol{J}^{\mathrm{f}}_{\mathrm{TT}} \triangleq \begin{bmatrix} J_{\tau^{\mathrm{f}}\tau^{\mathrm{f}}} & J_{\tau^{\mathrm{f}}B} \\ J_{\tau^{\mathrm{f}}B} & J_{BB} \end{bmatrix}$. The backward temporal FIM $\boldsymbol{J}^{\mathrm{b}}_{\mathrm{TT}}$ can be similarly defined. By transforming $\boldsymbol{J}^{\mathrm{f}}_{\mathrm{TT}}$ and $\boldsymbol{J}^{\mathrm{b}}_{\mathrm{TT}}$ into the temporal parameters $\{\tau, B\}$ and then adding them, the formula for the EFIM of $J_{\tau\tau}$, is found to be same as the one in (4.20). Moreover, the corresponding EFIM matrix for the forward and backward channel parameters, ${\boldsymbol{J}_{\boldsymbol{v}^{\mathrm{f}}\boldsymbol{v}^{\mathrm{f}}}}^{\mathrm{e}}$ and ${\boldsymbol{J}_{\boldsymbol{v}^{\mathrm{b}}\boldsymbol{v}^{\mathrm{b}}}}^{\mathrm{e}}$, are similar to (4.16).

4.4 FIM of the location parameters

In order to compute the position and orientation error bounds, we need to transfer the EFIM derived in the last section to the location domain. To that effect, we define the forward and backward channel parameters as $\boldsymbol{\varphi}^{\mathrm{f}}_{\mathrm{CH}} \triangleq \{\boldsymbol{v}^{\mathrm{f}}, \tau\}$ and $\boldsymbol{\varphi}^{\mathrm{b}}_{\mathrm{CH}} \triangleq \{\boldsymbol{v}^{\mathrm{b}}, \tau\}$. We also define the location parameters as $\boldsymbol{\varphi}_{\mathrm{L}} \triangleq \{\boldsymbol{p}, \boldsymbol{o}\}$. The EFIM of location parameters $\boldsymbol{J}^{\mathrm{e}}_{\mathrm{L-OWL1}}$, $\boldsymbol{J}^{\mathrm{e}}_{\mathrm{L-OWL2}}$, $\boldsymbol{J}^{\mathrm{e}}_{\mathrm{L-OWL3}}$, $\boldsymbol{J}^{\mathrm{e}}_{\mathrm{L-RLP}}$ and $\boldsymbol{J}^{\mathrm{e}}_{\mathrm{L-CLP}}$, for the cases studied (i.e., OWL cases 1-3, RLP and CLP protocols) are found through the following transformation matrix $\mathbf{\Lambda}^{\mathbf{f}\backslash\mathbf{b}}$, respectively.

$$\mathbf{\Lambda}^{\mathrm{f}\backslash\mathrm{b}} \triangleq \frac{\partial \boldsymbol{\varphi}_{\mathrm{CH}}^{\mathrm{f}\backslash\mathrm{b}}}{\partial \boldsymbol{\varphi}_{\mathrm{L}}} = \left[\underbrace{\begin{array}{c} \frac{\partial \boldsymbol{\upsilon}^{\mathrm{f}\backslash\mathrm{b}}}{\partial \boldsymbol{p}} \\ \frac{\partial \boldsymbol{\upsilon}^{\mathrm{f}\backslash\mathrm{b}}}{\partial \boldsymbol{o}} \end{array}}_{\mathbf{\Lambda}_{\mathrm{S}}^{\mathrm{f}\backslash\mathrm{b}}} \middle| \underbrace{\begin{array}{c} \frac{\partial \tau}{\partial \boldsymbol{p}} \\ \frac{\partial \tau}{\partial \boldsymbol{o}} \end{array}}_{\mathbf{\Lambda}_{\tau}} \right], \ \in \mathbb{R}^{5\times 5}, \tag{4.22}$$

where the spatial and temporal transformation matrices are denoted by $\mathbf{\Lambda}_{\mathrm{S}}^{\mathrm{f}\backslash\mathrm{b}} \in \mathbb{R}^{5\times 4}$ and $\mathbf{\Lambda}_{\tau} \in \mathbb{R}^{5\times 1}$, respectively. Note[2] that the backward spatial transformation matrix $\mathbf{\Lambda}_{\mathrm{S}}^{\mathrm{b}}$ is different from the forward one $\mathbf{\Lambda}_{\mathrm{S}}^{\mathrm{f}}$.

Furthermore, in (4.22), for the second anchor in the OWL cases 2 and 3, $\tau = \tau_2^{\mathrm{b}}$ is different from the one in case 1, where $\tau = \tau_1^{\mathrm{b}}$ ($\tau_2^{\mathrm{b}} = \|\boldsymbol{p} - \boldsymbol{p_2}\|/c$ for the second anchor and $\tau_1^{\mathrm{b}} = \|\boldsymbol{p}\|/c$ for the first anchor. The same idea is applied to the spatial transformation matrix $\mathbf{\Lambda}_{\mathrm{S}}^{\mathrm{b}}$, where $\mathbf{\Lambda}_{\mathrm{S}}^{\mathrm{b}} = \mathbf{\Lambda}_{\mathrm{S}_1}^{\mathrm{b}}$ for the first anchor and $\mathbf{\Lambda}_{\mathrm{S}}^{\mathrm{b}} = \mathbf{\Lambda}_{\mathrm{S}_2}^{\mathrm{b}}$ for the second one. Then, as discussed in the last section, we conclude that

$$\boldsymbol{J}_{\mathrm{L-OWL1}}^{\mathrm{e}} \triangleq \mathbf{\Lambda}_{\mathrm{S}}^{\mathrm{b}} \boldsymbol{J}_{\boldsymbol{\upsilon}^{\mathrm{b}}\boldsymbol{\upsilon}^{\mathrm{b}}}^{\mathrm{e}} \mathbf{\Lambda}_{\mathrm{S}}^{\mathrm{b}\,\mathrm{T}} + J_{\tau^{\mathrm{b}}\tau^{\mathrm{b}}} \mathbf{\Lambda}_{\tau} \mathbf{\Lambda}_{\tau}^{\mathrm{T}}, \tag{4.23a}$$

$$\boldsymbol{J}_{\mathrm{L-OWL2}}^{\mathrm{e}} \triangleq \mathbf{\Lambda}_{\mathrm{S}_1}^{\mathrm{b}} \boldsymbol{J}_{\boldsymbol{\upsilon}^{\mathrm{b}}\boldsymbol{\upsilon}^{\mathrm{b}}}^{\mathrm{e}}{}^{\mathit{A1}} \mathbf{\Lambda}_{\mathrm{S}_1}^{\mathrm{b}}{}^{\mathrm{T}} + J_{\tau_1^{\mathrm{b}}\tau_1^{\mathrm{b}}} \mathbf{\Lambda}_{\tau} \mathbf{\Lambda}_{\tau}^{\mathrm{T}} + J_{\tau_2^{\mathrm{b}}\tau_2^{\mathrm{b}}} \mathbf{\Lambda}_{\tau} \mathbf{\Lambda}_{\tau}^{\mathrm{T}}, \tag{4.23b}$$

$$\begin{aligned} \boldsymbol{J}_{\mathrm{L-OWL3}}^{\mathrm{e}} \triangleq{} & \mathbf{\Lambda}_{\mathrm{S}_1}^{\mathrm{b}} \boldsymbol{J}_{\boldsymbol{\upsilon}^{\mathrm{b}}\boldsymbol{\upsilon}^{\mathrm{b}}}^{\mathrm{e}}{}^{\mathit{A1}} \mathbf{\Lambda}_{\mathrm{S}_1}^{\mathrm{b}}{}^{\mathrm{T}} + \mathbf{\Lambda}_{\mathrm{S}_2}^{\mathrm{b}} \boldsymbol{J}_{\boldsymbol{\upsilon}^{\mathrm{b}}\boldsymbol{\upsilon}^{\mathrm{b}}}^{\mathrm{e}}{}^{\mathit{A2}} \mathbf{\Lambda}_{\mathrm{S}_2}^{\mathrm{b}}{}^{\mathrm{T}} \\ & + J_{\tau_1^{\mathrm{b}}\tau_1^{\mathrm{b}}} \mathbf{\Lambda}_{\tau} \mathbf{\Lambda}_{\tau}^{\mathrm{T}} + J_{\tau_2^{\mathrm{b}}\tau_2^{\mathrm{b}}} \mathbf{\Lambda}_{\tau} \mathbf{\Lambda}_{\tau}^{\mathrm{T}}, \end{aligned} \tag{4.23c}$$

$$\boldsymbol{J}_{\mathrm{L-RLP}}^{\mathrm{e}} \triangleq \mathbf{\Lambda}_{\mathrm{S}}^{\mathrm{b}} \boldsymbol{J}_{\boldsymbol{\upsilon}^{\mathrm{b}}\boldsymbol{\upsilon}^{\mathrm{b}}}^{\mathrm{e}} \mathbf{\Lambda}_{\mathrm{S}}^{\mathrm{b}\,\mathrm{T}} + J_{\tau\tau} \mathbf{\Lambda}_{\tau} \mathbf{\Lambda}_{\tau}^{\mathrm{T}}, \tag{4.23d}$$

$$\boldsymbol{J}_{\mathrm{L-CLP}}^{\mathrm{e}} \triangleq \mathbf{\Lambda}_{\mathrm{S}}^{\mathrm{f}} \boldsymbol{J}^{\mathrm{e}}{}_{\boldsymbol{\upsilon}^{\mathrm{f}}\boldsymbol{\upsilon}^{\mathrm{f}}} \mathbf{\Lambda}_{\mathrm{S}}^{\mathrm{f}\,\mathrm{T}} + \mathbf{\Lambda}_{\mathrm{S}}^{\mathrm{b}} \boldsymbol{J}^{\mathrm{e}}{}_{\boldsymbol{\upsilon}^{\mathrm{b}}\boldsymbol{\upsilon}^{\mathrm{b}}} \mathbf{\Lambda}_{\mathrm{S}}^{\mathrm{b}\,\mathrm{T}} + J_{\tau\tau} \mathbf{\Lambda}_{\tau} \mathbf{\Lambda}_{\tau}^{\mathrm{T}}. \tag{4.23e}$$

The temporal components of (4.23b) and (4.23c) are explained in detail in appendix B.2.

---

[2] The AoA and AoD angles are exchanged in the forward and backward transmissions.

Finally, the PEB and OEB of D_2 can be derived as

$$\mathrm{PEB} = \sqrt{[\mathbf{C}]_{1,1} + [\mathbf{C}]_{2,2} + [\mathbf{C}]_{3,3}}\ , \tag{4.24a}$$

$$\mathrm{OEB} = \sqrt{[\mathbf{C}]_{4,4} + [\mathbf{C}]_{5,5}}\ , \tag{4.24b}$$

where $[\mathbf{C}]_{i,j}$ is the $(i,j)^{th}$ element of the obtained $\boldsymbol{J}_{\mathrm{L}}^{\mathrm{e}}$. As can be seen from (4.23), the RLP gives more information about the temporal parameter in comparison with OWL-case 1, and this occurs because it has one more transmission. However, the information that we earn using the CLP and OWL-case 3 is almost twice that from the RLP. Consequently, the CLP, at the cost of greater complexity, and OWL cases 2 and 3, at the cost of a second anchor, cause less error in localization than the RLP. In the next section, we examine whether or not this extra information compensates for the localization error due to HWIs.

4.5 Discussions and Numerical results

4.5.1 Simulation setup

In this simulation, we consider a scenario where the initiation of transmission in TWL occurs at the BS. There, we have D_1 lying on the xz-plane with $N_1 = 12 \times 12$ URA antennas located at the origin, each with height $h_{\mathrm{BS}} = 10\ m$. The UE is considered to be D_2, operating at frequency $f = 38$ GHz, with $N_2 = 12 \times 12$ URA antennas and located anywhere in a sector of hexagon cells on the plane $z = -h_{\mathrm{BS}} = -10\ m$ with a radius of 50 meters. However, in the OWL case, the UE initiates communication by what is known as uplink transmission. In the OWL with two anchors, the first and second BS act as D_{1_1}

and D_{1_2}, respectively. The UE is also tilted by an orientation angle of 0 or 10 degrees in both azimuth and elevation. We use directional beamforming for all devices with $N_{\mathrm{B}} = 25$ beams. In the forward transmission Fig. 4.4a, the BS steers the beams towards the sector containing the UE with azimuth and elevation angles $\phi^{\mathrm{f}}_{1,l}$ and $\theta^{\mathrm{f}}_{1,l}, 1 \leq l \leq N_{\mathrm{B}}$ as

$$\boldsymbol{f}^{\mathrm{f}}_{l} \triangleq \frac{1}{\sqrt{N_{\mathrm{B}}}} \boldsymbol{a}_1(\phi_{1,l}, \theta_{1,l}),$$

where $\boldsymbol{a}_1(\phi_{1,l}, \theta_{1,l})$ is the array response vector towards the angles $\phi_{1,l}$ and $\theta_{1,l}$. We normalize the beamforming matrix $\boldsymbol{f}^{\mathrm{f}}_{l}$ to obtain trace$({\boldsymbol{F}^{\mathrm{f}}}^{\mathrm{H}} \boldsymbol{F}^{\mathrm{f}}) = 1$. On the other hand, in the backward transmission Fig. 4.4b, the UE replies to the BS by steering the transmission beams towards the virtual sector, containing the BS with azimuth and elevation angles $\phi^{\mathrm{b}}_{2,l}$ and $\theta^{\mathrm{b}}_{2,l}, 1 \leq l \leq N_{\mathrm{B}}$.

The receive beamforming $\boldsymbol{w}^{\mathrm{f}}_{l}, \boldsymbol{w}^{\mathrm{b}}_{l}$ and the backward transmit beamforming $\boldsymbol{f}^{\mathrm{b}}_{l}$ can be found in the same way.

The propagated beams are fixed and equispaced on the sectors containing the BS and UE. Moreover, as in [83], the transmitted signal is assumed to be passed through a unit energy ideal *sinc* pulse-shaping filter with bandwidth $W = 125\ MHz$ and $N_{\mathrm{s}} = 16$. We also set the noise variance to $N_0 = -110\ dBm$. In our simulation environment, we assume that the UE is moving among the 25 different locations in one sector of a cell. Finally, we average the simulations over 25 UE locations to obtain the PEB and OEB affected by initiator and responder HWIs. In this case, PEB and OEB degradation can be calculated

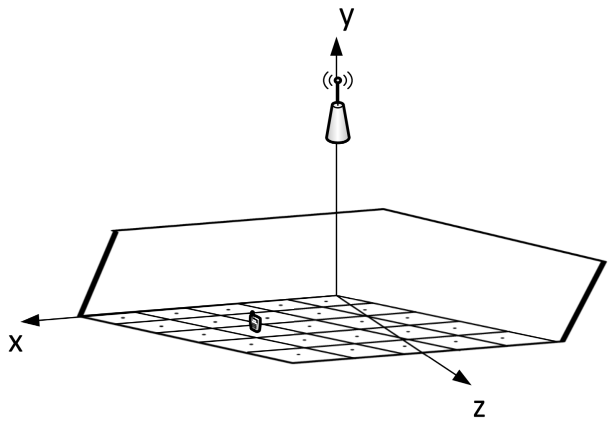

(a) Steered beams towards 25 different UE's location in forward transmission.

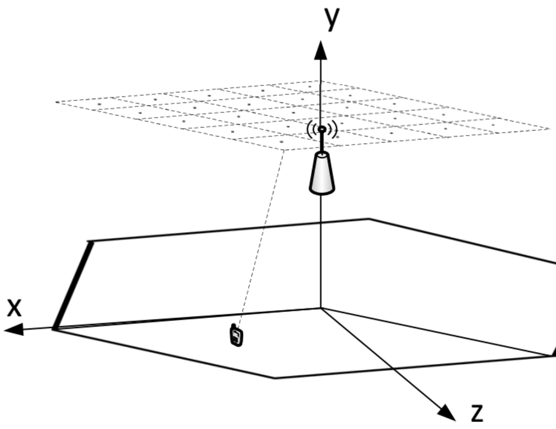

(b) Virtual sector containing 25 beams directed towards BS in backward transmission.

Figure 4.4: Forward and backward beam propagation.

as

$$\mathrm{PEB}_{\mathrm{deg}} = \left(\frac{\mathrm{PEB}_{\mathrm{HWIs}}}{\mathrm{PEB}_{\mathrm{ideal}}} - 1\right) \times 100\%, \tag{4.25}$$

$$\mathrm{OEB}_{\mathrm{deg}} = \left(\frac{\mathrm{OEB}_{\mathrm{HWIs}}}{\mathrm{OEB}_{\mathrm{ideal}}} - 1\right) \times 100\%. \tag{4.26}$$

where $\mathrm{PEB}_{\mathrm{ideal}}$ and $\mathrm{OEB}_{\mathrm{ideal}}$ are obtained using (4.24)

4.5.2 Performance Analysis

Fig. 4.5 illustrates the PEB with respect to the HWIs factor κ for the OWL cases and the two discussed protocols RLP and CLP. Based on the error vector magnitude (EVM) metrics on the data sheets of the RF transceivers, κ should be in the practical range [0.9,1] [65]. For this simulation, κ changes consistently within this interval. As can be seen from this figure, CLP outperforms RLP due to the additional spatial term. The CLP has better localization performance under different HWIs factors than the OWL cases as well. This is due to 1) the extra information in comparison with OWL cases 1 and 2, and 2) the closer distance between the BS and UE when compared to that between second BS and UE in OWL-case 3.

Moreover, RLP and OWL-case 1 follow the same curve with a minor increase, on the order of mm, in the performance of the RLP over that of the OWL-case 1. This is due to the fact that the temporal parameters are estimated twice. However, RLP mitigates the effect of imperfect synchronization between the transceivers. It is important to note that the HWIs have a severe impact on the system performance for all the mentioned protocols and, as expected, the PEB is at a minimum when $\kappa = 1$ (i.e., where there are no hardware imperfections at the transceivers).

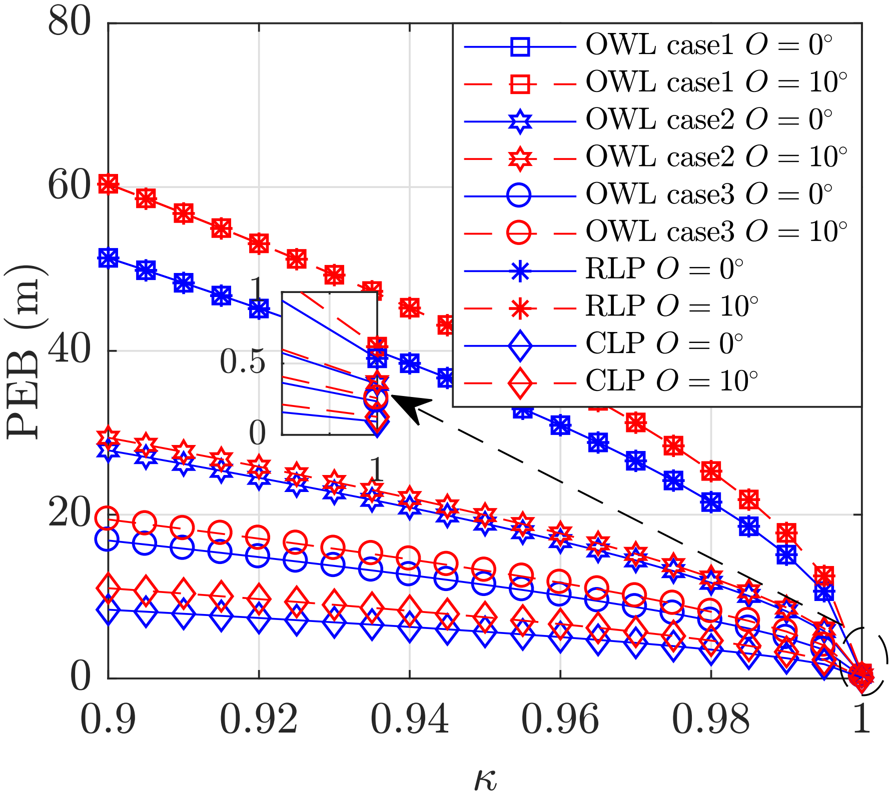

Figure 4.5: PEB w. r. t. κ considering two orientation angles $[0°; 0°]$ and $[10°; 10°]$ under the OWL, RLP and CLP.

Fig. 4.6 presents the PEB degradation level with respect to κ. As illustrated in the figure, when κ strays from 1, the PEB deteriorates less dramatically in OWL cases 1 and 2 as well as that in the CLP, than that in the RLP. The robustness of the CLP is even more evident for the oriented UE than the disoriented one; this indicates the strength of the CLP against misorientation.

Hence, two anchors can render mmWave localization more robust against HWIs. Moreover, the total loss caused by decreasing κ from 1 to 0.9 is the same for OWL case 1 and RLP. With no orientation, the worst total degradation is seen in the RLP and OWL case

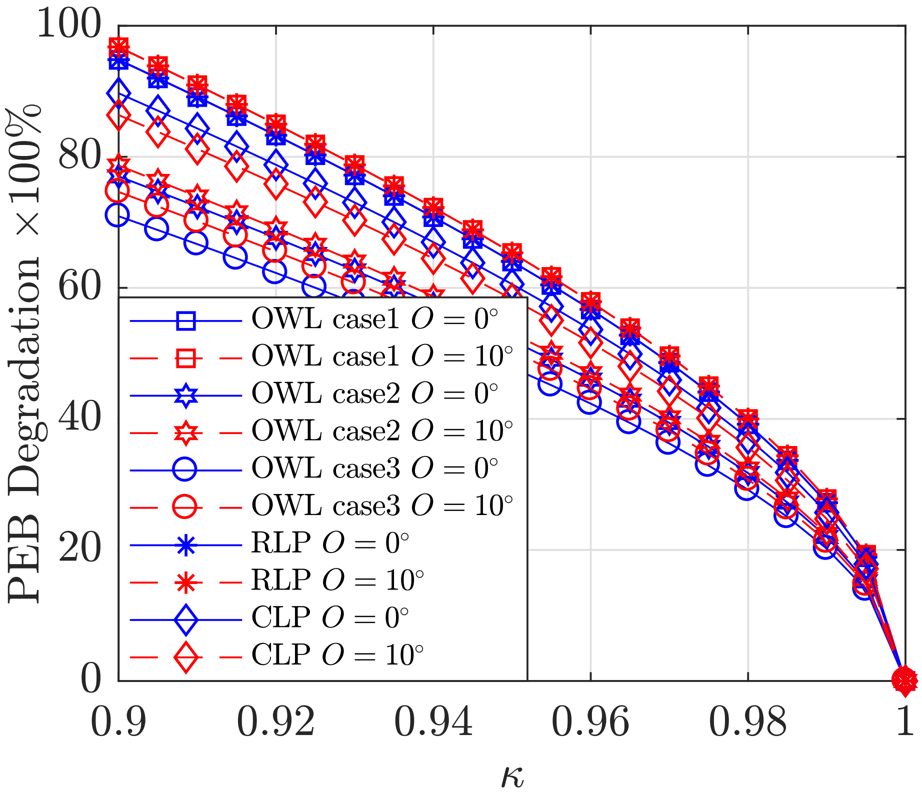

Figure 4.6: PEB degradation w. r. t. κ considering two orientation angles $[0^\circ; 0^\circ]$ and $[10^\circ; 10^\circ]$ under the OWL, RLP and CLP.

1, at $94.83 \times 100\%$. The smallest degradation, at $70.93 \times 100\%$, occurs when using two anchors in OWL-case 3. Needless to say, the degradation is quite enormous. Greater impairment causes more degradation for the RLP than for OWL-case 3; for instance, in the case of $\boldsymbol{o} = [0; 0]$, a $17.91 \times 100\%$ degradation difference can be noticed when $\kappa = 0.94$, as compared to $23.9 \times 100\%$ when $\kappa = 0.9$.

Fig. 4.7 presents the PEB percentage loss using the CLP with respect to both impairment factors κ_1 and κ_2. It is clear that the impact of the impaired BS and UE on the localization is the same and that the PEB is worsened by $89.7 \times 100\%$ at $\kappa_1 = \kappa_2 = \sqrt{0.94}$

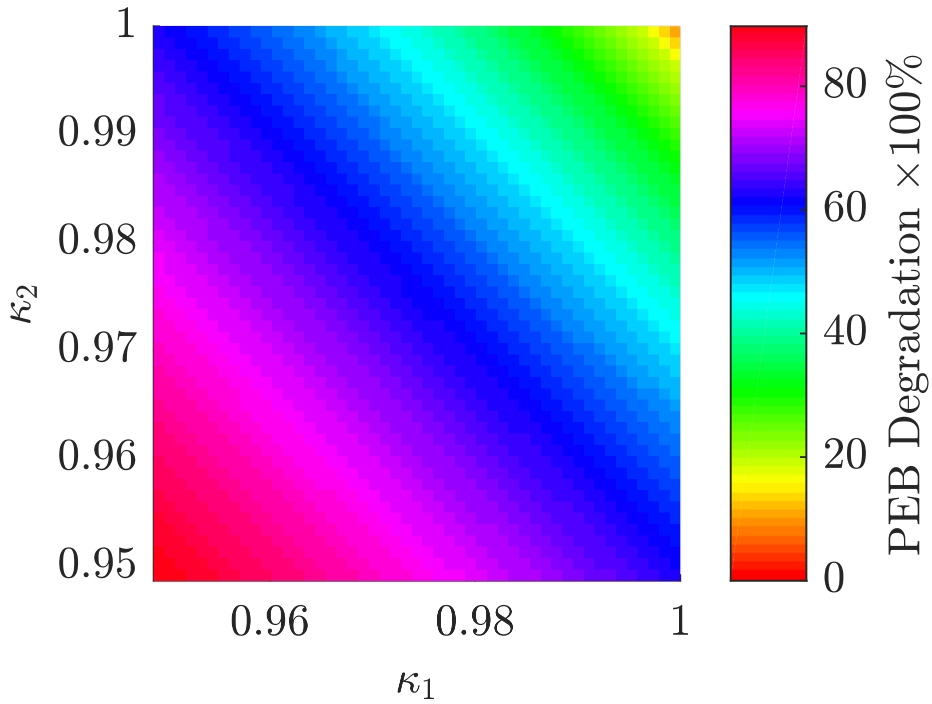

Figure 4.7: PEB degradation w. r. t. κ_1 and κ_2 with orientation angle $[0°; 0°]$ under the CLP.

($\kappa = 0.9$). The same trend can be observed for the PEB and OEB loss in all the other cases.

Figs. 4.8 and 4.9 provide the OEB and its degradation, with respect to κ, when using all the studied cases and protocols at two different orientations. From Fig. 4.8, we can see that the OEB is at a minimum when $\kappa = 1$. Furthermore, the OEB for OWL case 3 worsens less sharply than in the other cases because κ approaches 0.9. It can also be noted that the smallest OEB is produced by the CLP protocol. However, the deterioration for both OWL case 1 and RLP is the same. Taking a closer look at the rate of change with respect to κ leads us to Fig. 4.9, where, in the case of no orientation, the OEB degradation

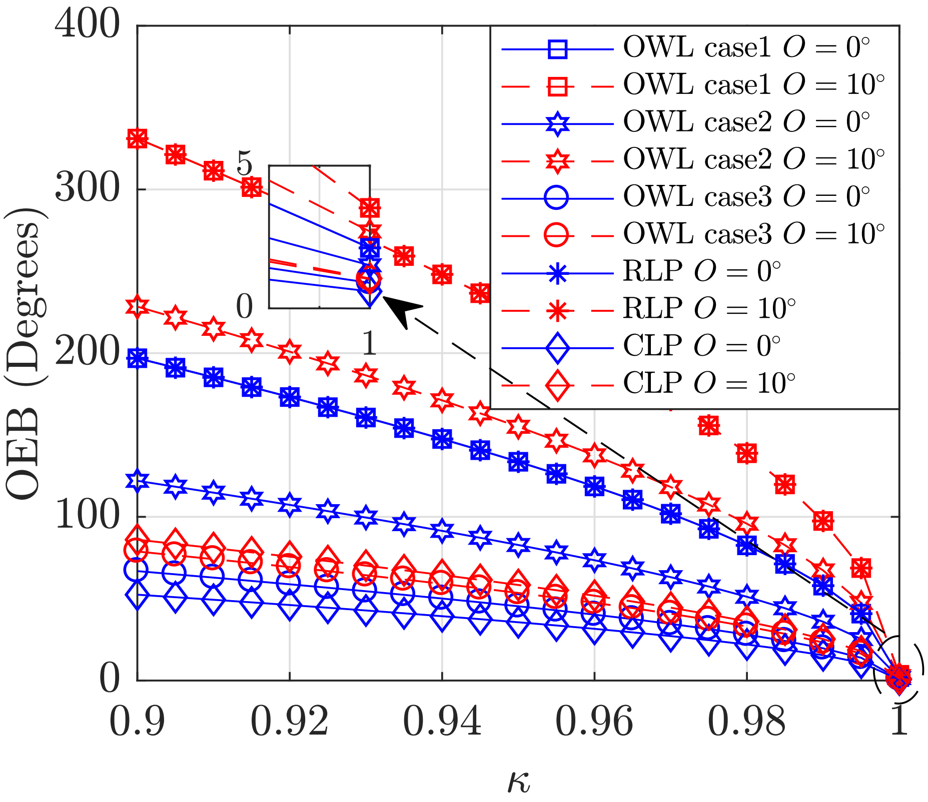

Figure 4.8: OEB w. r. t. κ considering two orientation angles $[0°; 0°]$ and $[10°; 10°]$ under the OWL, RLP and CLP.

exhibits the same behavior as that of PEB.

In the case of a tilted UE, using the CLP and OWL case 2, HWIs are more damaging to orientation estimation than to position estimation. The opposite effect is seen when using the RLP and OWL cases 1 and 3. For instance, in the comparison between two different orientations in the CLP, a $5.85 \times 100\%$ degradation difference in orientation estimation can be noticed when $\kappa = 0.9$, and this can be compared with a $3.33 \times 100\%$ degradation in position estimation. In general, by comparing figures 4.6 and 4.9, the OWL case 3 can be said to have the best resilience against HWIs while CLP maintains the best error bounds.

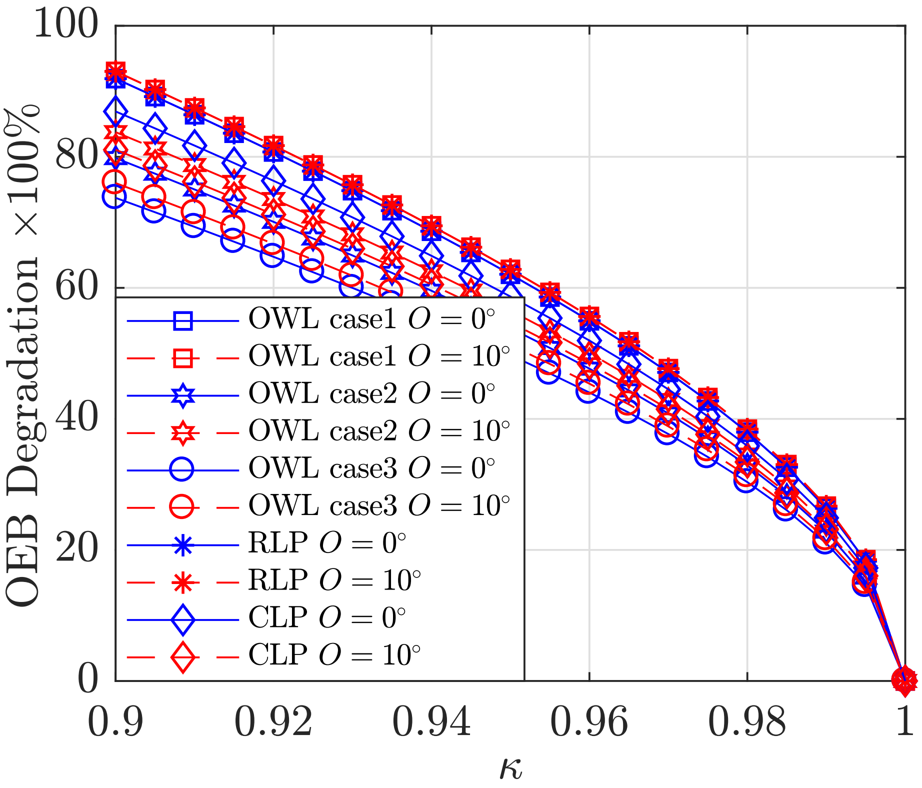

Figure 4.9: OEB degradation w. r. t. κ considering two orientation angles $[0°; 0°]$ and $[10°; 10°]$ under the OWL, RLP and CLP.

The reason for this is that CLP has only one anchor, which is close to the possible UE locations while two anchors are used in OWL-case 3, one of which is far from the UE location. As a result, more information is obtained using CLP than in OWL case 3 with two anchors spaced by distance d. The effect of this distance is investigated in Fig. 4.10.

Fig. 4.10 presents the PEB with respect to the distance between the two anchors in OWL case 3 at two different values for the HWIs factor: $\kappa = 1$ and $\kappa = 0.99$. In order to compare the change of PEB in both cases, the red line is inserted showing the PEB for the CLP with the corresponding HWIs values. As can be seen in the case of $\kappa = 1$ (Fig. 4.10a), when the second anchor is 40-47 m away from the first anchor, OWL case 3

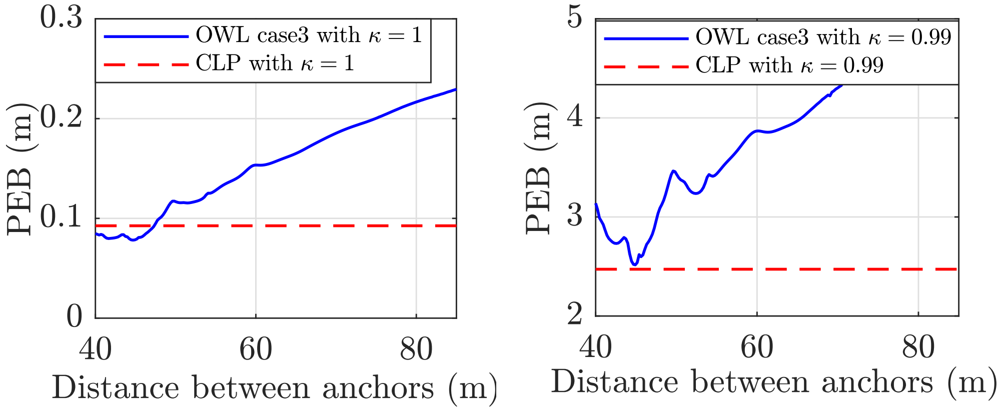

(a) κ=1, (b) κ=0.99,

Figure 4.10: PEB w. r. t. distance between two anchors considering no orientation under the OWL- case 3 and CLP with $\kappa = 1$ and $\kappa = 0.99$.

outperforms CLP. This occurs because the second anchor is much closer to the UE location (see Fig. 4.3). This applies to the OEB as well. In the case of $\kappa = 0.99$, due to the effects of HWI, there is no superiority of OWL case 3 over the CLP.

4.6 Conclusion

The effect of hardware impairments (HWIs) on localization with synchronous and asynchronous transceivers in 5G mmWave systems was studied in this chapter. We focus on one-way localization (OWL) under synchronized transceivers, as well as on two-anchor, two-way round-trip localization (RLP) and collaborative localization protocols (CLP) in order to eliminate the time bias between the asynchronized UE and BS. The position and orientation bounds for the UE were derived.

In line with the literature, our results demonstrate the superior performance of CLP over

RLP, not only in tackling disorientation but also under the stress of HWIs. On the other hand, almost no advantage is seen of the RLP over the OWL, except for the elimination of clock bias. Based on our investigation, error bounds for all cases are at a minimum at the ideal point and deteriorate by at least $70.93 \times 100\%$ as hardware imperfection worsens to 0.9. Position degradation is completely symmetrical for both the UE and BS's hardware imperfections.

Generally, the OWL with two anchors located at the center of two neighborhood cells has the best resilience against HWIs, while the CLP protocol demonstrates the best error bounds. Future works based on this chapter can include designing estimators to efficiently track the UE under the joint effects of HWIs and imperfect synchronization. There can also be an examination of the effect of Non-line of sight (NLOS) paths in the established scenario.

4.7 Publications Resulted from This Chapter

- F. Ghaseminajm, M. Alsmadi, S. S. Ikki, "Error Bounds for Localization in *mm*Wave MIMO Systems: Effects of Hardware Impairments Considering Perfect and Imperfect Clock Synchronization," to be published in *IEEE systems journal*.

Chapter 5

RIS-aided Mobile Localization Error Bounds Under Hardware Impairments (2D and 3D scenarios)

Overview: Reconfigurable intelligent surface (RIS) is the latest game-changing technology which helps improving the millileter wave (mmWave) communication systems' performance such as localization. The vulnerability of mmWave systems to the environment such as blockage can be mitigated using RIS by adjusting the incoming signals' phase. On the other hand, manufacturing an ideal hardware deployed at the transceivers is not feasible and practical. This non-linearity in hardware known as hardware impairments (HWIs), causes signal degradation and consequently more localization error. In this chapter, the effect of HWIs on RIS-assited localization for the both two dimension and three dimension scenarios is examined. Our numerical results show that active RISs alleviate the deteriorating effect of HWIs on the user's position error bounds (PEB). Based on our outcome, increasing the inter-RISs space by creating resolvable paths, leads to localization improvement.

5.1 Introduction

Based on Cisco annual internet report in March 2020, internet users will be increased by 15% in 2023 in comparison with the ones in 2018. Moreover, the global mobile devices is expected to be almost 5 billion more, from 2018 [2]. According to this growing connectivity, fifth generation (5G) wireless network has been deployed in some developed and developing countries; however, there is a need for a technology supporting all 5G application requirements, including escalated mobile broadband, ultra low latency communication and massive communication [69]. Plus, the complexity, cost and energy consumption of multiple-input multiple-output (MIMO) millimeter wave (mmWave) communication systems are pivotal concern [70]. For this reason, nowadays, researchers are more focused on a brand-new technology with low cost and energy consumption solution: reconfigurable intelligent surfaces (RISs).

RISs consist of a large number of passive elements in which they are capable of controlling the phase of incoming signals independently [70, 96]. Furthermore, the receiver noise do not affect the RIS, so the analog to digital (ADC) and the digital to analog (DAC) converters are not needed [69]. This intelligent reflecting and low cost surface can boost the wireless communication performance, such as positioning. Localization is one of the main features of 5G mmWave communication systems. In this chapter, large number of elements in RISs along with multiple paths (e.g. line of sight (LOS) and the reflected paths from the RIS) make the estimation of angle of departure (AoD), angle of arrival (AoA) and time of arrival (ToA) achievable [15, 77]. For example, [97] as well as [98] and [99], using combination of AoD, AoA and ToA found the Cramér-Rao lower bounds (CRLB) and consequently, the position (PEB) and orientation error bounds (OEB) of a user equipment (UE).

On the other hand, often localization is affected by the hardware impairments (HWIs) at the transceivers. Ideally, baseband samples at the transmitter generate the accurate passband signals; then, at the receiver side, the signal is demodulated, reliably [65]. However, this is not accomplishable and manufacturing of transceivers often comes with some minor deficiency and non-linearity, known as *HWIs*. This deficiency is presented in two forms: additive and multiplicative [86]. It is shown in [100] that HWIs cause major degradation in UE's localization. In this chapter, we examine the effect of this imperfection on the RIS aided single-input single-output (SISO) communication system to see how RIS compensates the degradation originated from HWIs. Although, [86] studied the effect of HWIs on RIS assisted wireless communication, its effect on the UE's localization has not been studied yet.

Even more, [101] proved that RIS has significant effect on localization under asynchronous condition. Moreover, [102] noted that RIS makes joint localization and synchronization possible using only downlink multiple-input single-output (MISO) transmission. In addition, near-field positioning is done using a proper RIS phase design and another two algorithms by [103] and [104], respectively. [105] performed multi targets' localization and [106] optimized RISs' phase shifters using hierarchical code book (HCB) algorithm. Moreover, [107] proposed a novel method in a RIS-aided communication system in which using the sparse nature of mmWave communication system, UE is estimated. RIS is profitable for Indoor localization as well, in which the blockage can be compensated; [108] combined RIS and ultra wide band (UWB) signals for this purpose.

To the best of our knowledge, the effect of HWIs on RIS-aided localization has not been studied yet. In this chapter, we present a scenario in which RIS is assisting the localization process affected by HWIs. Focusing on the uplink transmission and considering the both LOS and non-line of sight (NLOS) paths (reflected from the RISs) in two dimension (2D) and 3D scenarios, our main contribution is to examine the following concerns

- How much the localization can benefit from the RISs in order to overcoming the degradation caused by HWIs?
- How much increasing the number of passive elements in each RIS and increasing the number of RISs can help reducing the localization bounds?
- Does increasing the inter-RIS space help improving the positioning performance?

The rest of the chapter is organized as follows. Section 5.2, provides the signal and channel model affected by HWIs in 2D and 3D scenarios. The Fisher information matrix (FIM) of the unknown parameters and channel parameters is earned in section 5.3, followed by the transformation to the location parameters' FIM. Also, in order to optimizing the RISs' control matrix, the RIS resource allocation is presented in the subsection 5.3.3. Section 5.4 provides the simulation setup and the numerical results for both 2D and 3D scenarios. Finally, section 5.5 concludes the chapter.

5.2 Problem formulation

First, we assume a 2D scenario, shown in Fig. 5.1, including a single antenna base station (BS) and UE. Considering uplink transmission, we establish a line of G- RISs. Each RIS is located at location (x_{g}, L) and equipped with M-element uniform linear array (ULA) on the x-axis, spacing $\frac{\lambda}{2}$. On the other hand, we assume a 3D scenario as shown in Fig. 5.2 and considering uplink transmission, it is consisting of a BS and UE with a single antenna.

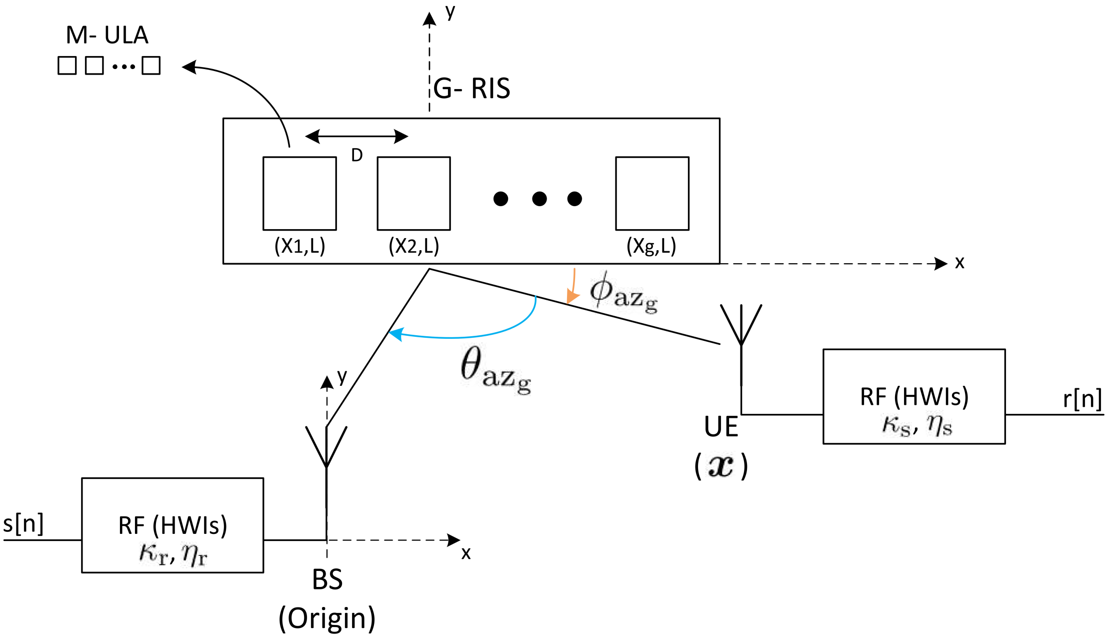

Figure 5.1: RIS-aided localization 2D scenario consisting of UE as a transmitter and BS as a receiver and a line of G RISs.

This time, we consider a wall consisting of series of G-RISs, each with M-element uniform rectangular array (URA) on xy-plane; in which $M = M_{\mathrm{x}} M_{\mathrm{y}}$ with M_{x} and M_{y} elements located on the x and y axis, respectively and spacing $\frac{\lambda}{2}$. The inter-RIS spacing for the both 2D and 3D scenarios is D. We assume BS and UE are affected by HWIs with factor κ_{s} and κ_{r} in the transmitter and receiver, respectively. In the 3D scenario, the wall is located at the cell's edge; in which each RIS is placed at $\boldsymbol{x}_{\mathrm{g}}$. Also, the BS and UE are located at origin and $\boldsymbol{x}$, respectively.

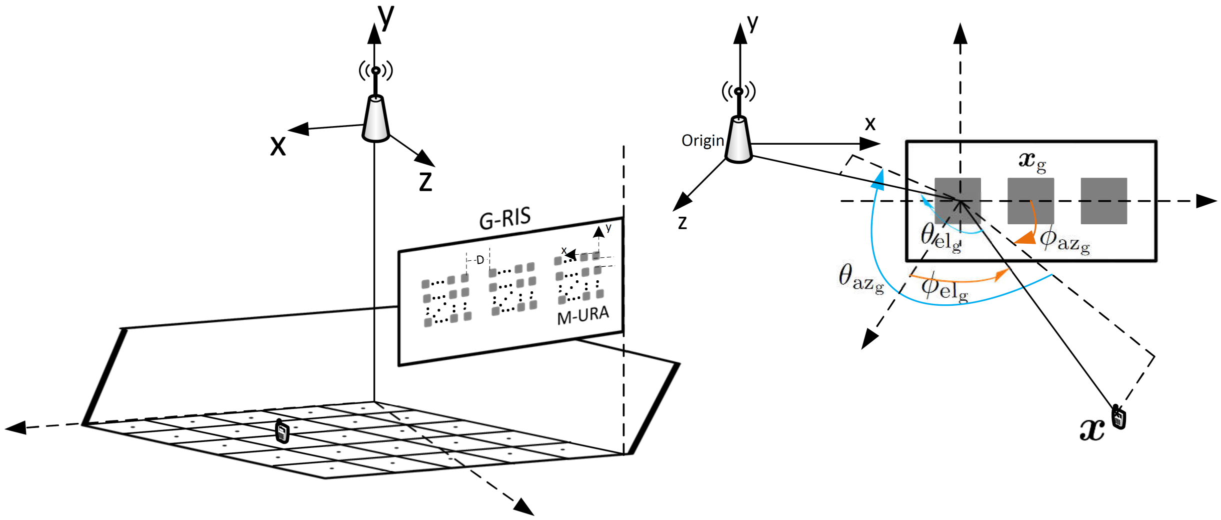

Figure 5.2: RIS-aided localization 3D scenario consisting of UE as a transmitter and BS as a receiver and a wall of G RISs.

5.2.1 Signal and channel model

Taking mm-Wave communication into account, the UE transmits signal $f(t)$ as below

$$f(t) = \sqrt{\kappa_{\mathrm{s}}}s(t) + \eta_{\mathrm{s}}, \tag{5.1}$$

in which κ_{s} is the HWIs factor at the transmitter (UE) antenna, η_{s} is the source additive distortion noise with mean zero and variance $\sigma^2_{\eta_{\mathrm{s}}} = E(1-\kappa_{\mathrm{s}})$; where E is the power of the transmitted signal $s(t)$. The received signal at the BS consisting of LOS and reflected signals from RISs, can be written as

$$r(t) = \sum_{g=0}^{G} \sqrt{\kappa_{\mathrm{r}}}\beta_{\mathrm{g}} \boldsymbol{h}_{\mathbf{g}}{}^{\mathrm{T}} \boldsymbol{\Omega}_{\mathrm{g}} \boldsymbol{g}_{\mathbf{g}} f(t-\tau_{\mathrm{g}}) + \eta_{\mathrm{r}} + n(t), \tag{5.2}$$

where $f(t)$ is the signal affected by HWIs, η_{r} is the responder's (BS) additive distortion noise with mean zero and variance $\sigma^2_{\eta_{\mathrm{r}}} = E(1-\kappa_{\mathrm{r}})\sum_{g=0}^{G}|\beta_{\mathrm{g}}|^2$, $n(t)$ is the proper white Gaussian noise with power spectral density (PSD) N_0. Also, κ_{r} is the BS's HWIs factor. β_{g} for the LOS path and the reflected paths can be driven as below

$$\beta_{\mathrm{g}} = \begin{cases} e^{-j2\pi f_{\mathrm{c}}\tau_0}\dfrac{\lambda}{4\pi\|\boldsymbol{x}\|}, & g=0 \\ e^{-j2\pi f_{\mathrm{c}}\tau_{\mathrm{g}}}\dfrac{\Gamma\lambda}{4\pi\left(\|\boldsymbol{x}_{\mathrm{g}}\|+\|\boldsymbol{x}-\boldsymbol{x}_{\mathrm{g}}\|\right)}, & g\neq 0 \end{cases} \tag{5.3}$$

where $\boldsymbol{x}$ and $\boldsymbol{x}_{\mathrm{g}}$ represent UE and g^{th} RIS locations. Moreover, f_{c} is the carrier frequency. $\tau_0 = \|\boldsymbol{x}\|/c$ is the LOS path delay while $\tau_{\mathrm{g}} = \|\boldsymbol{x}_{\mathrm{g}}\|/c + \|\boldsymbol{x}_{\mathrm{g}} - \boldsymbol{x}\|/c$ are the reflected path delays and c is the propagation speed. Also, $\lambda = c/f_{\mathrm{c}}$ is the signal wavelength. Plus, Γ is the reflection coefficient in case of inactivity of the corresponding RIS.

Furthermore, $\boldsymbol{h}_{\mathrm{g}}$ and $\boldsymbol{g}_{\mathrm{g}}$ in (5.2) are calculated only for the reflected paths and where as [109] and [98], for the uplink transmission are the $M \times 1$ UE-to-RIS and RIS-to-BS response vector, respectively. For the 2D scenario,

$$\boldsymbol{h}_{\mathrm{g},m} = \frac{1}{\sqrt{M}}\exp\left(-j\boldsymbol{\Delta}^{\mathrm{T}}\boldsymbol{k}(\phi_{\mathrm{az_g}})\right), \tag{5.4}$$

$$\boldsymbol{g}_{\mathrm{g},m} = \frac{1}{\sqrt{M}}\exp\left(-j\boldsymbol{\Delta}^{\mathrm{T}}\boldsymbol{k}(\theta_{\mathrm{az_g}})\right), \tag{5.5}$$

and for the 3D scenario,

$$\boldsymbol{h}_{\mathrm{g},m} = \frac{1}{\sqrt{M}}\exp\left(-j\boldsymbol{\Delta}^{\mathrm{T}}\boldsymbol{k}(\phi_{\mathrm{az_g}},\phi_{\mathrm{el_g}})\right), \tag{5.6}$$

$$\boldsymbol{g}_{\mathrm{g},m} = \frac{1}{\sqrt{M}}\exp\left(-j\boldsymbol{\Delta}^{\mathrm{T}}\boldsymbol{k}(\theta_{\mathrm{az_g}},\theta_{\mathrm{el_g}})\right), \tag{5.7}$$

where, $m \in \{0,\cdots,M-1\}$, $\boldsymbol{k}(\phi_{\mathrm{az_g}})$ and $\boldsymbol{k}(\phi_{\mathrm{az_g}},\phi_{\mathrm{el_g}})$ is the wave number vector in the azimuth direction $\phi_{\mathrm{az_g}}$ for 2D and in azimuth direction $\phi_{\mathrm{az_g}}$ and elevation direction $\theta_{\mathrm{az_g}}$ for the 3D scenario, respectively and for the 2D can be calculated as,

$$\boldsymbol{k}(\phi_{\mathrm{az_g}}) = \frac{2\pi}{\lambda}[\cos(\phi_{\mathrm{az_g}}); \sin(\phi_{\mathrm{az_g}}); 0],$$

while for the 3D, it is earned by,

$$\boldsymbol{k}(\phi_{\mathrm{az_g}}, \phi_{\mathrm{el_g}}) = \frac{2\pi}{\lambda}[\cos(\phi_{\mathrm{az_g}})\sin(\phi_{\mathrm{el_g}}); \sin(\phi_{\mathrm{az_g}})\sin(\phi_{\mathrm{el_g}}); \cos(\phi_{\mathrm{el_g}})],$$

Moreover, $\boldsymbol{\Delta}$ is the antenna location matrix and in our scenario, assuming starting point (x_0, L) in the 2D scenario, for the m^{th} element of the g^{th} RIS, can be written as below,

$$\boldsymbol{\Delta}(m, g) = [(m-1)\frac{\lambda}{2} + (g-1)D + x_0; L], \tag{5.8}$$

where, $\boldsymbol{\Delta}(m, g) \in \mathbb{R}^{2\times M},\ g > 1,\ m \in \{1, ..., M\}$. Also, in 3D, assuming starting point $(0; y_0; z_0)$ for the $(m_{\mathrm{x}}, m_{\mathrm{y}})^{th}$ element of the g^{th} RIS, $\boldsymbol{\Delta}$ can be calculated as

$$\boldsymbol{\Delta}(m_{\mathrm{x}}, m_{\mathrm{y}}, g) = [(m_{\mathrm{x}}-1)\frac{\lambda}{2} + (g-1)D; y_0 + (m_{\mathrm{y}}-1)\frac{\lambda}{2}; z_0], \tag{5.9}$$

where, $\boldsymbol{\Delta}(m_{\mathrm{x}}, m_{\mathrm{y}}, g) \in \mathbb{R}^{3\times M},\ g > 1,\ m_{\mathrm{x}} \in \{1, ..., M_{\mathrm{x}}\}\ \mathit{and}\quad m_{\mathrm{y}} \in \{1, ..., M_{\mathrm{y}}\}$. Considering $\boldsymbol{s}_{\mathrm{g}} = \boldsymbol{x} - \boldsymbol{x}_{\mathrm{g}}$, $\phi_{\mathrm{az_g}} = \tan^{-1}(\frac{\boldsymbol{s}_{\mathrm{g}}(2)}{\boldsymbol{s}_{\mathrm{g}}(1)})$ and $\phi_{\mathrm{el_g}} = \cos^{-1}(\frac{\boldsymbol{s}_{\mathrm{g}}(3)}{\|\boldsymbol{s}_{\mathrm{g}}\|})$ are the azimuth and elevation AoA of the received signal in g^{th} RIS from UE and $\theta_{\mathrm{az_g}}$ and $\theta_{\mathrm{el_g}}$ are the azimuth and elevation AoD of the transmitted signal from the g^{th} RIS to the BS. Note that, $\phi_{\mathrm{el_g}}$ and $\theta_{\mathrm{el_g}}$ are not applicable in the 2D scenario.

It worth mentioning that we assume all the paths are resolvable; this can be reached by choosing RIS distance greater than $\frac{c}{W}$, so the paths can arrive in different timing [97];

where, W is the signal bandwidth.

For the best UE localization performance, we need to optimize diagonal $M \times M$ controlling matrix $\boldsymbol{\Omega}_{\mathrm{g}}$; in other words, matrix $\boldsymbol{\Omega}_{\mathrm{g}}$ will control the phase of departed signal from RIS. Note that, ${\boldsymbol{h}_{\mathbf{g}}}^{\mathrm{T}}\boldsymbol{\Omega}_{\mathrm{g}}\boldsymbol{g}_{\mathbf{g}} = 1$, when $g = 0$ in the LOS path. The optimization procedure will be explained in detail in subsection 5.3.3.

By substituting (5.1) into (5.2), we have

$$r(t) = \kappa \sum_{g=0}^{G} \beta_{\mathrm{g}} {\boldsymbol{h}_{\mathbf{g}}}^{\mathrm{T}} \boldsymbol{\Omega}_{\mathrm{g}} \boldsymbol{g}_{\mathbf{g}} s(t - \tau_{\mathrm{g}}) + \sqrt{\kappa_{\mathrm{r}}} \sum_{g=0}^{G} \beta_{\mathrm{g}} {\boldsymbol{h}_{\mathbf{g}}}^{\mathrm{T}} \boldsymbol{\Omega}_{\mathrm{g}} \boldsymbol{g}_{\mathbf{g}} \eta_{\mathrm{s}} + \eta_{\mathrm{r}} + n(t), \tag{5.10}$$

in which $\kappa = \sqrt{\kappa_{\mathrm{s}}\kappa_{\mathrm{r}}}$. In order to deriving the error bounds, the variance of the received noise needs to be calculated. Towards that, first, we separate the signal and noise parts of the received signal in (5.10), as $\mu(t)$ and $w(t)$, respectively.

$$\mu(t) = \kappa \sum_{g=0}^{G} \beta_{\mathrm{g}} {\boldsymbol{h}_{\mathbf{g}}}^{\mathrm{T}} \boldsymbol{\Omega}_{\mathrm{g}} \boldsymbol{g}_{\mathbf{g}} s(t - \tau_{\mathrm{g}}), \tag{5.11}$$

$$w(t) = \sqrt{\kappa_{\mathrm{r}}} \sum_{g=0}^{G} \beta_{\mathrm{g}} {\boldsymbol{h}_{\mathbf{g}}}^{\mathrm{T}} \boldsymbol{\Omega}_{\mathrm{g}} \boldsymbol{g}_{\mathbf{g}} \eta_{\mathrm{s}} + \eta_{\mathrm{r}} + n(t), \tag{5.12}$$

according to (5.12) and based on the calculated variance of distortion noises, the received noise variance, σ_{w}^2, can be written as

$$\sigma_{\mathrm{w}}^2 = E(1 - \kappa^2) \sum_{g=0}^{G} |\beta_{\mathrm{g}}|^2 + N_0. \tag{5.13}$$

After signal acquisition and conversion of the signal part, in (5.11), to the frequency domain by discrete Fourier transform (DFT), the observation at the n-th point becomes

$$\mu[n] = \kappa \sum_{g=0}^{G} \beta_{\mathrm{g}} \boldsymbol{h}_{\mathbf{g}}{}^{\mathrm{T}} \boldsymbol{\Omega}_{\mathrm{g}} \boldsymbol{g}_{\mathbf{g}} e^{-j\tau_{\mathrm{g}} F[n]} s[n], \tag{5.14}$$

in which $F[n] = \frac{2\pi n W}{N+1}$, where N is the total number of the points.

5.3 Localization problem

Our goal is to obtain the UE PEB using the received signal $r(t)$ with optimized diagonal matrix $\boldsymbol{\Omega}_{\mathrm{g}}$. To achieve this, we need to accomplish three steps: first, we derive Fisher information of unknown parameters $\boldsymbol{\varphi} \triangleq \{\boldsymbol{\tau}, \boldsymbol{\phi_{az}}, \boldsymbol{\beta_R}, \boldsymbol{\beta_I}, \kappa\}$ for 2D and $\boldsymbol{\varphi} \triangleq \{\boldsymbol{\tau}, \boldsymbol{\phi_{az}}, \boldsymbol{\phi_{el}}, \boldsymbol{\beta_R}, \boldsymbol{\beta_I}, \kappa\}$ for the 3D scenario. Then, we calculate the EFIM for the channel parameters $\boldsymbol{\varphi}_{\mathrm{CH}} \triangleq \{\boldsymbol{\tau}, \boldsymbol{\phi_{az}}\}$ for 2D and $\boldsymbol{\varphi}_{\mathrm{CH}} \triangleq \{\boldsymbol{\tau}, \boldsymbol{\phi_{az}}, \boldsymbol{\phi_{el}}\}$ for the 3D scenario. Finally, we transform the channel parameters $\boldsymbol{\varphi}_{\mathrm{CH}}$ to the location parameters $\boldsymbol{\varphi}_{\mathrm{L}} \triangleq \{\boldsymbol{x}\}$.

5.3.1 Fisher Information Analysis

We now derive the Fisher Information Matrix (FIM) of the vector $\boldsymbol{\varphi}$, containing $4G + 4$ and $5G + 4$ unknown parameters for the 2D and 3D scenarios, respectively. Namely, define

$$\boldsymbol{\varphi} \triangleq [\boldsymbol{\tau}, \boldsymbol{\phi_{az}}, \boldsymbol{\beta_R}, \boldsymbol{\beta_I}, \kappa] \ \textit{in 2D}, \tag{5.15}$$

$$\boldsymbol{\varphi} \triangleq [\boldsymbol{\tau}, \boldsymbol{\phi_{az}}, \boldsymbol{\phi_{el}}, \boldsymbol{\beta_R}, \boldsymbol{\beta_I}, \kappa] \ \textit{in 3D}, \tag{5.16}$$

where,

$$\begin{aligned}\boldsymbol{\tau} &\triangleq [\tau_0, \tau_1, ..., \tau_{\mathrm{G}}]\,,\\ \boldsymbol{\phi_{az}} &\triangleq [\phi_{\mathrm{az}_1}, ..., \phi_{\mathrm{az}_{\mathrm{G}}}]\,,\\ \boldsymbol{\phi_{el}} &\triangleq [\phi_{\mathrm{el}_1}, ..., \phi_{\mathrm{el}_{\mathrm{G}}}]\,,\\ \boldsymbol{\beta_R} &\triangleq [\beta_{\mathrm{R}_0}, \beta_{\mathrm{R}_1}, ..., \beta_{\mathrm{R}_{\mathrm{G}}}]\,,\\ \boldsymbol{\beta_I} &\triangleq [\beta_{\mathrm{I}_0}, \beta_{\mathrm{I}_1}, ..., \beta_{\mathrm{I}_{\mathrm{G}}}]\,,\end{aligned}$$

Also, $\beta_{\mathrm{R}_{\mathrm{g}}}$ and $\beta_{\mathrm{I}_{\mathrm{g}}}$ are the real and imaginary parts of the g^{th} path channel gain β_{g}. Then, the corresponding FIM is denoted by

$$\boldsymbol{J_{\varphi}} = \begin{bmatrix} \boldsymbol{J_{\varphi_{\mathbf{CH}}}} & \boldsymbol{J_{\varphi_{\mathbf{CN}}}} \\ \boldsymbol{J_{\varphi_{\mathbf{CN}}}}^{\mathrm{T}} & \boldsymbol{J_{\varphi_{\mathbf{N}}}} \end{bmatrix} \in \mathbb{R}^{(4G+4)\times(4G+4)}\text{for 2D and} \in \mathbb{R}^{(5G+4)\times(5G+4)}\text{for 3D,} \tag{5.17}$$

in which $\boldsymbol{J_{\varphi_{\mathbf{CH}}}}$ and $\boldsymbol{J_{\varphi_{\mathbf{N}}}}$ are the channel and nuisance parameters' FIM, respectively and $\boldsymbol{J_{\varphi_{\mathbf{CN}}}}$ is the mutual information of the channel and nuisance parameters. The matrices in (5.17), can be written for the 2D scenario as follows.

$$\boldsymbol{J_{\varphi_{\mathbf{CH}}}} = \begin{bmatrix} \boldsymbol{J_{\tau\tau}} & \boldsymbol{J_{\tau\phi_{az}}} \\ \boldsymbol{J_{\phi_{az}\tau}} & \boldsymbol{J_{\phi_{az}\phi_{az}}} \end{bmatrix} \in \mathbb{R}^{(2G+1)\times(2G+1)}, \tag{5.18}$$

$$\boldsymbol{J_{\varphi_{\mathbf{CN}}}} = \begin{bmatrix} \boldsymbol{J_{\tau\beta_R}} & \boldsymbol{J_{\tau\beta_I}} & \boldsymbol{j_{\tau\kappa}} \\ \boldsymbol{J_{\phi_{az}\beta_R}} & \boldsymbol{J_{\phi_{az}\beta_I}} & \boldsymbol{j_{\phi_{az}\kappa}} \end{bmatrix} \in \mathbb{R}^{(2G+1)\times(2G+3)}, \tag{5.19}$$

and for the 3D scenario,

$$\boldsymbol{J}_{\boldsymbol{\varphi}_{\mathbf{CH}}} = \begin{bmatrix} \boldsymbol{J}_{\boldsymbol{\tau\tau}} & \boldsymbol{J}_{\boldsymbol{\tau\phi_{az}}} & \boldsymbol{J}_{\boldsymbol{\tau\phi_{el}}} \\ \boldsymbol{J}_{\boldsymbol{\phi_{az}\tau}} & \boldsymbol{J}_{\boldsymbol{\phi_{az}\phi_{az}}} & \boldsymbol{J}_{\boldsymbol{\phi_{az}\phi_{el}}} \\ \boldsymbol{J}_{\boldsymbol{\phi_{el}\tau}} & \boldsymbol{J}_{\boldsymbol{\phi_{el}\phi_{el}}} & \boldsymbol{J}_{\boldsymbol{\phi_{el}\phi_{el}}} \end{bmatrix} \in \mathbb{R}^{(3G+1)\times(3G+1)}, \tag{5.20}$$

$$\boldsymbol{J}_{\boldsymbol{\varphi}_{\mathbf{CN}}} = \begin{bmatrix} \boldsymbol{J}_{\boldsymbol{\tau\beta_R}} & \boldsymbol{J}_{\boldsymbol{\tau\beta_I}} & \boldsymbol{j}_{\boldsymbol{\tau}\kappa} \\ \boldsymbol{J}_{\boldsymbol{\phi_{az}\beta_R}} & \boldsymbol{J}_{\boldsymbol{\phi_{az}\beta_I}} & \boldsymbol{j}_{\boldsymbol{\phi_{az}}\kappa} \\ \boldsymbol{J}_{\boldsymbol{\phi_{el}\beta_R}} & \boldsymbol{J}_{\boldsymbol{\phi_{el}\beta_I}} & \boldsymbol{j}_{\boldsymbol{\phi_{el}}\kappa} \end{bmatrix} \in \mathbb{R}^{(3G+1)\times(2G+3)}, \tag{5.21}$$

and for the both 2D and 3D scenarios,

$$\boldsymbol{J}_{\boldsymbol{\varphi}_{\mathbf{N}}} = \begin{bmatrix} \boldsymbol{J}_{\boldsymbol{\beta_R\beta_R}} & \boldsymbol{J}_{\boldsymbol{\beta_R\beta_I}} & \boldsymbol{j}_{\boldsymbol{\beta_R}\kappa} \\ \boldsymbol{J}_{\boldsymbol{\beta_I\beta_R}} & \boldsymbol{J}_{\boldsymbol{\beta_I\beta_I}} & \boldsymbol{j}_{\boldsymbol{\beta_I}\kappa} \\ \boldsymbol{j}_{\kappa\boldsymbol{\beta_R}} & \boldsymbol{j}_{\kappa\boldsymbol{\beta_I}} & J_{\kappa\kappa} \end{bmatrix} \in \mathbb{R}^{(2G+3)\times(2G+3)}, \tag{5.22}$$

Note that

$$\boldsymbol{J}_{\boldsymbol{\varphi_i\varphi_j}} \in \mathbb{R}^{(\textit{number of elements in } \varphi_i)\times(\textit{number of elements in } \varphi_j)}.$$

In general, each scalar FIM element in (5.17) can be defined as [110]

$$\boldsymbol{J}_{\varphi_\mathrm{i}\varphi_\mathrm{j}} = \sum_{n=-N/2}^{N/2} \Re\Big\{\mathrm{tr}\left[(\sigma_\mathrm{w}^2)^{-1}\left(\frac{\partial\sigma_\mathrm{w}^2}{\partial\varphi_\mathrm{i}}\right)(\sigma_\mathrm{w}^2)^{-1}\left(\frac{\partial\sigma_\mathrm{w}^2}{\partial\varphi_\mathrm{j}}\right)\right] + 2\left[\frac{\partial\boldsymbol{\mu}}{\partial\varphi_\mathrm{i}}\right]^\mathrm{H}(\sigma_\mathrm{w}^2)^{-1}\left[\frac{\partial\boldsymbol{\mu}}{\partial\varphi_\mathrm{j}}\right]\Big\}, \tag{5.23}$$

The full derivation of the elements of (5.17) is provided in appendix C.1.

The FIM $\boldsymbol{J}_{\boldsymbol{\varphi}_{\mathbf{CH}}}$ contains important information about the UE's location. In order to eliminate the effect of nuisance parameters $\boldsymbol{\varphi_N}$ from the channel parameters $\boldsymbol{\varphi_{CH}}$, schure complement can be used as below [90],

$$\boldsymbol{J}^{\mathrm{e}}_{\boldsymbol{\varphi}_{\mathbf{CH}}} = \boldsymbol{J}_{\boldsymbol{\varphi}_{\mathbf{CH}}} - \boldsymbol{J}_{\boldsymbol{\varphi}_{\mathbf{CN}}} \boldsymbol{J}^{-1}_{\boldsymbol{\varphi}_{\mathbf{N}}} \boldsymbol{J}^{\mathrm{T}}_{\boldsymbol{\varphi}_{\mathbf{CN}}} \in \mathbb{R}^{(2G+1)\times(2G+1)} \text{for 2D and} \in \mathbb{R}^{(3G+1)\times(3G+1)} \text{for 3D}, \tag{5.24}$$

where $\boldsymbol{J}^{\mathrm{e}}_{\boldsymbol{\varphi}_{\mathbf{CH}}}$ is the equivalent FIM (EFIM) of the channel parameters.

5.3.2 FIM of the location parameters

With a focus on presenting the position error bound, the derived EFIM in (5.24) needs to be transferred to the location parameter $\boldsymbol{\varphi}_{\boldsymbol{L}} \triangleq [\boldsymbol{x}]$. Towards that, the transformation matrix $\boldsymbol{\gamma}$ is defined for the 2D scenario as below

$$\gamma \triangleq \frac{\partial \boldsymbol{\varphi}_{\boldsymbol{CH}}}{\partial \boldsymbol{\varphi}_{\boldsymbol{L}}} = \begin{bmatrix} \frac{\partial \boldsymbol{\tau}}{\partial \boldsymbol{x}} & \frac{\partial \boldsymbol{\phi}_{\boldsymbol{az}}}{\partial \boldsymbol{x}} \end{bmatrix} \in \mathbb{R}^{2\times(2G+1)}, \tag{5.25}$$

and for the 3D scenario,

$$\gamma \triangleq \frac{\partial \boldsymbol{\varphi}_{\boldsymbol{CH}}}{\partial \boldsymbol{\varphi}_{\boldsymbol{L}}} = \begin{bmatrix} \frac{\partial \boldsymbol{\tau}}{\partial \boldsymbol{x}} & \frac{\partial \boldsymbol{\phi}_{\boldsymbol{az}}}{\partial \boldsymbol{x}} & \frac{\partial \boldsymbol{\phi}_{\boldsymbol{el}}}{\partial \boldsymbol{x}} \end{bmatrix} \in \mathbb{R}^{3\times(3G+1)}, \tag{5.26}$$

Full derivation of the transfom matrix $\boldsymbol{\gamma}$ is provided in appendix C.2. Thus, the EFIM of the location parameter, $\boldsymbol{J}^{\mathrm{e}}_{\boldsymbol{\varphi}_{\mathbf{L}}}$, can be computed as,

$$\boldsymbol{J}^{\mathrm{e}}_{\boldsymbol{\varphi}_{\mathbf{L}}} = \boldsymbol{\gamma} \boldsymbol{J}^{\mathrm{e}}_{\boldsymbol{\varphi}_{\mathbf{CH}}} \boldsymbol{\gamma}^{\mathrm{T}}, \in \mathbb{R}^{2\times 2} \text{for 2D and} \in \mathbb{R}^{3\times 3} \text{for 3D} \tag{5.27}$$

the diagonal elements of inverse matrix of $\boldsymbol{J}^{\mathrm{e}}_{\boldsymbol{\varphi}_{\mathbf{L}}}$ contains the position error bounds. Finally, the PEB for 2D and 3D scenario is derived as,

$$\mathrm{PEB} = \sqrt{[\mathbf{C}]_{1,1} + [\mathbf{C}]_{2,2}}, \tag{5.28}$$

and

$$\mathrm{PEB} = \sqrt{[\mathbf{C}]_{1,1} + [\mathbf{C}]_{2,2} + [\mathbf{C}]_{3,3}}, \tag{5.29}$$

respectively. where $\mathbf{C} = {\boldsymbol{J}^{\mathrm{e}}_{\boldsymbol{\varphi}_{\mathbf{L}}}}^{\mathbf{-1}}$.

5.3.3 RIS Resource Allocation

Similar to [97], we consider two variables allocating the RIS resources. Vector $\boldsymbol{a} = [\mathrm{a}_1, \mathrm{a}_2, ..., \mathrm{a}_{\mathrm{g}}]$ and controller matrix $\boldsymbol{\Omega}_{\mathrm{g}} = \mathrm{diag}\left(e^{j\omega_{\mathrm{g},0}}, ..., e^{j\omega_{\mathrm{g},M-1}}\right)$ where $\boldsymbol{\omega}_{\mathrm{g}} = [\omega_1^{\mathrm{T}}, ..., \omega_{\mathrm{G}}^{\mathrm{T}}]^{\mathrm{T}}$. The first variable (i.e. $\boldsymbol{a}$) represents the inactive RIS as $\mathrm{a}_{\mathrm{g}} = 0$ and active RIS as $\mathrm{a}_{\mathrm{g}} = 1$. For the inactive case, RIS will act as an omnidirectional reflector, so that $\Omega_{\mathrm{g}} = \boldsymbol{I}_{\mathrm{M}}$).

On the other hand if the RIS is active, Ω_{g} needs to be optimized in order to minimize the error bounds. Achieving maximum signal to noise ratio (SNR) minimizes the PEB. Based on the signal model in (5.14) and the received noise variance in (5.13), the SNR is calculated as below

$$\mathrm{SNR} = \frac{\kappa^2}{1 - \kappa^2 + \frac{N0}{E\sum_{g=0}^{G} |\beta_{\mathrm{g}}|^2 |\boldsymbol{h}_{\mathrm{g}}^{\mathrm{T}} \boldsymbol{\Omega}_{\mathrm{g}} \boldsymbol{g}_{\mathrm{g}}|^2}}, \tag{5.30}$$

which is maximized if the term $|\boldsymbol{h}_{\mathrm{g}}^{\mathrm{T}}\boldsymbol{\Omega}_{\mathrm{g}}\boldsymbol{g}_{\mathrm{g}}|^2$ is maximized [97]. So that,

$$|\boldsymbol{h}_{\mathrm{g}}^{\mathrm{T}}\boldsymbol{\Omega}_{\mathrm{g}}\boldsymbol{g}_{\mathrm{g}}|^2 = \left|\sum_{m=0}^{M-1} e^{j\omega_{\mathrm{g,m}}} e^{-j\boldsymbol{\Delta}^{\mathrm{T}}\boldsymbol{k}(\phi_{\mathrm{g-az}},\phi_{\mathrm{g-el}})} e^{-j\boldsymbol{\Delta}^{\mathrm{T}}\boldsymbol{k}(\theta_{\mathrm{g-az}},\theta_{\mathrm{g-el}})}\right|^2, \tag{5.31}$$

then,

$$\begin{aligned} \omega_{\mathrm{g,m}} &= \boldsymbol{\Delta}^{\mathrm{T}}\left(\boldsymbol{k}(\phi_{\mathrm{g-az}}) + \boldsymbol{k}(\theta_{\mathrm{g-az}})\right) \text{For 2D,} \\ \omega_{\mathrm{g,m}} &= \boldsymbol{\Delta}^{\mathrm{T}}\left(\boldsymbol{k}(\phi_{\mathrm{g-az}},\phi_{\mathrm{g-el}}) + \boldsymbol{k}(\theta_{\mathrm{g-az}},\theta_{\mathrm{g-el}})\right) \text{For 3D.} \end{aligned} \tag{5.32}$$

5.4 Discussions and Numerical results

5.4.1 Simulation setup

In this simulation, we consider uplink transmission, in which, the receiver (BS) is located at the origin, 10 m above the transmitter (UE), in 3D scenario. The UE is assumed to be located at anywhere in a 10 m × 10 m square in 2D scenario and in one sector of a 50 m radius cell, in the xz- plane, in 3D scenario. Both the UE and BS are equipped with a single antenna and operating at frequency $f = 38\ GHz$. In order to assist the UE localization, 3 RISs, each equipped with 100 elements, are located on the line $\boldsymbol{x}_{\mathrm{g}}(3) = 10m$ on one edge of the square (2D) and on edge of the cell (3D) in the plane $\boldsymbol{x}_{\mathrm{g}}(3) = 25\sqrt{3}m$. In 3D scenario, the elements of the RIS are forming a 10 × 10 URA. Similar to [83], we pass the transmitted signal through a unit energy ideal *sinc* pulse shape filter; so that, the signal has the bandwidth $W = 125\ MHz$. Also, in order to the frequency conversion through DFT, we chose 129 points. Moreover, the noise variance N_0 is set to -89 dBm for the 2D and -100 dBm for the 3D scenario. Assuming that the UE is moving in different

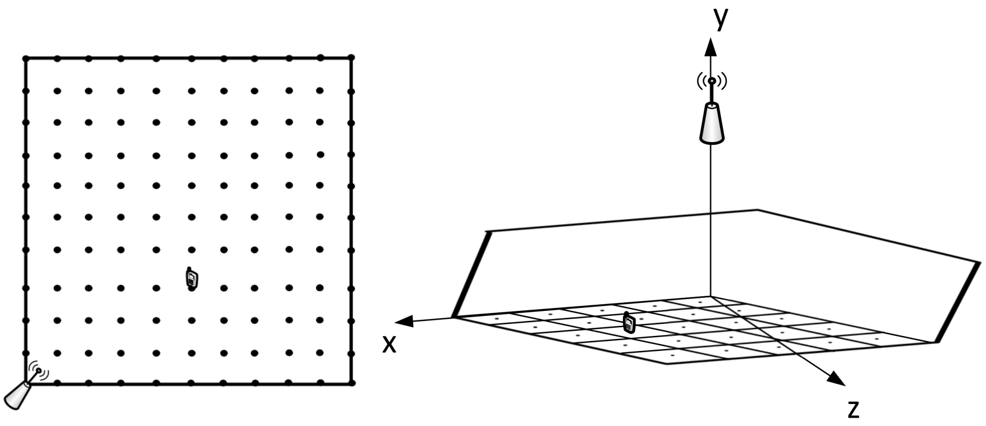

(a) 2D scenario,

(b) 3D scenario,

Figure 5.3: UE locations in 2D and 3D scenarios.

locations on the square (2D- Fig. 5.3a) and on one sector of a cell (3D- Fig. 5.3b), we average the earned PEB, affected by the transceivers' HWIs, over these discrete locations.

5.4.2 Performance Analysis

Fig. 5.4 and Fig. 5.5 illustrate the PEB with respect to the HWIs factor κ assuming different number of active RISs, in 2D and 3D scenarios, respectively. Considering the practical range for $\kappa \in [0.9, 1]$ [65], the average PEB over different UE locations is earned. As it can be seen from Fig. 5.5, with no active RIS, PEB rises sharply from 42.73 to 1289 meters, which are enormous amounts; however, activating 1 RIS, while other RISs acting as a reflector, improve the localization performance by 26.44 meters, when $\kappa = 1$; this is due to the phase correction using the active RIS, which maximizes the SNR. It is evident that, in 3D scenario, 2 active RISs has the best performance among the other cases, while more RISs in 2D scenario provides mildly better performance; in the other words, activating

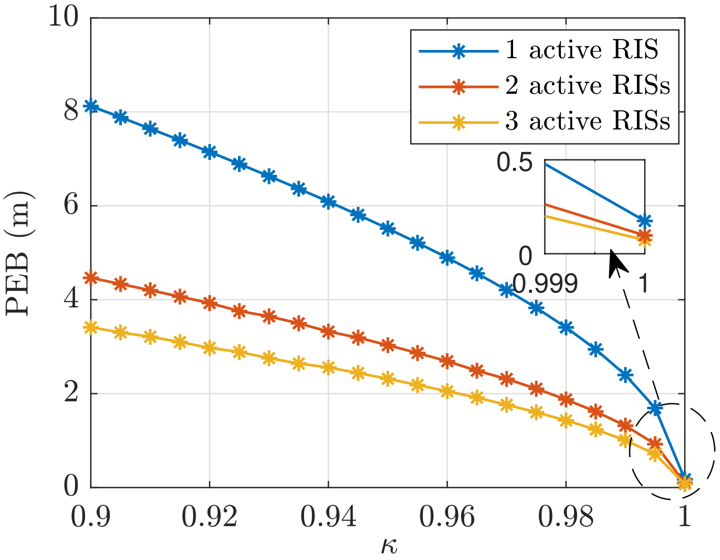

Figure 5.4: PEB w. r. t. the HWIs factors κ using different number of active RISs each with 100 elements in 2D scenario.

more RISs in a practical 3D scenario, does not boost the localization performance; this is because of better performance of spaced 2 RISs rather than 3 RISs. Moreover, in both scenarios, by activating 2 or more RISs, PEB stays more steady than one or no active RIS, as κ strays away from 1. In order to see how the behavior of the PEB is similar to the SNR, Fig. 5.6 is provided for the 3D scenario. As it can be seen from Fig. 5.6, activating more RISs escalate the SNR value; although this betterment is more explicit between no active RIS and 1 active RIS, than between 2 and 3 active RISs. Also, SNR deteriorates by HWIs with the same slope for all the cases. In general, the SNR improves by 2 dB by activating 3 RISs and this is due to the maximizing SNR in (5.30) by activating each RIS. Furthermore, Fig. 5.6 is in logarithmic unit and that is why in comparison with the PEB, SNR worsens less aggressively with HWIs.

In Fig. 5.7 and Fig. 5.8, we examined that in the both scenarios which factors between

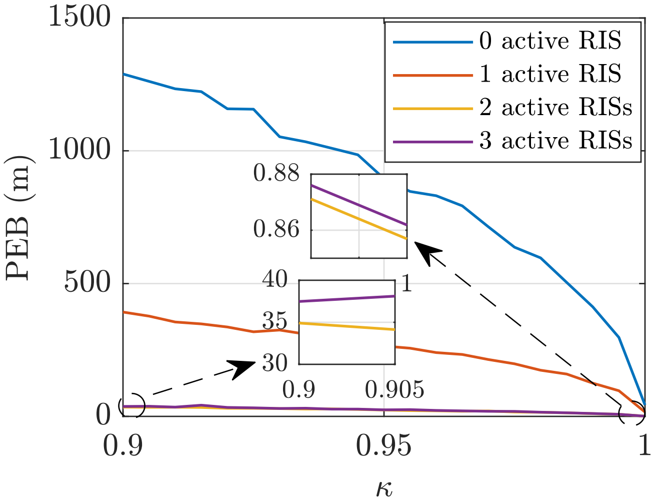

Figure 5.5: PEB w. r. t. the HWIs factors κ using different number of active RISs each with 100 elements in 3D scenario.

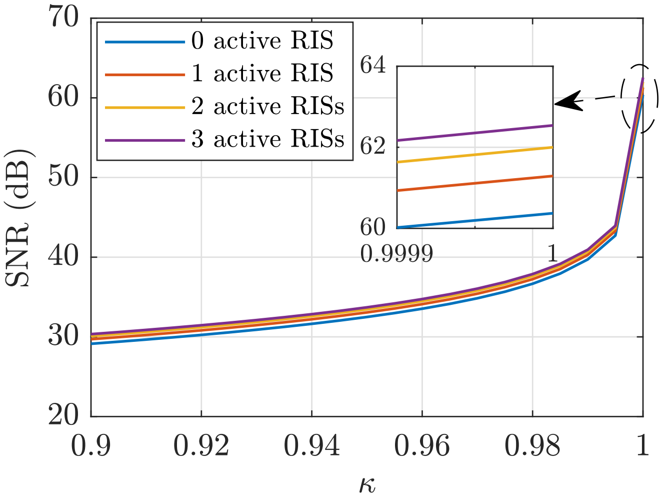

Figure 5.6: SNR w. r. t. the HWIs factors κ using different number of active RISs each with 100 elements in 3D scenario.

number of elements in each RIS and the number of RISs, are more useful to boost the localization system affected by HWIs. Hence, we considered the following cases,

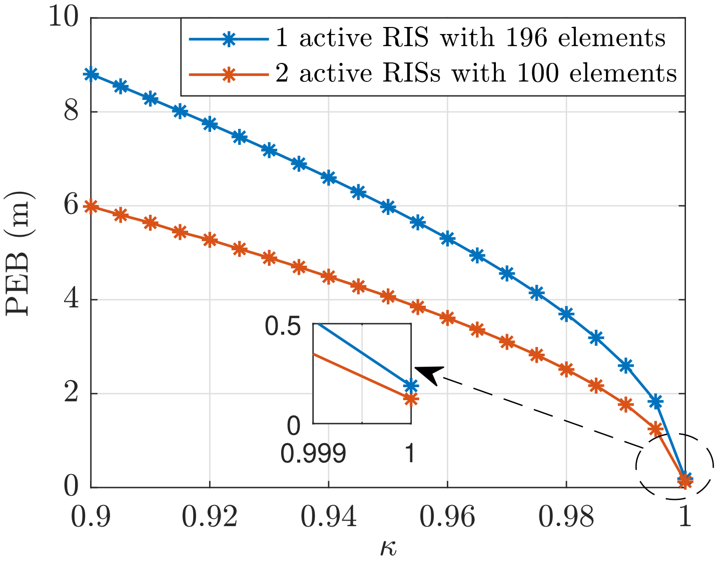

Figure 5.7: PEB w. r. t. the HWIs factors κ in two different cases (2D scenario): 1)RIS allocation vector $\boldsymbol{a} = [1, 1, 0]$ each with 100 elements, 2)RIS allocation vector $\boldsymbol{a} = [1, 0, 0]$ each with 196 elements.

- 1 active RIS with almost 2m elements,
- 2 active RISs each with m elements,

From the both Fig. 5.7 and Fig. 5.8, it is evident that activating more RISs in 2D and 3D has superior performance than using more elements in each RIS; This is again due to the space between the elements. In the other words, each elements in the RIS are spaced by $\lambda/2$, however, each RISs are located 2-3 meters away from each other; i. e, more distance, better performance. This fact is apparent in Fig. 5.9 for the 2D scenario and Fig. 5.10 for the 3D scenario.

Fig. 5.9 shows how PEB changes with the inter RIS space in 2D scenario for three different HWIs factor $\kappa = 1$, $\kappa = 0.94$ and $\kappa = 0.9$ and Fig. 5.10 presents the PEB alteration with respect to the inter RIS space in 3D scenario, for two different values of HWIs factor.

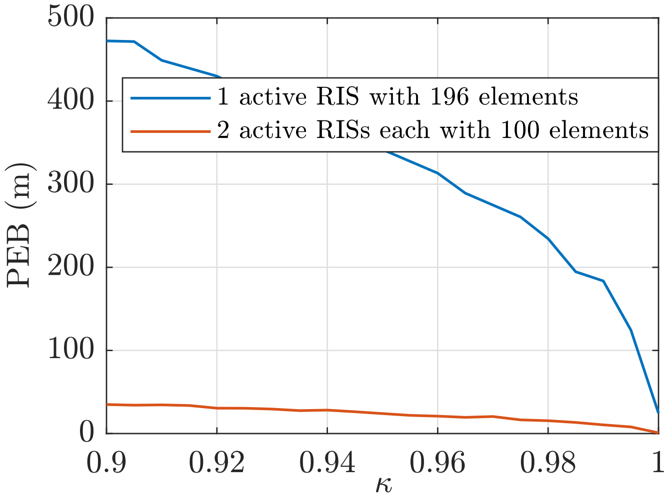

Figure 5.8: PEB w. r. t. the HWIs factors κ in two different cases (3D scenario): 1)RIS allocation vector $\boldsymbol{a} = [1, 1, 0]$ each with 100 elements, 2)RIS allocation vector $\boldsymbol{a} = [1, 0, 0]$ each with 196 elements.

In the both scenarios with different amount of HWIs, PEB drops as the distance between RISs increases. Although, this distance is more effective in non-ideal transceivers. As the distance between the RISs increases, the incoming signals from different RISs are more resolveable, leading to more accurate estimation; this fact decreases the amount of PEB.

Finally, Fig. 5.11 presents the PEB corresponding to the UE location in the sector considering ideal HWIs and 2 active RISs in 3D scenario. When the UE is close to the either the BS or the RISs, its localization is more accurate than other points. This is due to the receiving stronger signal which increases the SNR.

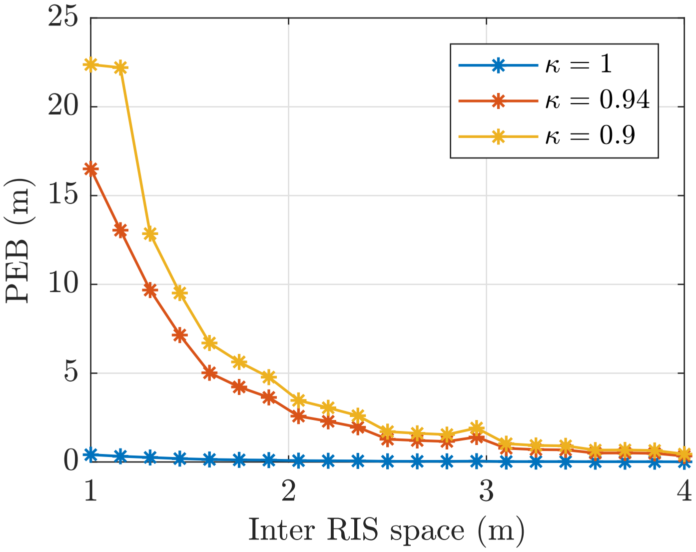

Figure 5.9: PEB w. r. t. the inter RIS space considering two active RISs with RIS allocation vector $\boldsymbol{a} = [1, 1, 1]$ and two different HWIs factors κ in 2D scenario.

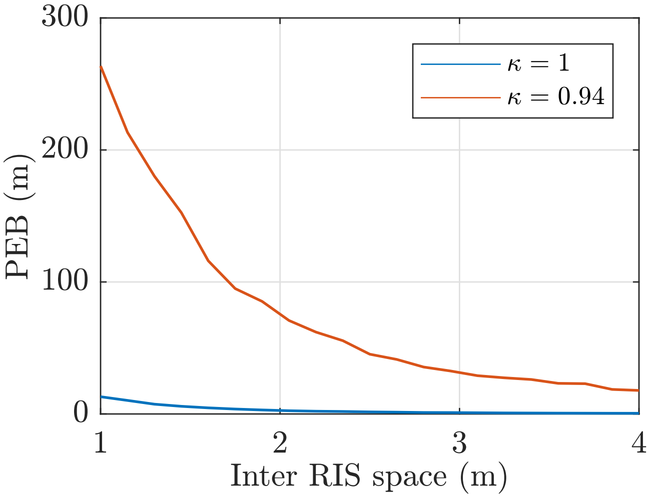

Figure 5.10: PEB w. r. t. the inter RIS space considering two active RISs with RIS allocation vector $\boldsymbol{a} = [1, 1, 0]$ and two different HWIs factors κ in 3D scenario.

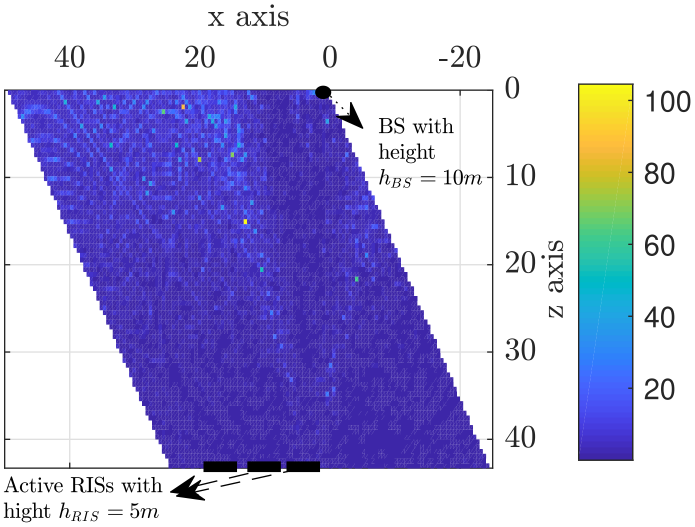

Figure 5.11: PEB w. r. t. the UE location in a diamond shape sector considering ideal HWIs and RIS allocation vector $\boldsymbol{a} = [1, 1, 0]$.

5.5 Conclusion

In this chapter, the effects of hardware impairments (HWIs) on the UE localization with the assistance of the reflecting intelligence surfaces (RISs), for two (2D) and three dimensional (3D) scenarios, is presented. As expected, due to the incoming signal's phase optimization by RISs, more active RISs leads to the less localization error; however, results reveal that there is a threshold for the number of the activated RISs in 3D scenario and after activating limited number of RISs, more RISs do not improve the localization process. Even, this fact can be seen in the 2D scenario, as the betterment of the localization performance decreases by activating more than two RISs. On the other hand, in 3D scenario, signal to noise ratio (SNR) rises with more active RISs and as HWIs factor gets closer to 1. Plus, the slope of SNR drop with respect to the HWIs factor κ, is the same for different active RISs.

Furthermore, based on our results, activating more RISs with less elements is more helpful in the localization process than installing more elements in each active RIS. In addition, more inter RIS space, reduces the user position error bound (PEB).

Future works based on this chapter can include considering multiple antennas at the transceivers. Also, the effect of asynchronous transceivers in RIS aided localization along with HWIs can be examined.

5.6 Publications Resulted from This Chapter

- F. Ghaseminajm, M. Alsmadi, S. S. Ikki, "RIS-aided Mobile Localization Error Bounds Under Hardware Impairments," to be submitted in *IEEE systems journal.*

Chapter 6

Conclusions and Future research

This thesis presented a research on the user equipment (UE)'s localization error bounds under hardware impairments (HWIs) conditions while concentrating on different scenarios in 5G mmWave communication systems. This chapter provides the final conclusions based on the contributions mentioned in section 1.5.

6.1 Conclusions

- Examining the effect of HWIs on UE's localization in 2D scenario is provided in chapter 3. Focusing on the line of sight (LOS) path in uplink transmission, the received signal model and the received noise covariance is derived. After deriving the Fisher information matrix (FIM) of the unknown parameters, we then transformed them to the location parameters' FIM. Finally, we accomplished the error analysis and earned the numerically calculated Cramèr-Rao lower bounds (CRLB) for the position and orientation of the UE. By comparing the numerical results, we show that both the position (PEB) and orientation error bounds (OEB) deteriorate intensively as HWIs worsen and they are at minimum in perfect circumstances. Although, the amount of PEB and OEB degradation for non-tilted UE are the same, OEB degradation becomes more than PEB deterioration for the tilted UE.

- The first part of chapter 4 extended the effect of HWIs on UE localization error bounds discussed in chapter 3, to the 3D scenario. In this scenario, which is introduced as one way localization (OWL)- case 1, the UE and the base station (BS) are assumed to be timely synchronized. On the other hand, considering asynchronous transceivers and in order to eliminate the clock bias, we examined the effect of HWIs on UE's PEB and OEB in two other OWL cases, as well. In OWL- case 2 and 3, the localization information earned by the neighboring BS is also utilized. OWL- case 2 profits from the second BS to cancel the clock bias and OWL- case 3 takes advantages of the both spatial and temporal information obtained through the redundant BS. Besides these three cases, we investigated two other scenarios based on the two way localization (TWL): round-trop (RLP) and collaborative localization protocols (CLP). The former, involves UE for estimating the forward transmission delay and the latter is based on the complete collaboration between the BS and the UE. After obtaining the signal model and received noise covariance for the both forward and backward transmissions, which is the same for all of the scenarios, the FIM of unknown parameters and consequently the location parameters' FIM are derived per scenario. Finally, we compared the behavior of the error bounds as HWIs worsen. Comparing the numerical results reveals that CLP has the superior performance over other cases; However, OWL- case 3 shows the least degradation percentage with respect to the HWIs factor. Moreover, except the clock bias elimination, there is no supremacy of RLP over OWL.

- In chapter 5, in order to overcoming the intense deteriorated localization caused by HWIs, we exploited the installed reconfigurable intelligent surfaces (RISs) on the edge of the square in 2D scenario and on the edge of the cell in 3D scenario. As expected, the results indicate that installing RISs in collaboration with even a single anchor, is extremely beneficial in facing HWIs conditions. Furthermore, we understood through 3D scenario, adding more RISs does not necessarily improve the localization performance under HWIs. However, more distance between RISs is immensely helpful in declining position error bounds; this fact is more evident when hardware is more malfunctioned. Moreover, in the scenario of RIS-aided localization, PEB declines more in comparison with the SNR, in presence of HWIs.

The major outcome of this thesis is to understand this fact that the hardware implemented in the transceivers comes with some minor deficiencies; this can extremely affect the localization performance in 5G localization systems, as we saw through the numerical performance bounds. Based on our results, we know which algorithms and methods are the best in tackling HWIs. This thesis introduces a solid mathematical framework for the study of different types of localization systems under realistic scenarios; however it comes with some assumptions that can be considered as the limitations of the presented research. Our research could also motivate other researchers to explore further investigations. To that end, this thesis can be considered as a benchmark.

6.2 Limitations of the presented work

Throughout the derivations and calculations of the UE error bounds in different scenarios, some assumptions are considered. These assumptions are made in order to simplifying the complications of the mathematical derivations and can be considered as limitations of the presented work as follows.

- In chapter 2, section 2.2, in order to model the HWIs, we assume that the input and the output signal power are the same. In reality, some compensation algorithms need to be used which increases the complexity of the system.
- In chapter 2, section 2.3.1, we assume that the estimator is unbiased in which $\mathbb{E}[\hat{\theta}] = \theta$. Considering a biased estimator, would add a bias to each FIM element.
- In chapter 2, section 2.4, we considered that the electromagnetic elements used in RISs are not lossy; however, RIS elements can be lossy and subsequently change the amplitude of the reflected signal.
- In chapter 3, section 3.2.1, we assume that the receiver beams are orthogonal as of sparse transmission in 5G mmWave communication systems; so that $\boldsymbol{W}^{\mathrm{H}}\boldsymbol{W} = \boldsymbol{I}_{\mathrm{N_B}}$. However, this may not be exactly equal to the identity and this will change the noise covariance.
- In chapters 3 and 4, we assume that all the antennas at the transmitter are imperfect with the same factor κ_{s}. This is not correct in reality. However, considering independent imperfection would add N_{T} unknown parameters; which would complicate our derivations.

6.3 Future Research Directions

Limitations of mmWave communication systems and its challenges are still is one of the attractive topics among researchers. Based on our findings, general HWIs have severe effects on the 5G mmWave localization systems; however, there are still so many open research topics that can be enumerated as follow.

- **Spacial cases for HWIs:** Generally, HWIs can include phase noise, nonlinear power amplifier and I/Q imbalance. The received signal model for each special case of HWIs is different and so that the performance analysis might be different. Our research can be used as a benchmark for all the other mentioned special cases.

- **Estimators:** We have addressed the minimum error bounds of any estimators for the UE localization in each scenario. Applying and designing estimation algorithms, such as Maximum likelihood estimation (MLE) algorithm, on the mentioned scenarios can be considered as a next step to practically show the localization performance under HWIs circumstances. Bench-marking those techniques with the derived PEB and OEB, approves the functionality of the estimators.

- **Phased array configurations:** We derived the UE localization error bounds based on the radio frequency (RF) phase-shifting configuration. In this configuration, after mounting the signal on the desired frequency, its phase for beamforming is shifted. There are three other beamforming configurations including: local oscillator (LO) phase shifting, intermediate frequency (IF) phase shifting and digital beamforming. Comparing all these four configurations will give a comprehensive view of the localization performance under HWIs.

- **Realistic scenarios:** The considered scenario in this thesis does not include non line-of-sight (NLOS) paths, mobilized user and indoor localization. As it is explained earlier, mmWave contains few paths and therefore LoS path contains most of the information; for this reason, we expect, considering NLOS paths might make a negligible change on our results; however, they can be exploited in indoor scenarios as may the LoS path is blocked. Also, finding the localization bounds for the moving user will open another topic for tracking the UE using estimators in practical applications such as vehicular communication systems.

- **New applications:** Addressing the positioning error bounds affected by HWIs in device-to-device, vehicle-to-vehicle and internet-of-things applications can also be considered as another new research topic.

APPENDICES

Appendix A

Derivation of FIM elements $\boldsymbol{J}_{\mathrm{C}}$ in 2D scenario

In order to derive the entries of (3.7), we define the following parameters:

$$\boldsymbol{p}_{\mathrm{R}} \triangleq \frac{\partial}{\partial \theta_{\mathrm{R}}} \boldsymbol{a}_{\mathrm{R}}(\theta_{\mathrm{R}}), \tag{A.1a}$$

$$\boldsymbol{p}_{\mathrm{T}} \triangleq \frac{\partial}{\partial \theta_{\mathrm{T}}} \boldsymbol{a}_{\mathrm{T}}(\theta_{\mathrm{T}}), \tag{A.1b}$$

$$\dot{\boldsymbol{s}} \triangleq \frac{\partial \boldsymbol{s}(t)}{\partial \tau}, \tag{A.1c}$$

$$\gamma_0 \triangleq \frac{2EN_{\mathrm{s}}}{\sigma_{\mathrm{z}}^2}, \tag{A.1d}$$

$$\gamma_1 \triangleq \frac{4T_0E^2N_{\mathrm{B}}^2}{\sigma_{\mathrm{z}}^4}, \tag{A.1e}$$

and by deriving following derivatives

$$\frac{\partial \boldsymbol{\mu}(t)}{\partial \theta_{\mathrm{R}}} = \kappa\beta \boldsymbol{W}^{\mathrm{H}} \boldsymbol{p}_{\mathbf{R}}(\theta_{\mathrm{R}}) {\boldsymbol{a}_{\mathbf{T}}}^{\mathrm{H}}(\theta_{\mathrm{T}}) \boldsymbol{F} \boldsymbol{s}(t-\tau), \tag{A.2a}$$

$$\frac{\partial \boldsymbol{\mu}(t)}{\partial \theta_{\mathrm{T}}} = \kappa\beta \boldsymbol{W}^{\mathrm{H}} \boldsymbol{a}_{\mathbf{R}}(\theta_{\mathrm{R}}) {\boldsymbol{p}_{\mathbf{T}}}^{\mathrm{H}}(\theta_{\mathrm{T}}) \boldsymbol{F} \boldsymbol{s}(t-\tau), \tag{A.2b}$$

$$\frac{\partial \boldsymbol{\mu}(t)}{\partial \tau} = \kappa\beta \boldsymbol{W}^{\mathrm{H}} \boldsymbol{a}_{\mathbf{R}}(\theta_{\mathrm{R}}) {\boldsymbol{a}_{\mathbf{T}}}^{\mathrm{H}}(\theta_{\mathrm{T}}) \boldsymbol{F} \dot{\boldsymbol{s}}(t-\tau), \tag{A.2c}$$

$$\frac{\partial \boldsymbol{\mu}(t)}{\partial \beta_{\mathrm{R}}} = \kappa \boldsymbol{W}^{\mathrm{H}} \boldsymbol{a}_{\mathbf{R}}(\theta_{\mathrm{R}}) {\boldsymbol{a}_{\mathbf{T}}}^{\mathrm{H}}(\theta_{\mathrm{T}}) \boldsymbol{F} \boldsymbol{s}(t-\tau), \tag{A.2d}$$

$$\frac{\partial \boldsymbol{\mu}(t)}{\partial \beta_{\mathrm{I}}} = j\kappa \boldsymbol{W}^{\mathrm{H}} \boldsymbol{a}_{\mathbf{R}}(\theta_{\mathrm{R}}) {\boldsymbol{a}_{\mathbf{T}}}^{\mathrm{H}}(\theta_{\mathrm{T}}) \boldsymbol{F} \boldsymbol{s}(t-\tau), \tag{A.2e}$$

$$\frac{\partial \boldsymbol{\mu}(t)}{\partial \kappa} = \beta \boldsymbol{W}^{\mathrm{H}} \boldsymbol{a}_{\mathbf{R}}(\theta_{\mathrm{R}}) {\boldsymbol{a}_{\mathbf{T}}}^{\mathrm{H}}(\theta_{\mathrm{T}}) \boldsymbol{F} \boldsymbol{s}(t-\tau), \tag{A.2f}$$

and using the following signal correlation relationship

$$\int_0^{T_0} \boldsymbol{s}(t-\tau)\boldsymbol{s}^{\mathrm{H}}(t-\tau)\mathrm{d}t = N_{\mathrm{s}} \boldsymbol{I}_{N_{\mathrm{B}}}, \tag{A.3a}$$

$$\int_0^{T_0} \frac{\partial \boldsymbol{s}(t-\tau)}{\partial \tau} \frac{\partial \boldsymbol{s}^{\mathrm{H}}(t-\tau)}{\partial \tau} \mathrm{d}t = 4\pi^2 N_{\mathrm{s}} W_{\mathrm{eff}}^2 \boldsymbol{I}_{N_{\mathrm{B}}}, \tag{A.3b}$$

$$\int_0^{T_0} \frac{\partial \boldsymbol{s}(t-\tau)}{\partial \tau} \boldsymbol{s}^{\mathrm{H}}(t-\tau)\mathrm{d}t = \mathbf{0}, \tag{A.3c}$$

where $W_{\text{eff}}^2 \triangleq \int_{-W/2}^{W/2} f^2 |P(f)|^2 \mathrm{d}f$ and W is the bandwidth, the elements of (3.7) can be calculated as below

$$J_{\theta_{\mathrm{R}}\theta_{\mathrm{R}}} = \gamma_0 \kappa^2 |\beta|^2 \|\boldsymbol{p}_R^H \boldsymbol{W}\|^2 \|\boldsymbol{a}_T^H \boldsymbol{F}\|^2, \tag{A.4a}$$

$$J_{\theta_{\mathrm{R}}\theta_{\mathrm{T}}} = \gamma_0 \kappa^2 |\beta|^2 \Re\left\{(\boldsymbol{p}_T^H \boldsymbol{F}\boldsymbol{F}^H \boldsymbol{a}_T)(\boldsymbol{p}_R^H \boldsymbol{W}\boldsymbol{W}^H \boldsymbol{a}_R)\right\}, \tag{A.4b}$$

$$J_{\theta_{\mathrm{R}}\beta_{\mathrm{R}}} = \gamma_0 \kappa^2 \|\boldsymbol{a}_T^H \boldsymbol{F}\|^2 \Re\left\{\beta^* \boldsymbol{p}_R^H \boldsymbol{W}\boldsymbol{W}^H \boldsymbol{a}_R\right\}, \tag{A.4c}$$

$$J_{\theta_{\mathrm{R}}\beta_{\mathrm{I}}} = -\gamma_0 \kappa^2 \|\boldsymbol{a}_T^H \boldsymbol{F}\|^2 \Im\left\{\beta^* \boldsymbol{p}_R^H \boldsymbol{W}\boldsymbol{W}^H \boldsymbol{a}_R\right\}, \tag{A.4d}$$

$$J_{\theta_{\mathrm{R}}\kappa} = \gamma_0 \kappa |\beta|^2 \|\boldsymbol{a}_T^H \boldsymbol{F}\|^2 \Re\left\{\boldsymbol{p}_R^H \boldsymbol{W}\boldsymbol{W}^H \boldsymbol{a}_R\right\}, \tag{A.4e}$$

$$J_{\theta_{\mathrm{T}}\theta_{\mathrm{T}}} = \gamma_0 \kappa^2 |\beta|^2 \|\boldsymbol{a}_R^H \boldsymbol{W}\|^2 \|\boldsymbol{p}_T^H \boldsymbol{F}\|^2, \tag{A.4f}$$

$$J_{\theta_{\mathrm{T}}\beta_{\mathrm{R}}} = \gamma_0 \kappa^2 \|\boldsymbol{a}_R^H \boldsymbol{W}\|^2 \Re\left\{\beta^* \boldsymbol{a}_T^H \boldsymbol{F}\boldsymbol{F}^H \boldsymbol{p}_T\right\}, \tag{A.4g}$$

$$J_{\theta_{\mathrm{T}}\beta_{\mathrm{I}}} = -\gamma_0 \kappa^2 \|\boldsymbol{a}_R^H \boldsymbol{W}\|^2 \Im\left\{\beta^* \boldsymbol{a}_T^H \boldsymbol{F}\boldsymbol{F}^H \boldsymbol{p}_T\right\}, \tag{A.4h}$$

$$J_{\theta_{\mathrm{T}}\kappa} = \gamma_0 \kappa |\beta|^2 \|\boldsymbol{a}_R^H \boldsymbol{W}\|^2 \Re\left\{\boldsymbol{a}_T^H \boldsymbol{F}\boldsymbol{F}^H \boldsymbol{p}_T\right\}, \tag{A.4i}$$

$$J_{\tau\tau} = 4\gamma_0 \pi^2 W_{eff}^2 \kappa^2 |\beta|^2 \|\boldsymbol{a}_R^H \boldsymbol{W}\|^2 \|\boldsymbol{a}_T^H \boldsymbol{F}\|^2, \tag{A.4j}$$

$$J_{\beta_{\mathrm{R}}\beta_{\mathrm{R}}} = \gamma_1 (1-\kappa^2)^2 \beta_R^2 + \gamma_0 \kappa^2 \|\boldsymbol{a}_R^H \boldsymbol{W}\|^2 \|\boldsymbol{a}_T^H \boldsymbol{F}\|^2, \tag{A.4k}$$

$$J_{\beta_{\mathrm{R}}\beta_{\mathrm{I}}} = \gamma_1 (1-\kappa^2)^2 \beta_R \beta_I, \tag{A.4l}$$

$$J_{\beta_{\mathrm{R}}\kappa} = \gamma_0 \kappa \beta_R \|\boldsymbol{a}_R^H \boldsymbol{W}\|^2 \|\boldsymbol{a}_T^H \boldsymbol{F}\|^2 - \gamma_1 \kappa |\beta|^2 \beta_R (1-\kappa^2), \tag{A.4m}$$

$$J_{\beta_{\mathrm{I}}\beta_{\mathrm{I}}} = \gamma_1 (1-\kappa^2)^2 \beta_I^2 + \gamma_0 \kappa^2 \|\boldsymbol{a}_R^H \boldsymbol{W}\|^2 \|\boldsymbol{a}_T^H \boldsymbol{F}\|^2, \tag{A.4n}$$

$$J_{\beta_{\mathrm{I}}\kappa} = -\gamma_1 \kappa |\beta|^2 \beta_I (1-\kappa^2) + \gamma_0 \kappa \beta_I \|\boldsymbol{a}_R^H \boldsymbol{W}\|^2 \|\boldsymbol{a}_T^H \boldsymbol{F}\|^2, \tag{A.4o}$$

$$J_{\kappa\kappa} = \gamma_1 \kappa^2 |\beta|^4 + \gamma_0 |\beta|^2 \|\boldsymbol{a}_R^H \boldsymbol{W}\|^2 \|\boldsymbol{a}_T^H \boldsymbol{F}\|^2. \tag{A.4p}$$

Appendix B

Derivation of FIM elements in 3D scenario under imperfect synchronization

B.1 FIM elements for two-way scenario

By defining the following parameters

$$
\begin{aligned}
\boldsymbol{p}_1 &\triangleq \frac{\partial}{\partial \phi_1}\boldsymbol{a}_1(\boldsymbol{v}_1), & \boldsymbol{h}_1 &\triangleq \frac{\partial}{\partial \theta_1}\boldsymbol{a}_1(\boldsymbol{v}_1),\\
\boldsymbol{p}_2 &\triangleq \frac{\partial}{\partial \phi_2}\boldsymbol{a}_2(\boldsymbol{v}_2), & \boldsymbol{h}_2 &\triangleq \frac{\partial}{\partial \theta_2}\boldsymbol{a}_2(\boldsymbol{v}_2),\\
\dot{\boldsymbol{s}}_1 &\triangleq \frac{\partial \boldsymbol{s}_1(t)}{\partial \tau^{\mathrm{f}}}, & \dot{\boldsymbol{s}}_2 &\triangleq \frac{\partial \boldsymbol{s}_2(t)}{\partial \tau^{\mathrm{b}}},\\
\gamma_0 &\triangleq \frac{2EN_{\mathrm{s}}}{\sigma_{\mathrm{z}}^2}, & \gamma_1 &\triangleq \frac{4T_0E^2N_{\mathrm{B}}^2}{\sigma_{\mathrm{z}}^4},
\end{aligned}
$$

the derivatives of the received signal $\boldsymbol{\mu_1}(t)$ are calculated as below (for the convenience the AoA and AoD are removed)

$$
\begin{aligned}
\frac{\partial \boldsymbol{\mu_1}(t)}{\partial \phi_1} &= \kappa\beta {\boldsymbol{W}^{\mathrm{b}}}^{\mathrm{H}} \boldsymbol{p_1} {\boldsymbol{a_2}}^{\mathrm{H}} \boldsymbol{F}^{\mathrm{b}} \boldsymbol{s}_2(t-\tau^{\mathrm{b}}), \\
\frac{\partial \boldsymbol{\mu_1}(t)}{\partial \phi_2} &= \kappa\beta {\boldsymbol{W}^{\mathrm{b}}}^{\mathrm{H}} \boldsymbol{a_1} {\boldsymbol{p_2}}^{\mathrm{H}} \boldsymbol{F}^{\mathrm{b}} \boldsymbol{s}_2(t-\tau^{\mathrm{b}}), \\
\frac{\partial \boldsymbol{\mu_1}(t)}{\partial \theta_1} &= \kappa\beta {\boldsymbol{W}^{\mathrm{b}}}^{\mathrm{H}} \boldsymbol{h_1} {\boldsymbol{a_2}}^{\mathrm{H}} \boldsymbol{F}^{\mathrm{b}} \boldsymbol{s}_2(t-\tau^{\mathrm{b}}), \\
\frac{\partial \boldsymbol{\mu_1}(t)}{\partial \theta_2} &= \kappa\beta {\boldsymbol{W}^{\mathrm{b}}}^{\mathrm{H}} \boldsymbol{a_1} {\boldsymbol{h_2}}^{\mathrm{H}} \boldsymbol{F}^{\mathrm{b}} \boldsymbol{s}_2(t-\tau^{\mathrm{b}}), \\
\frac{\partial \boldsymbol{\mu_1}(t)}{\partial \tau^{\mathrm{b}}} &= \kappa\beta {\boldsymbol{W}^{\mathrm{b}}}^{\mathrm{H}} \boldsymbol{a_1} {\boldsymbol{a_2}}^{\mathrm{H}} \boldsymbol{F}^{\mathrm{b}} \dot{\boldsymbol{s}}_2(t-\tau^{\mathrm{b}}), \\
\frac{\partial \boldsymbol{\mu_1}(t)}{\partial \beta_{\mathrm{R}}} &= \kappa {\boldsymbol{W}^{\mathrm{b}}}^{\mathrm{H}} \boldsymbol{a_1} {\boldsymbol{a_2}}^{\mathrm{H}} \boldsymbol{F}^{\mathrm{b}} \boldsymbol{s}_2(t-\tau^{\mathrm{b}}), \\
\frac{\partial \boldsymbol{\mu_1}(t)}{\partial \beta_{\mathrm{I}}} &= j\kappa {\boldsymbol{W}^{\mathrm{b}}}^{\mathrm{H}} \boldsymbol{a_1} {\boldsymbol{a_2}}^{\mathrm{H}} \boldsymbol{F}^{\mathrm{b}} \boldsymbol{s}_2(t-\tau^{\mathrm{b}}), \\
\frac{\partial \boldsymbol{\mu_1}(t)}{\partial \kappa} &= \beta {\boldsymbol{W}^{\mathrm{b}}}^{\mathrm{H}} \boldsymbol{a_1} {\boldsymbol{a_2}}^{\mathrm{H}} \boldsymbol{F}^{\mathrm{b}} \boldsymbol{s}_2(t-\tau^{\mathrm{b}}),
\end{aligned}
$$

Now, defining the operator $\boldsymbol{O_A} \triangleq \boldsymbol{A}(\boldsymbol{A}^{\mathrm{H}}\boldsymbol{A})^{-1}\boldsymbol{A}^{\mathrm{H}}$ and using (4.14), FIM of the parameters $\{\boldsymbol{\upsilon}^{\mathrm{b}}, \boldsymbol{\beta}, \kappa, \tau\}$ for the backward transmission is derived as below

$$
\begin{aligned}
J_{\phi_1\phi_1} &= \gamma_0\kappa^2|\beta|^2||\boldsymbol{a}_2^H\boldsymbol{F}^{\mathrm{b}}||^2\Re\left\{(\boldsymbol{p}_1^{\mathrm{H}}\boldsymbol{O}_{\boldsymbol{W}^{\mathrm{b}}}\boldsymbol{p}_1)\right\}, \\
J_{\phi_1\phi_2} &= \gamma_0\kappa^2|\beta|^2\Re\left\{(\boldsymbol{p}_2^H\boldsymbol{F}^{\mathrm{b}}{\boldsymbol{F}^{\mathrm{b}}}^H\boldsymbol{a}_2)(\boldsymbol{p}_1^H\boldsymbol{O}_{\boldsymbol{W}^{\mathrm{b}}}\boldsymbol{a}_1)\right\}, \\
J_{\phi_1\theta_1} &= \gamma_0\kappa^2|\beta|^2||\boldsymbol{a}_2^H\boldsymbol{F}^{\mathrm{b}}||^2\Re\left\{\boldsymbol{p}_1^{\mathrm{H}}\boldsymbol{O}_{\boldsymbol{W}^{\mathrm{b}}}\boldsymbol{h}_1\right\}, \\
J_{\phi_1\theta_2} &= \gamma_0\kappa^2|\beta|^2\Re\left\{(\boldsymbol{h}_2^H\boldsymbol{F}^{\mathrm{b}}{\boldsymbol{F}^{\mathrm{b}}}^H\boldsymbol{a}_2)(\boldsymbol{p}_1^{\mathrm{H}}\boldsymbol{O}_{\boldsymbol{W}^{\mathrm{b}}}\boldsymbol{a}_1)\right\}, \\
J_{\phi_1\beta_{\mathrm{R}}} &= \gamma_0\kappa^2||\boldsymbol{a}_2^H\boldsymbol{F}^{\mathrm{b}}||^2\Re\left\{\beta^*\boldsymbol{p}_1^H\boldsymbol{O}_{\boldsymbol{W}^{\mathrm{b}}}\boldsymbol{a}_1\right\}, \\
J_{\phi_1\beta_{\mathrm{I}}} &= -\gamma_0\kappa^2||\boldsymbol{a}_2^H\boldsymbol{F}^{\mathrm{b}}||^2\Im\left\{\beta^*\boldsymbol{p}_1^H\boldsymbol{O}_{\boldsymbol{W}^{\mathrm{b}}}\boldsymbol{a}_1\right\},
\end{aligned}
$$

$$
\begin{aligned}
J_{\phi_1\kappa} &= \gamma_0\kappa|\beta|^2||\boldsymbol{a}_2^H\boldsymbol{F}^{\mathrm{b}}||^2\Re\left\{\boldsymbol{p}_1^H\boldsymbol{O}_{\boldsymbol{W}^{\mathrm{b}}}\boldsymbol{a}_1\right\},\\
J_{\phi_2\phi_2} &= \gamma_0\kappa^2|\beta|^2||\boldsymbol{p}_2^H\boldsymbol{F}^{\mathrm{b}}||^2\Re\left\{(\boldsymbol{a}_1^H\boldsymbol{O}_{\boldsymbol{W}^{\mathrm{b}}}\boldsymbol{a}_1)\right\},\\
J_{\phi_2\theta_1} &= \gamma_0\kappa^2|\beta|^2\Re\left\{(\boldsymbol{a}_2^H\boldsymbol{F}^{\mathrm{b}}\boldsymbol{F}^{\mathrm{b}^H}\boldsymbol{p}_2)(\boldsymbol{a}_1^H\boldsymbol{O}_{\boldsymbol{W}^{\mathrm{b}}}\boldsymbol{h}_1)\right\},\\
J_{\phi_2\theta_2} &= \gamma_0\kappa^2|\beta|^2\Re\left\{(\boldsymbol{h}_2^H\boldsymbol{F}^{\mathrm{b}}\boldsymbol{F}^{\mathrm{b}^{\mathrm{H}}}\boldsymbol{p}_2)(\boldsymbol{a}_1^{\mathrm{H}}\boldsymbol{O}_{\boldsymbol{W}^{\mathrm{b}}}\boldsymbol{a}_1)\right\},\\
J_{\phi_2\beta_{\mathrm{R}}} &= \gamma_0\kappa^2\Re\left\{\beta^*(\boldsymbol{a}_2^H\boldsymbol{F}^{\mathrm{b}}\boldsymbol{F}^{\mathrm{b}^H}\boldsymbol{p}_2)(\boldsymbol{a}_1^H\boldsymbol{O}_{\boldsymbol{W}^{\mathrm{b}}}\boldsymbol{a}_1)\right\},\\
J_{\phi_2\beta_{\mathrm{I}}} &= -\gamma_0\kappa^2\Im\left\{\beta^*(\boldsymbol{a}_2^H\boldsymbol{F}^{\mathrm{b}}\boldsymbol{F}^{\mathrm{b}^H}\boldsymbol{p}_2)(\boldsymbol{a}_1^H\boldsymbol{O}_{\boldsymbol{W}^{\mathrm{b}}}\boldsymbol{a}_1)\right\},\\
J_{\phi_2\kappa} &= \gamma_0\kappa|\beta|^2\Re\left\{(\boldsymbol{a}_2^H\boldsymbol{F}^{\mathrm{b}}\boldsymbol{F}^{\mathrm{b}^H}\boldsymbol{p}_2)(\boldsymbol{a}_1^H\boldsymbol{O}_{\boldsymbol{W}^{\mathrm{b}}}\boldsymbol{a}_1)\right\},\\
J_{\theta_1\theta_1} &= \gamma_0\kappa^2|\beta|^2||\boldsymbol{a}_2^H\boldsymbol{F}^{\mathrm{b}}||^2\Re\left\{(\boldsymbol{h}_1^H\boldsymbol{O}_{\boldsymbol{W}^{\mathrm{b}}}\boldsymbol{h}_1)\right\},\\
J_{\theta_1\theta_2} &= \gamma_0\kappa^2|\beta|^2\Re\left\{(\boldsymbol{h}_2^H\boldsymbol{F}^{\mathrm{b}}\boldsymbol{F}^{\mathrm{b}^H}\boldsymbol{a}_2)(\boldsymbol{h}_1^H\boldsymbol{O}_{\boldsymbol{W}^{\mathrm{b}}}\boldsymbol{a}_1)\right\},\\
J_{\theta_1\beta_{\mathrm{R}}} &= \gamma_0\kappa^2||\boldsymbol{a}_2^H\boldsymbol{F}^{\mathrm{b}}||^2\Re\left\{\beta^*(\boldsymbol{h}_1^H\boldsymbol{O}_{\boldsymbol{W}^{\mathrm{b}}}\boldsymbol{a}_1)\right\},\\
J_{\theta_1\beta_{\mathrm{I}}} &= -\gamma_0\kappa^2||\boldsymbol{a}_2^H\boldsymbol{F}^{\mathrm{b}}||^2\Im\left\{\beta^*(\boldsymbol{h}_1^H\boldsymbol{O}_{\boldsymbol{W}^{\mathrm{b}}}\boldsymbol{a}_1)\right\},\\
J_{\theta_1\kappa} &= \gamma_0\kappa|\beta|^2||\boldsymbol{a}_2^H\boldsymbol{F}^{\mathrm{b}}||^2\Re\left\{\boldsymbol{h}_1^H\boldsymbol{O}_{\boldsymbol{W}^{\mathrm{b}}}\boldsymbol{a}_1\right\},\\
J_{\theta_2\theta_2} &= \gamma_0\kappa^2|\beta|^2||\boldsymbol{h}_2^H\boldsymbol{F}^{\mathrm{b}}||^2\Re\left\{(\boldsymbol{a}_1^H\boldsymbol{O}_{\boldsymbol{W}^{\mathrm{b}}}\boldsymbol{a}_1)\right\},\\
J_{\theta_2\beta_{\mathrm{R}}} &= \gamma_0\kappa^2\Re\left\{\beta^*(\boldsymbol{a}_2^H\boldsymbol{F}^{\mathrm{b}}\boldsymbol{F}^{\mathrm{b}^H}\boldsymbol{h}_2)(\boldsymbol{a}_1^H\boldsymbol{O}_{\boldsymbol{W}^{\mathrm{b}}}\boldsymbol{a}_1)\right\},\\
J_{\theta_2\beta_{\mathrm{I}}} &= -\gamma_0\kappa^2\Im\left\{\beta^*(\boldsymbol{a}_2^H\boldsymbol{F}^{\mathrm{b}}\boldsymbol{F}^{\mathrm{b}^H}\boldsymbol{h}_2)(\boldsymbol{a}_1^H\boldsymbol{O}_{\boldsymbol{W}^{\mathrm{b}}}\boldsymbol{a}_1)\right\},\\
J_{\theta_2\kappa} &= \gamma_0\kappa|\beta|^2\Re\left\{(\boldsymbol{a}_2^H\boldsymbol{F}^{\mathrm{b}}\boldsymbol{F}^{\mathrm{b}^H}\boldsymbol{h}_2)(\boldsymbol{a}_1^H\boldsymbol{O}_{\boldsymbol{W}^{\mathrm{b}}}\boldsymbol{a}_1)\right\},\\
J_{\tau^{\mathrm{b}}\tau^{\mathrm{b}}} &= 4\gamma_0\pi^2W_{eff}^2\kappa^2|\beta|^2||\boldsymbol{a}_2^H\boldsymbol{F}^{\mathrm{b}}||^2\Re\left\{(\boldsymbol{a}_1^H\boldsymbol{O}_{\boldsymbol{W}^{\mathrm{b}}}\boldsymbol{a}_1)\right\},\\
J_{\beta_{\mathrm{R}}\beta_{\mathrm{R}}} &= \gamma_1(1-\kappa^2)^2\beta_R^2\gamma_0\kappa^2||\boldsymbol{a}_2^H\boldsymbol{F}^{\mathrm{b}}||^2\Re\left\{(\boldsymbol{a}_1^H\boldsymbol{O}_{\boldsymbol{W}^{\mathrm{b}}}\boldsymbol{a}_1)\right\},\\
J_{\beta_{\mathrm{R}}\beta_{\mathrm{I}}} &= \gamma_1(1-\kappa^2)^2\beta_R\beta_I-\gamma_0\kappa^2||\boldsymbol{a}_2^H\boldsymbol{F}^{\mathrm{b}}||^2\Im\left\{(\boldsymbol{a}_1^H\boldsymbol{O}_{\boldsymbol{W}^{\mathrm{b}}}\boldsymbol{a}_1)\right\},\\
J_{\beta_{\mathrm{R}}\kappa} &= -\gamma_1\kappa|\beta|^2\beta_R(1-\kappa^2)+\gamma_0\kappa\beta_R||\boldsymbol{a}_2^H\boldsymbol{F}^{\mathrm{b}}||^2\Re\left\{(\boldsymbol{a}_1^H\boldsymbol{O}_{\boldsymbol{W}^{\mathrm{b}}}\boldsymbol{a}_1)\right\},
\end{aligned}
$$

$$\begin{aligned}
J_{\beta_{\mathrm{I}}\beta_{\mathrm{I}}} &= \gamma_1(1-\kappa^2)^2\beta_I^2 + \gamma_0\kappa^2||\boldsymbol{a}_2^H\boldsymbol{F}^{\mathrm{b}}||^2\Re\left\{(\boldsymbol{a}_1^H\boldsymbol{O}_{\boldsymbol{W}^{\mathrm{b}}}\boldsymbol{a}_1)\right\},\\
J_{\beta_{\mathrm{I}}\kappa} &= -\gamma_1\kappa|\beta|^2\beta_I(1-\kappa^2) + \gamma_0\kappa\beta_I||\boldsymbol{a}_2^H\boldsymbol{F}^{\mathrm{b}}||^2\Re\left\{(\boldsymbol{a}_1^H\boldsymbol{O}_{\boldsymbol{W}^{\mathrm{b}}}\boldsymbol{a}_1)\right\},\\
J_{\kappa\kappa} &= \gamma_1\kappa^2|\beta|^4 + \gamma_0|\beta|^2||\boldsymbol{a}_2^H\boldsymbol{F}^{\mathrm{b}}||^2\Re\left\{(\boldsymbol{a}_1^H\boldsymbol{O}_{\boldsymbol{W}^{\mathrm{b}}}\boldsymbol{a}_1)\right\}.
\end{aligned}$$

Note that FIM for the forward transmission is achieved through $\boldsymbol{\mu}_{\mathbf{2}}(t)$ and it is as same as the derived FIM elements by exchanging subscripts "1" and "2" and also replacing superscripts "f" and "b". Besides that, for the OWL-cases 2 and 3, the FIM of the second anchor is derived similarly by transferring the second anchor to the origin. The location of device D_2 will consequently be $\boldsymbol{p} - \boldsymbol{p}_{\mathbf{2}}$.

B.2 Derivation of temporal parts of location FIM for the OWL- case 2 and 3

We define the FIM of the temporal parameters $\boldsymbol{\varphi}_{\mathrm{T}} \triangleq \{\tau_1^{\mathrm{b}}, \tau_2^{\mathrm{b}}\}$ as follows

$$\boldsymbol{J}_{\mathrm{T}} \triangleq \begin{bmatrix} J_{\tau_1^{\mathrm{b}}\tau_1^{\mathrm{b}}} & 0 \\ 0 & J_{\tau_2^{\mathrm{b}}\tau_2^{\mathrm{b}}} \end{bmatrix}, \in \mathbb{R}^{2\times 2}. \tag{B.1}$$

By transforming the temporal parameters $\boldsymbol{\varphi}_{\mathrm{T}}$ to location parameters $\boldsymbol{\varphi}_{\mathrm{L}}$ using $\boldsymbol{\Lambda}_{\mathbf{T}}$, the temporal component of the location parameters' FIM becomes

$$\boldsymbol{J}_{\mathrm{L-OWL2-Temporal}} = \boldsymbol{J}_{\mathrm{L-OWL3-Temporal}} = \boldsymbol{\Lambda}_{\mathbf{T}}\boldsymbol{J}_{\mathrm{T}}\boldsymbol{\Lambda}_{\mathbf{T}}^{\mathbf{T}}, \tag{B.2}$$

where

$$\boldsymbol{\Lambda}_{\mathbf{T}} = \frac{\partial \boldsymbol{\varphi}_{\mathrm{T}}}{\partial \boldsymbol{\varphi}_{\mathrm{L}}} = \begin{bmatrix} \frac{\partial \tau_1^{\mathrm{b}}}{\partial \boldsymbol{p}} & \frac{\partial \tau_2^{\mathrm{b}}}{\partial \boldsymbol{p}} \\ \frac{\partial \tau_1^{\mathrm{b}}}{\partial \boldsymbol{o}} & \frac{\partial \tau_2^{\mathrm{b}}}{\partial \boldsymbol{o}} \end{bmatrix}, \in \mathbb{R}^{5\times 2}. \tag{B.3}$$

After substituting (B.3) into (B.2), we obtain the following temporal part of $\boldsymbol{J}_{\mathrm{L-OWL2}}$ and $\boldsymbol{J}_{\mathrm{L-OWL3}}$, which was noted before in (4.23b) and (4.23c):

$$\begin{aligned} &\boldsymbol{J}_{\mathrm{L-OWL2-Temporal}} = \boldsymbol{J}_{\mathrm{L-OWL3-Temporal}} \\ &= J_{\tau_1^{\mathrm{b}}\tau_1^{\mathrm{b}}} \begin{bmatrix} \frac{\partial \tau_1^{\mathrm{b}}}{\partial \boldsymbol{p}} \\ \frac{\partial \tau_1^{\mathrm{b}}}{\partial \boldsymbol{o}} \end{bmatrix} \begin{bmatrix} \frac{\partial \tau_1^{\mathrm{b}}}{\partial \boldsymbol{p}} & \frac{\partial \tau_1^{\mathrm{b}}}{\partial \boldsymbol{o}} \end{bmatrix} + J_{\tau_2^{\mathrm{b}}\tau_2^{\mathrm{b}}} \begin{bmatrix} \frac{\partial \tau_2^{\mathrm{b}}}{\partial \boldsymbol{p}} \\ \frac{\partial \tau_2^{\mathrm{b}}}{\partial \boldsymbol{o}} \end{bmatrix} \begin{bmatrix} \frac{\partial \tau_2^{\mathrm{b}}}{\partial \boldsymbol{p}} & \frac{\partial \tau_2^{\mathrm{b}}}{\partial \boldsymbol{o}} \end{bmatrix}, \\ &= J_{\tau_1^{\mathrm{b}}\tau_1^{\mathrm{b}}} \boldsymbol{\Lambda}_\tau \boldsymbol{\Lambda}_\tau^{\mathrm{T}}|_{\tau=\tau_1^{\mathrm{b}}} + J_{\tau_2^{\mathrm{b}}\tau_2^{\mathrm{b}}} \boldsymbol{\Lambda}_\tau \boldsymbol{\Lambda}_\tau^{\mathrm{T}}|_{\tau=\tau_2^{\mathrm{b}}}. \end{aligned} \tag{B.4}$$

Appendix C

RIS-aided localization FIM elements and transformation matrix derivations

C.1 Derivation of FIM elements

In order to find the scalar elements in (5.17) through (5.23), the following derivatives are calculated.

$$
\begin{aligned}
\frac{\partial \boldsymbol{\mu}}{\partial \tau_{\mathrm{g}}} &= \kappa(-jF[n])\beta_{\mathrm{g}}\boldsymbol{h}_{\mathrm{g}}^{\mathrm{T}}\Omega_{\mathrm{g}}\boldsymbol{g}_{\mathbf{g}}e^{-j\tau_{\mathrm{g}}F[n]}s[n],\ g \in \{0, 1, ..., G\} \\
\frac{\partial \boldsymbol{\mu}}{\partial \phi_{\mathrm{az}_{\mathrm{g}}}} &= \kappa\beta_{\mathrm{g}}\boldsymbol{h'}_{\mathbf{1}\mathrm{g}}^{\mathrm{T}}\Omega_{\mathrm{g}}\boldsymbol{g}_{\mathbf{g}}e^{-j\tau_{\mathrm{g}}F[n]}s[n],\ g \in \{1, ..., G\} \\
\frac{\partial \boldsymbol{\mu}}{\partial \phi_{\mathrm{el}_{\mathrm{g}}}} &= \kappa\beta_{\mathrm{g}}\boldsymbol{h'}_{\mathbf{2}\mathrm{g}}^{\mathrm{T}}\Omega_{\mathrm{g}}\boldsymbol{g}_{\mathbf{g}}e^{-j\tau_{\mathrm{g}}F[n]}s[n],\ g \in \{1, ..., G\}
\end{aligned}
$$

$$\begin{aligned}
\frac{\partial \boldsymbol{\mu}}{\partial \beta_{\mathrm{R_g}}} &= \kappa \boldsymbol{h}_{\mathrm{g}}^{\mathrm{T}} \Omega_{\mathrm{g}} \boldsymbol{g}_{\mathbf{g}} e^{-j\tau_{\mathrm{g}} F[n]} s[n],\ g \in \{0, 1, ..., G\} \\
\frac{\partial \boldsymbol{\mu}}{\partial \beta_{\mathrm{I_g}}} &= j\kappa \boldsymbol{h}_{\mathrm{g}}^{\mathrm{T}} \Omega_{\mathrm{g}} \boldsymbol{g}_{\mathbf{g}} e^{-j\tau_{\mathrm{g}} F[n]} s[n],\ g \in \{0, 1, ..., G\} \\
\frac{\partial \boldsymbol{\mu}}{\partial \kappa} &= \sum_{g=0}^{G} \beta_{\mathrm{g}} \boldsymbol{h}_{\mathrm{g}}^{\mathrm{T}} \Omega_{\mathrm{g}} \boldsymbol{g}_{\mathbf{g}} e^{-j\tau_{\mathrm{g}} F[n]} s[n], \\
\frac{\partial \sigma_{\mathrm{w}}^2}{\partial \beta_{\mathrm{R_g}}} &= 2E(1-\kappa^2)\beta_{\mathrm{R_g}},\ g \in \{0, 1, ..., G\} \\
\frac{\partial \sigma_{\mathrm{w}}^2}{\partial \beta_{\mathrm{I_g}}} &= 2E(1-\kappa^2)\beta_{\mathrm{I_g}},\ g \in \{0, 1, ..., G\} \\
\frac{\partial \sigma_{\mathrm{w}}^2}{\partial \kappa} &= -2E\kappa \sum_{g=0}^{G} |\beta_{\mathrm{g}}|^2,
\end{aligned}$$

where,

$$\begin{aligned}
\boldsymbol{h'_1}_{\mathrm{g}} &= \frac{\partial \boldsymbol{h_g}}{\partial \phi_{\mathrm{az_g}}}, \\
\boldsymbol{h'_2}_{\mathrm{g}} &= \frac{\partial \boldsymbol{h_g}}{\partial \phi_{\mathrm{el_g}}},
\end{aligned}$$

defining

$$\begin{aligned}
\gamma_0 &\triangleq \frac{2E}{\sigma_{\mathrm{w}}^2}, \\
\delta &\triangleq \tau_{\mathrm{g'}} - \tau_{\mathrm{g}}, \\
\mathrm{S}\Delta_0(\delta) &\triangleq \sum_{n=-N/2}^{N/2} e^{-j(\delta)F[n]}, \\
\mathrm{S}\Delta_1(\delta) &\triangleq \sum_{n=-N/2}^{N/2} F[n] e^{-j(\delta)F[n]},
\end{aligned}$$

$$\mathrm{S}\Delta_2(\delta) \triangleq \sum_{n=-N/2}^{N/2} F^2[n] e^{-j(\delta)F[n]},$$

the derived fisher information for the interaction between the g'^{th} and g^{th} paths are given below,

$$\begin{aligned}
J_{\tau_{\mathrm{g}}\tau_{\mathrm{g}'}} &= \gamma_0\kappa^2\Re\left\{\beta^*_{\mathrm{g}}\beta_{\mathrm{g}'}\mathrm{S}\Delta_2(\delta)(\boldsymbol{h}^{\mathrm{T}}_{\mathrm{g}}\Omega_{\mathrm{g}}\boldsymbol{g}_{\mathbf{g}})^{\mathrm{H}}(\boldsymbol{h}^{\mathrm{T}}_{\mathrm{g}'}\Omega_{\mathrm{g}'}\boldsymbol{g}_{\mathbf{g'}})\right\}, \\
J_{\tau_{\mathrm{g}}\phi_{\mathrm{az}_{\mathrm{g}'}}} &= -\gamma_0\kappa^2\Im\left\{\beta^*_{\mathrm{g}}\beta_{\mathrm{g}'}\mathrm{S}\Delta_1(\delta)(\boldsymbol{h}^{\mathrm{T}}_{\mathrm{g}}\Omega_{\mathrm{g}}\boldsymbol{g}_{\mathbf{g}})^{\mathrm{H}}(\boldsymbol{h}'^{\mathrm{T}}_{\mathbf{1}\mathrm{g}'}\Omega_{\mathrm{g}'}\boldsymbol{g}_{\mathbf{g'}})\right\}, \\
J_{\tau_{\mathrm{g}}\phi_{\mathrm{el}_{\mathrm{g}'}}} &= -\gamma_0\kappa^2\Im\left\{\beta^*_{\mathrm{g}}\beta_{\mathrm{g}'}\mathrm{S}\Delta_1(\delta)(\boldsymbol{h}^{\mathrm{T}}_{\mathrm{g}}\Omega_{\mathrm{g}}\boldsymbol{g}_{\mathbf{g}})^{\mathrm{H}}(\boldsymbol{h}'^{\mathrm{T}}_{\mathbf{2}\mathrm{g}'}\Omega_{\mathrm{g}'}\boldsymbol{g}_{\mathbf{g'}})\right\}, \\
J_{\tau_{\mathrm{g}}\beta_{\mathrm{R}_{\mathrm{g}'}}} &= -\gamma_0\kappa^2\Im\left\{\beta^*_{\mathrm{g}}\mathrm{S}\Delta_1(\delta)(\boldsymbol{h}^{\mathrm{T}}_{\mathrm{g}}\Omega_{\mathrm{g}}\boldsymbol{g}_{\mathbf{g}})^{\mathrm{H}}(\boldsymbol{h}^{\mathrm{T}}_{\mathrm{g}'}\Omega_{\mathrm{g}'}\boldsymbol{g}_{\mathbf{g'}})\right\}, \\
J_{\tau_{\mathrm{g}}\beta_{\mathrm{I}_{\mathrm{g}'}}} &= -\gamma_0\kappa^2\Re\left\{\beta^*_{\mathrm{g}}\mathrm{S}\Delta_1(\delta)(\boldsymbol{h}^{\mathrm{T}}_{\mathrm{g}}\Omega_{\mathrm{g}}\boldsymbol{g}_{\mathbf{g}})^{\mathrm{H}}(\boldsymbol{h}^{\mathrm{T}}_{\mathrm{g}'}\Omega_{\mathrm{g}'}\boldsymbol{g}_{\mathbf{g'}})\right\}, \\
J_{\tau_{\mathrm{g}}\kappa} &= -\gamma_0\kappa\Im\left\{\beta^*_{\mathrm{g}}(\boldsymbol{h}^{\mathrm{T}}_{\mathrm{g}}\Omega_{\mathrm{g}}\boldsymbol{g}_{\mathbf{g}})^{\mathrm{H}}\sum_{g'=0}^{G}\beta_{\mathrm{g}'}\mathrm{S}\Delta_1(\delta)(\boldsymbol{h}^{\mathrm{T}}_{\mathrm{g}'}\Omega_{\mathrm{g}'}\boldsymbol{g}_{\mathbf{g'}})\right\}, \\
J_{\phi_{\mathrm{az}_{\mathrm{g}}}\phi_{\mathrm{az}_{\mathrm{g}'}}} &= \gamma_0\kappa^2\Re\left\{\beta^*_{\mathrm{g}}\beta_{\mathrm{g}'}\mathrm{S}\Delta_0(\delta)(\boldsymbol{h}'^{\mathrm{T}}_{\mathbf{1}\mathrm{g}}\Omega_{\mathrm{g}}\boldsymbol{g}_{\mathbf{g}})^{\mathrm{H}}(\boldsymbol{h}'^{\mathrm{T}}_{\mathbf{1}\mathrm{g}'}\Omega_{\mathrm{g}'}\boldsymbol{g}_{\mathbf{g'}})\right\}, \\
J_{\phi_{\mathrm{az}_{\mathrm{g}}}\phi_{\mathrm{el}_{\mathrm{g}'}}} &= \gamma_0\kappa^2\Re\left\{\beta^*_{\mathrm{g}}\beta_{\mathrm{g}'}\mathrm{S}\Delta_0(\delta)(\boldsymbol{h}'^{\mathrm{T}}_{\mathbf{1}\mathrm{g}}\Omega_{\mathrm{g}}\boldsymbol{g}_{\mathbf{g}})^{\mathrm{H}}(\boldsymbol{h}'^{\mathrm{T}}_{\mathbf{2}\mathrm{g}'}\Omega_{\mathrm{g}'}\boldsymbol{g}_{\mathbf{g'}})\right\}, \\
J_{\beta_{\mathrm{R}_{\mathrm{g}}}\phi_{\mathrm{az}_{\mathrm{g}'}}} &= \gamma_0\kappa^2\Re\left\{\beta_{\mathrm{g}'}\mathrm{S}\Delta_0(\delta)(\boldsymbol{h}^{\mathrm{T}}_{\mathrm{g}}\Omega_{\mathrm{g}}\boldsymbol{g}_{\mathbf{g}})^{\mathrm{H}}(\boldsymbol{h}'^{\mathrm{T}}_{\mathbf{1}\mathrm{g}'}\Omega_{\mathrm{g}'}\boldsymbol{g}_{\mathbf{g'}})\right\}, \\
J_{\beta_{\mathrm{I}_{\mathrm{g}}}\phi_{\mathrm{az}_{\mathrm{g}'}}} &= \gamma_0\kappa^2\Im\left\{\beta_{\mathrm{g}'}\mathrm{S}\Delta_0(\delta)(\boldsymbol{h}^{\mathrm{T}}_{\mathrm{g}}\Omega_{\mathrm{g}}\boldsymbol{g}_{\mathbf{g}})^{\mathrm{H}}(\boldsymbol{h}'^{\mathrm{T}}_{\mathbf{1}\mathrm{g}'}\Omega_{\mathrm{g}'}\boldsymbol{g}_{\mathbf{g'}})\right\}, \\
J_{\phi_{\mathrm{az}_{\mathrm{g}}}\kappa} &= \gamma_0\kappa\Re\left\{\beta^*_{\mathrm{g}}(\boldsymbol{h}'^{\mathrm{T}}_{\mathbf{1}\mathrm{g}}\Omega_{\mathrm{g}}\boldsymbol{g}_{\mathbf{g}})^{\mathrm{H}}\sum_{g'=0}^{G}\beta_{\mathrm{g}'}\mathrm{S}\Delta_0(\delta)(\boldsymbol{h}^{\mathrm{T}}_{\mathrm{g}'}\Omega_{\mathrm{g}'}\boldsymbol{g}_{\mathbf{g'}})\right\}, \\
J_{\phi_{\mathrm{el}_{\mathrm{g}}}\phi_{\mathrm{el}_{\mathrm{g}'}}} &= \gamma_0\kappa^2\Re\left\{\beta^*_{\mathrm{g}}\beta_{\mathrm{g}'}\mathrm{S}\Delta_0(\delta)(\boldsymbol{h}'^{\mathrm{T}}_{\mathbf{2}\mathrm{g}}\Omega_{\mathrm{g}}\boldsymbol{g}_{\mathbf{g}})^{\mathrm{H}}(\boldsymbol{h}'^{\mathrm{T}}_{\mathbf{2}\mathrm{g}'}\Omega_{\mathrm{g}'}\boldsymbol{g}_{\mathbf{g'}})\right\}, \\
J_{\beta_{\mathrm{R}_{\mathrm{g}}}\phi_{\mathrm{el}_{\mathrm{g}'}}} &= \gamma_0\kappa^2\Re\left\{\beta_{\mathrm{g}'}\mathrm{S}\Delta_0(\delta)(\boldsymbol{h}^{\mathrm{T}}_{\mathrm{g}}\Omega_{\mathrm{g}}\boldsymbol{g}_{\mathbf{g}})^{\mathrm{H}}(\boldsymbol{h}'^{\mathrm{T}}_{\mathbf{2}\mathrm{g}'}\Omega_{\mathrm{g}'}\boldsymbol{g}_{\mathbf{g'}})\right\}, \\
J_{\beta_{\mathrm{I}_{\mathrm{g}}}\phi_{\mathrm{el}_{\mathrm{g}'}}} &= \gamma_0\kappa^2\Im\left\{\beta_{\mathrm{g}'}\mathrm{S}\Delta_0(\delta)(\boldsymbol{h}^{\mathrm{T}}_{\mathrm{g}}\Omega_{\mathrm{g}}\boldsymbol{g}_{\mathbf{g}})^{\mathrm{H}}(\boldsymbol{h}'^{\mathrm{T}}_{\mathbf{2}\mathrm{g}'}\Omega_{\mathrm{g}'}\boldsymbol{g}_{\mathbf{g'}})\right\},
\end{aligned}$$

$$
\begin{aligned}
J_{\phi_{\mathrm{el_g}}\kappa} &= \gamma_0\kappa\Re\left\{\beta_{\mathrm{g}}^{*}(\boldsymbol{h'_2}_{\mathrm{g}}^{\mathrm{T}}\Omega_{\mathrm{g}}\boldsymbol{g}_{\mathbf{g}})^{\mathrm{H}}\sum_{g'=0}^{G}\beta_{\mathrm{g'}}\mathrm{S}\Delta_0(\delta)(\boldsymbol{h}_{\mathrm{g'}}^{\mathrm{T}}\Omega_{\mathrm{g'}}\boldsymbol{g}_{\mathbf{g'}})\right\},\\
J_{\beta_{\mathrm{R_g}}\beta_{\mathrm{R_{g'}}}} &= (N+1)\gamma_0^2(1-\kappa^2)^2\beta_{\mathrm{R_g}}\beta_{\mathrm{R_{g'}}} + \gamma_0\kappa^2\Re\left\{\mathrm{S}\Delta_0(\delta)(\boldsymbol{h}_{\mathrm{g}}^{\mathrm{T}}\Omega_{\mathrm{g}}\boldsymbol{g}_{\mathbf{g}})^{\mathrm{H}}(\boldsymbol{h}_{\mathrm{g'}}^{\mathrm{T}}\Omega_{\mathrm{g'}}\boldsymbol{g}_{\mathbf{g'}})\right\},\\
J_{\beta_{\mathrm{R_g}}\beta_{\mathrm{I_{g'}}}} &= (N+1)\gamma_0^2(1-\kappa^2)^2\beta_{\mathrm{R_g}}\beta_{\mathrm{I_{g'}}} - \gamma_0\kappa^2\Im\left\{\mathrm{S}\Delta_0(\delta)(\boldsymbol{h}_{\mathrm{g}}^{\mathrm{T}}\Omega_{\mathrm{g}}\boldsymbol{g}_{\mathbf{g}})^{\mathrm{H}}(\boldsymbol{h}_{\mathrm{g'}}^{\mathrm{T}}\Omega_{\mathrm{g'}}\boldsymbol{g}_{\mathbf{g'}})\right\},\\
J_{\beta_{\mathrm{R_g}}\kappa} &= -(N+1)\gamma_0^2\kappa(1-\kappa^2)\beta_{\mathrm{R_g}}\sum_{g'=0}^{G}|\beta_{\mathrm{g'}}|^2 + \gamma_0\kappa\Re\left\{(\boldsymbol{h}_{\mathrm{g}}^{\mathrm{T}}\Omega_{\mathrm{g}}\boldsymbol{g}_{\mathbf{g}})^{\mathrm{H}}\sum_{g'=0}^{G}\beta_{\mathrm{g'}}\mathrm{S}\Delta_0(\delta)(\boldsymbol{h}_{\mathrm{g'}}^{\mathrm{T}}\Omega_{\mathrm{g'}}\boldsymbol{g}_{\mathbf{g'}})\right\},\\
J_{\beta_{\mathrm{I_g}}\beta_{\mathrm{I_{g'}}}} &= (N+1)\gamma_0^2(1-\kappa^2)^2\beta_{\mathrm{I_g}}\beta_{\mathrm{I_{g'}}} + \gamma_0\kappa^2\Re\left\{\mathrm{S}\Delta_0(\delta)(\boldsymbol{h}_{\mathrm{g}}^{\mathrm{T}}\Omega_{\mathrm{g}}\boldsymbol{g}_{\mathbf{g}})^{\mathrm{H}}(\boldsymbol{h}_{\mathrm{g'}}^{\mathrm{T}}\Omega_{\mathrm{g'}}\boldsymbol{g}_{\mathbf{g'}})\right\},\\
J_{\beta_{\mathrm{I_g}}\kappa} &= -(N+1)\gamma_0^2\kappa(1-\kappa^2)\beta_{\mathrm{I_g}}\sum_{g'=0}^{G}|\beta_{\mathrm{g'}}|^2 + \gamma_0\kappa\Im\left\{(\boldsymbol{h}_{\mathrm{g}}^{\mathrm{T}}\Omega_{\mathrm{g}}\boldsymbol{g}_{\mathbf{g}})^{\mathrm{H}}\sum_{g'=0}^{G}\beta_{\mathrm{g'}}\mathrm{S}\Delta_0(\delta)(\boldsymbol{h}_{\mathrm{g'}}^{\mathrm{T}}\Omega_{\mathrm{g'}}\boldsymbol{g}_{\mathbf{g'}})\right\},\\
J_{\kappa\kappa} &= (N+1)\gamma_0^2\kappa^2(\sum_{g=0}^{G}|\beta_{\mathrm{g}}|^2)^2 + \gamma_0\Re\left\{\sum_{g=0}^{G}\sum_{g'=0}^{G}\beta_{\mathrm{g}}^{*}\beta_{\mathrm{g'}}\mathrm{S}\Delta_0(\delta)(\boldsymbol{h}_{\mathrm{g}}^{\mathrm{T}}\Omega_{\mathrm{g}}\boldsymbol{g}_{\mathbf{g}})^{\mathrm{H}}(\boldsymbol{h}_{\mathrm{g'}}^{\mathrm{T}}\Omega_{\mathrm{g'}}\boldsymbol{g}_{\mathbf{g'}})\right\}.
\end{aligned}
$$

For 2D scenario, the terms including ϕ_{el} is not usable.

C.2 Derivation of transformation matrix

According to the provided formula for $\boldsymbol{\tau}$, $\boldsymbol{\phi_{az}}$ and $\boldsymbol{\phi_{el}}$ in the subsection 5.2.1, the following derivatives can be achieved.

$$
\frac{\partial\tau_{\mathrm{g}}}{\partial\boldsymbol{x}} = \frac{1}{c}\begin{cases}\dfrac{\boldsymbol{x}}{\|\boldsymbol{x}\|}, & g=0\\[2ex] \dfrac{\boldsymbol{x}-\boldsymbol{x}_{\mathrm{g}}}{\|\boldsymbol{x}-\boldsymbol{x}_{\mathrm{g}}\|}, & g\neq 0\end{cases} \tag{C.1}
$$

$$\frac{\partial \phi_{\mathrm{az_g}}}{\partial \boldsymbol{x}} = \begin{bmatrix} \frac{-\boldsymbol{s}_{\mathrm{g}}(2)}{\boldsymbol{s}_{\mathrm{g}}^2(1)+\boldsymbol{s}_{\mathrm{g}}^2(2)} \\ \\ \frac{\boldsymbol{s}_{\mathrm{g}}(1)}{\boldsymbol{s}_{\mathrm{g}}^2(1)+\boldsymbol{s}_{\mathrm{g}}^2(2)} \\ \\ 0 \end{bmatrix}, \text{for 2D}$$

$$\frac{\partial \phi_{\mathrm{az_g}}}{\partial \boldsymbol{x}} = \begin{bmatrix} \frac{-\boldsymbol{s}_{\mathrm{g}}(2)}{\boldsymbol{s}_{\mathrm{g}}^2(1)+\boldsymbol{s}_{\mathrm{g}}^2(2)} \\ \\ \frac{\boldsymbol{s}_{\mathrm{g}}(1)}{\boldsymbol{s}_{\mathrm{g}}^2(1)+\boldsymbol{s}_{\mathrm{g}}^2(2)} \end{bmatrix}, \text{for 3D}$$

$$\frac{\partial \phi_{\mathrm{el_g}}}{\partial \boldsymbol{x}} = \frac{1}{\|\boldsymbol{s}_{\mathrm{g}}\|^2 \sqrt{\boldsymbol{s}_{\mathrm{g}}^2(1)+\boldsymbol{s}_{\mathrm{g}}^2(2)}} \begin{bmatrix} \boldsymbol{s}_{\mathrm{g}}(1)\boldsymbol{s}_{\mathrm{g}}(3) \\ \\ \boldsymbol{s}_{\mathrm{g}}(2)\boldsymbol{s}_{\mathrm{g}}(3) \\ \\ -(\boldsymbol{s}_{\mathrm{g}}^2(1)+\boldsymbol{s}_{\mathrm{g}}^2(2)) \end{bmatrix}, \text{for 3D}$$

then,

$$\begin{aligned} \frac{\partial \boldsymbol{\tau}}{\partial \boldsymbol{x}} &= \begin{bmatrix} \frac{\partial \tau_0}{\partial \boldsymbol{x}} & \frac{\partial \tau_1}{\partial \boldsymbol{x}} & \cdots & \frac{\partial \tau_{\mathrm{G}}}{\partial \boldsymbol{x}} \end{bmatrix}, \in \mathbb{R}^{2\times(G+1)} \text{for 2D and } \in \mathbb{R}^{3\times(G+1)} \text{for 3D} \\ \frac{\partial \boldsymbol{\phi_{az_g}}}{\partial \boldsymbol{x}} &= \begin{bmatrix} \frac{\partial \boldsymbol{\phi_{az_1}}}{\partial \boldsymbol{x}} & \cdots & \frac{\partial \boldsymbol{\phi_{az_G}}}{\partial \boldsymbol{x}} \end{bmatrix}, \in \mathbb{R}^{2\times G} \text{for 2D and } \in \mathbb{R}^{3\times G} \text{for 3D} \\ \frac{\partial \boldsymbol{\phi_{el_g}}}{\partial \boldsymbol{x}} &= \begin{bmatrix} \frac{\partial \boldsymbol{\phi_{el_1}}}{\partial \boldsymbol{x}} & \cdots & \frac{\partial \boldsymbol{\phi_{el_G}}}{\partial \boldsymbol{x}} \end{bmatrix}, \in \mathbb{R}^{3\times G} \text{for 3D.} \end{aligned}$$

References

[1] M. Fakharzadeh, M. Nezhad-Ahmadi, B. Biglarbegian, J. Ahmadi-Shokouh, and S. Safavi-Naeini. Cmos phased array transceiver technology for 60 GHz wireless applications. *IEEE Transactions on Antennas and Propagation*, 58(4):1093–1104, April 2010.

[2] Cisco annual internet report (2018–2023) white paper. `https://www.cisco.com/c/en/us/solutions/collateral/executive-perspectives/annual-internet-report/white-paper-c11-741490.html`. Accessed: March. 6, 2020.

[3] Omar El Ayach, Sridhar Rajagopal, Shadi Abu-Surra, Zhouyue Pi, and Robert W. Heath. Spatially sparse precoding in millimeter wave MIMO systems. *IEEE Transactions on Wireless Communications*, 13(3):1499–1513, 2014.

[4] Qian Clara Li, Huaning Niu, Apostolos Tolis Papathanassiou, and Geng Wu. 5G network capacity: Key elements and technologies. *IEEE Vehicular Technology Magazine*, 9(1):71–78, 2014.

[5] Anthony Ngozichukwuka Uwaechia and Nor Muzlifah Mahyuddin. A comprehensive survey on millimeter wave communications for fifth-generation wireless networks: Feasibility and challenges. *IEEE Access*, 8:62367–62414, 2020.

[6] Robert W. Heath, Nuria González-Prelcic, Sundeep Rangan, Wonil Roh, and Akbar M. Sayeed. An overview of signal processing techniques for millimeter wave MIMO systems. *IEEE Journal of Selected Topics in Signal Processing*, 10(3):436–453, 2016.

[7] Zhouyue Pi and Farooq Khan. An introduction to millimeter-wave mobile broadband systems. *IEEE Communications Magazine*, 49(6):101–107, 2011.

[8] Jeffrey G. Andrews, Stefano Buzzi, Wan Choi, Stephen V. Hanly, Angel Lozano, Anthony C. K. Soong, and Jianzhong Charlie Zhang. What will 5G be? *IEEE Journal on Selected Areas in Communications*, 32(6):1065–1082, 2014.

[9] Mustafa Riza Akdeniz, Yuanpeng Liu, Mathew K. Samimi, Shu Sun, Sundeep Rangan, Theodore S. Rappaport, and Elza Erkip. Millimeter wave channel modeling and cellular capacity evaluation. *IEEE Journal on Selected Areas in Communications*, 32(6):1164–1179, 2014.

[10] Linglong Dai, Bichai Wang, Mugen Peng, and Shanzhi Chen. Hybrid precoding-based millimeter-wave massive MIMO-NOMA with simultaneous wireless information and power transfer. *IEEE Journal on Selected Areas in Communications*, 37(1):131–141, 2019.

[11] Xianghao Yu, Juei-Chin Shen, Jun Zhang, and Khaled B. Letaief. Alternating minimization algorithms for hybrid precoding in millimeter wave MIMO systems. *IEEE Journal of Selected Topics in Signal Processing*, 10(3):485–500, 2016.

[12] Xiong Wang, Linghe Kong, Fanxin Kong, Fudong Qiu, Mingyu Xia, Shlomi Arnon, and Guihai Chen. Millimeter wave communication: A comprehensive survey. *IEEE Communications Surveys Tutorials*, 20(3):1616–1653, 2018.

[13] M. Marcus and B. Pattan. Millimeter wave propagation: spectrum management implications. *IEEE Microwave Magazine*, 6(2):54–62, 2005.

[14] Zohair Abu-Shaban. *Towards the Next Generation of Location-Aware Communications*. PhD thesis, The Australian National University, 2018.

[15] A. Shahmansoori, G. E. Garcia, G. Destino, G. Seco-Granados, and H. Wymeersch. Position and orientation estimation through millimeter-wave MIMO in 5G systems. *IEEE Transactions on Wireless Communications*, 17(3):1822–1835, 2018.

[16] A. Guerra, F. Guidi, and D. Dardari. Single-anchor localization and orientation performance limits using massive arrays: MIMO vs. beamforming. *IEEE Transactions on Wireless Communications*, 17(8):5241–5255, 2018.

[17] Z. Abu-Shaban, X. Zhou, T. Abhayapala, G. Seco-Granados, and H. Wymeersch. Error bounds for uplink and downlink 3D localization in 5G millimeter wave systems. *IEEE Transactions on Wireless Communications*, 17(8):4939–4954, Aug 2018.

[18] Xuerong Cui, Thomas Aaron Gulliver, Juan Li, and Hao Zhang. Vehicle positioning using 5G millimeter-wave systems. *IEEE Access*, 4:6964–6973, 2016.

[19] Henk Wymeersch, Gonzalo Seco-Granados, Giuseppe Destino, Davide Dardari, and Fredrik Tufvesson. 5G mmwave positioning for vehicular networks. *IEEE Wireless Communications*, 24(6):80–86, 2017.

[20] Klaus Witrisal, Paul Meissner, Erik Leitinger, Yuan Shen, Carl Gustafson, Fredrik Tufvesson, Katsuyuki Haneda, Davide Dardari, Andreas F. Molisch, Andrea Conti, and Moe Z. Win. High-accuracy localization for assisted living: 5G systems will turn multipath channels from foe to friend. *IEEE Signal Processing Magazine*, 33(2):59–70, 2016.

[21] Congzheng Han, Xiaoyi Zhu, Angela Doufexi, and Taskin Kocak. Location-aided multi-user beamforming for 60 GHz wpan systems. In *2012 IEEE 75th Vehicular Technology Conference (VTC Spring)*, pages 1–5, 2012.

[22] Noman Akbar, Shihao Yan, Nan Yang, and Jinhong Yuan. Mitigating pilot contamination through location-aware pilot assignment in massive MIMO networks. In *2016 IEEE Globecom Workshops (GC Wkshps)*, pages 1–6, 2016.

[23] Juan C. Aviles and Ammar Kouki. Position-aided mm-wave beam training under NLOS conditions. *IEEE Access*, 4:8703–8714, 2016.

[24] C. L. S. Howeth. *History of Communications-Electronics in the United States Navy.* Washington, D.C. Bureau of Ships and Office of Naval History, 1963.

[25] R. J. Danchik. An overview of transit development. *John Hopkins APL Technical Digest*, 19(1):18–26, Nov 1998.

[26] Christopher J. Hegarty and Eric Chatre. Evolution of the global navigation satellite system (GNSS). *Proceedings of the IEEE*, 96(12):1902–1917, 2008.

[27] J.M. Zagami, S.A. Parl, J.J. Bussgang, and K.D. Melillo. Providing universal location services using a wireless E911 location network. *IEEE Communications Magazine*, 36(4):66–71, 1998.

[28] The nations 911 system. https://www.fcc.gov/general/9-1-1-and-e9-1-1-services. The Federal Communications Commission, (Accessed: April 2022).

[29] Rocco Di Taranto, Srikar Muppirisetty, Ronald Raulefs, Dirk Slock, Tommy Svensson, and Henk Wymeersch. Location-aware communications for 5G networks: How location information can improve scalability, latency, and robustness of 5G. *IEEE Signal Processing Magazine*, 31(6):102–112, 2014.

[30] Y. Wang P. Zhang, J. Lu and Q. Wang. Cooperative localization in 5G networks: A survey. *ICT Express*, 3(1):27–32, 2017.

[31] Armin Dammann, Ronald Raulefs, and Siwei Zhang. On prospects of positioning in 5g. In *2015 IEEE International Conference on Communication Workshop (ICCW)*, pages 1207–1213, 2015.

[32] The development of global 5G at Huawei. https://carrier.huawei.com/en/spotlight/5g. (Accessed: April 2022).

[33] Service provider commercial 5G deals at Nokia. https://www.nokia.com/networks/5g/5g-contracts/. (Accessed: April 2022).

[34] Service provider commercial 5G deals at Ericsson. https://www.ericsson.com/en/5g/contracts. (Accessed: April 2022).

[35] Juan C. Aviles and Ammar Kouki. Position-aided mmWave beam training under NLOS conditions. *IEEE Access*, 4:8703–8714, 2016.

[36] Noman Akbar, Shihao Yan, Nan Yang, and Jinhong Yuan. Mitigating pilot contamination through location-aware pilot assignment in massive MIMO networks. In *2016 IEEE Globecom Workshops (GC Wkshps)*, pages 1–6, 2016.

[37] L. Srikar Muppirisetty, Tommy Svensson, and Henk Wymeersch. Spatial wireless channel prediction under location uncertainty. *IEEE Transactions on Wireless Communications*, 15(2):1031–1044, 2016.

[38] Ashraf Tahat, Georges Kaddoum, Siamak Yousefi, Shahrokh Valaee, and Francois Gagnon. A look at the recent wireless positioning techniques with a focus on algorithms for moving receivers. *IEEE Access*, 4:6652–6680, 2016.

[39] Farid Zahid, Nordin Rosdiadee, and Ismail Mahamod. Recent advances in wireless indoor localization techniques and system. *Journal of Computer Networks and Communications*, 2013(1):1–12, 2013.

[40] Yanying Gu, Anthony Lo, and Ignas Niemegeers. A survey of indoor positioning systems for wireless personal networks. *IEEE Communications Surveys Tutorials*, 11(1):13–32, 2009.

[41] Xi Yang, Michail Matthaiou, Jie Yang, Chao-Kai Wen, Feifei Gao, and Shi Jin. Hardware-constrained millimeter-wave systems for 5G: Challenges, opportunities, and solutions. *IEEE Communications Magazine*, 57(1):44–50, 2019.

[42] Xi Yang, Michail Matthaiou, Jie Yang, Chao-Kai Wen, Feifei Gao, and Shi Jin. Hardware-constrained millimeter-wave systems for 5G: Challenges, opportunities, and solutions. *IEEE Communications Magazine*, 57(1):44–50, 2019.

[43] Tim Schenk. *RF Imperfections in High-rate Wireless Systems, Impact and Digital Compensation*. Springer, 2008.

[44] Denis Petrovic, Wolfgang Rave, and Gerhard Fettweis. Effects of phase noise on OFDM systems with and without PLL: Characterization and compensation. *IEEE Transactions on Communications*, 55(8):1607–1616, 2007.

[45] Osama S. Faragallah, Hala S. El-Sayed, and Mohamed G. El-Mashed. Estimation and tracking for millimeter wave MIMO systems under phase noise problem. *IEEE Access*, 8:228009–228023, 2020.

[46] T. Pollet, M. Van Bladel, and M. Moeneclaey. Ber sensitivity of OFDM systems to carrier frequency offset and wiener phase noise. *IEEE Transactions on Communications*, 43(2/3/4):191–193, 1995.

[47] J. Stott. The effects of phase noise in OFDM. *EBU Tech. Rev*, 1998.

[48] H. Steendam, M. Moeneclaey, and H. Sari. The effect of carrier phase jitter on the performance of orthogonal frequency-division multiple-access systems. *IEEE Transactions on Communications*, 46(4):456–459, 1998.

[49] A. Garcia Armada. Understanding the effects of phase noise in orthogonal frequency division multiplexing (OFDM). *IEEE Transactions on Broadcasting*, 47(2):153–159, 2001.

[50] M.S. El-Tanany, Yiyan Wu, and L. Hazy. Analytical modeling and simulation of phase noise interference in OFDM-based digital television terrestrial broadcasting systems. *IEEE Transactions on Broadcasting*, 47(1):20–31, 2001.

[51] E. Costa and S. Pupolin. M-QAM-OFDM system performance in the presence of a nonlinear amplifier and phase noise. *IEEE Transactions on Communications*, 50(3):462–472, 2002.

[52] Songping Wu and Y. Bar-Ness. OFDM systems in the presence of phase noise: consequences and solutions. *IEEE Transactions on Communications*, 52(11):1988–1996, 2004.

[53] P. De Doncker T. Nguyen, J. Louveaux and F. Horlin. Impact of I/Q imbalance on time reversal-based indoor positioning systems. *14th International Conference on Wireless and Mobile Computing, Networking and Communications (WiMob)*, pages 36–41, 2018.

[54] M. Athanassios. *Beamforming: Sensor Signal Processing For Defence Applications.* ser. Communications And Signal Processing. World Scientific Publishing Company, 2015.

[55] N. Fistas and A. Manikas. A new general global array calibration method. In *Proceedings of ICASSP '94. IEEE International Conference on Acoustics, Speech and Signal Processing*, volume iv, pages IV/73–IV/76 vol.4, 1994.

[56] Christoph F. Mecklenbrauker, Andreas F. Molisch, Johan Karedal, Fredrik Tufvesson, Alexander Paier, Laura Bernado, Thomas Zemen, Oliver Klemp, and Nicolai Czink. Vehicular channel characterization and its implications for wireless system design and performance. *Proceedings of the IEEE*, 99(7):1189–1212, 2011.

[57] Qingpeng Ma, Gang Qiu, Qixun Zhang, Huiqing Sun, Zhiyong Feng, and Zhu Han. Training sequence based Doppler shift estimation for vehicular communication. In *2020 IEEE Wireless Communications and Networking Conference (WCNC)*, pages 1–6, 2020.

[58] Guanying Liu, An Liu, Rui Zhang, and Minjian Zhao. Angular-domain selective channel tracking and Doppler compensation for high-mobility mmwave massive MIMO. *IEEE Transactions on Wireless Communications*, 20(5):2902–2916, 2021.

[59] Zijun Gong, Cheng Li, Fan Jiang, and Moe Z. Win. Data-aided Doppler compensation for high-speed railway communications over mmwave bands. *IEEE Transactions on Wireless Communications*, 20(1):520–534, 2021.

[60] Z. Abu-Shaban, H. Wymeersch, T. Abhayapala, and G. Seco-Granados. Distributed two-way localization bounds for 5G mmwave systems. In *2018 IEEE Globecom Workshops (GC Wkshps)*, pages 1–6, 2018.

[61] Z. Abu-Shaban, H. Wymeersch, T. Abhayapala, and G. Seco-Granados. Single-anchor two-way localization bounds for 5G mmWave systems. *IEEE Transactions on Vehicular Technology*, 69(6):6388–6400, 2020.

[62] H. Van Trees and K. Bell. *Detection, Estimation, and Modulation Theory, Optimum Array Processing. Part IV.* John Wiley sons, 2011.

[63] A. Manikas. *Differential geometry in array processing.* Imperial College Press, 2004.

[64] C. A. Balanis and P. I. Ioannides. *Introduction to Smart Antennas.* Morgan Claypool, 2007.

[65] Emil Björnson, Jakob Hoydis, and Luca Sanguinetti. Massive MIMO networks: Spectral, energy, and hardware efficiency. *Foundations and Trends in Signal Processing*, 11(3-4):154–655, 2017.

[66] J. J. Bussgang. Crosscorrelation functions of amplitude distorted Gaussian signals. *Tech. rep. Research Laboratory of Electronics, Massachusetts Institute of Technology*, (216), 1952.

[67] S. M. Kay. *Fundamentals of Statistical Signal Processing: Estimation Theory*. Prentice-Hall, NJ, USA, 1993.

[68] H.V. Poor. *An Introduction to Signal Detection and Estimation*. Springer Texts in Electrical Engineering. Springer New York, 2013.

[69] Ertugrul Basar, Marco Di Renzo, Julien De Rosny, Merouane Debbah, Mohamed-Slim Alouini, and Rui Zhang. Wireless communications through reconfigurable intelligent surfaces. *IEEE Access*, 7:116753–116773, 2019.

[70] Qingqing Wu and Rui Zhang. Towards smart and reconfigurable environment: Intelligent reflecting surface aided wireless network. *IEEE Communications Magazine*, 58(1):106–112, 2020.

[71] Ertugrul Basar. Transmission through large intelligent surfaces: A new frontier in wireless communications. *Available: https://arxiv.org/abs/1902.08463*, 2019.

[72] Robert C. Daniels Theodore S. Rappaport, Robert W. Heath Jr. and James N. Murdock. *Millimeter Wave Wireless Communications*. Englewood Cliffs, NJ, USA: Prentice-Hall, 2015.

[73] R. W. Heath, N. González-Prelcic, S. Rangan, W. Roh, and A. M. Sayeed. An overview of signal processing techniques for millimeter wave MIMO systems. *IEEE Journal of Selected Topics in Signal Processing*, 10(3):436–453, April 2016.

[74] Ericsson. `https://www.ericsson.com/en/5g/use-cases`. Accessed: Dec. 6, 2018.

[75] H. Kim, H. Wymeersch, N. Garcia, G. Seco-Granados, and S. Kim. 5G mmWave vehicular tracking. *52nd Asilomar Conference on Signals, Systems, and Computers*, pages 541–547, 2018.

[76] N. Garcia, H. Wymeersch, E. G. Ström, and D. Slock. Location-aided mmWave channel estimation for vehicular communication. In *2016 IEEE 17th International Workshop on Signal Processing Advances in Wireless Communications (SPAWC)*, pages 1–5, 2016.

[77] M. D. Larsen, A. L. Swindlehurst, and T. Svantesson. Performance bounds for MIMO-OFDM channel estimation. *IEEE Transactions on Signal Processing*, 57(5):1901–1916, 2009.

[78] Y. Shen, H. Wymeersch, and M. Z. Win. Fundamental limits of wideband localization— part II: Cooperative networks. *IEEE Transactions on Information Theory*, 56(10):4981–5000, 2010.

[79] O. Kolawole, A. Papazafeiropoulos, and T. Ratnarajah. Impact of hardware impairments on mmwave MIMO systems with hybrid precoding. In *2018 IEEE Wireless Communications and Networking Conference (WCNC)*, pages 1–6, 2018.

[80] H. Shen, W. Xu, S. Gong, C. Zhao, and D. W. K. Ng. Beamforming optimization for IRS-aided communications with transceiver hardware impairments. *IEEE Transactions on Communications*, pages 1–1, 2020.

[81] M. Li, B. Selim, S. Muhaidat, P. C. Sofotasios, M. Dianati, P. D. Yoo, J. Liang, and A. Wang. Effects of residual hardware impairments on secure NOMA-based cooperative systems. *IEEE Access*, 8:2524–2536, 2020.

[82] Y. Wu, Y. Gu, and Z. Wang. Efficient channel estimation for mmWave MIMO with transceiver hardware impairments. *IEEE Transactions on Vehicular Technology*, 68(10):9883–9895, 2019.

[83] F. Ghaseminajm, Z. Abu-Shaban, S. S. Ikki, H. Wymeersch, and C. R. Benson. Localization error bounds for 5G mmwave systems under I/Q imbalance. *IEEE Transactions on Vehicular Technology*, pages 1–1, 2020.

[84] P. J. Schreier and L. L. Scharf. *Statistical Signal Processing of Complex-Valued Data*. Cambridge University Press, 2010.

[85] Y. Shen and M. Z. Win. Fundamental limits of wideband localization— part I: A general framework. *IEEE Transactions on Information Theory*, 56(10):4956–4980, Oct 2010.

[86] Mohd Hamza Naim Shaikh, Vivek Ashok Bohara, Anand Srivastava, and Gourab Ghatak. Performance analysis of intelligent reflecting surface-assisted wireless system with non-ideal transceiver. *IEEE Open Journal of the Communications Society*, 2:671–686, 2021.

[87] Rocco Di Taranto, Srikar Muppirisetty, Ronald Raulefs, Dirk Slock, Tommy Svensson, and Henk Wymeersch. Location-aware communications for 5G networks: How location information can improve scalability, latency, and robustness of 5G. *IEEE Signal Processing Magazine*, 31(6):102–112, 2014.

[88] Yuan Shen and Moe Z. Win. Performance of localization and orientation using wideband antenna arrays. In *2007 IEEE International Conference on Ultra-Wideband*, pages 288–293, 2007.

[89] Yuan Shen and Moe Z. Win. On the accuracy of localization systems using wideband antenna arrays. *IEEE Transactions on Communications*, 58(1):270–280, 2010.

[90] Yuan Shen and Moe Z. Win. Fundamental limits of wideband localization— part I: A general framework. *IEEE Transactions on Information Theory*, 56(10):4956–4980, 2010.

[91] Yuan Shen, Henk Wymeersch, and Moe Z. Win. Fundamental limits of wideband localization— part II: Cooperative networks. *IEEE Transactions on Information Theory*, 56(10):4981–5000, 2010.

[92] Donglin Wang, Michel Fattouche, and Fadhel M. Ghannouchi. Bounds of mmwave-based ranging and positioning in multipath channels. In *2017 IEEE Globecom Workshops (GC Wkshps)*, pages 1–6, 2017.

[93] Yue Wu, Yuantao Gu, and Zhaocheng Wang. Channel estimation for mmWave MIMO with transmitter hardware impairments. *IEEE Communications Letters*, 22(2):320–323, 2018.

[94] Nebojsa Maletic, Jesús Gutiérrez-Teran, and Eckhard Grass. Beamforming mmWave MIMO: Impact of nonideal hardware and channel state information. In *2018 26th Telecommunications Forum (TELFOR)*, pages 1–6, 2018.

[95] Anastasios Papazafeiropoulos, Tharmalingam Ratnarajah, Pandelis Kourtessis, and Symeon Chatzinotas. Nuts and bolts of a realistic stochastic geometric analysis of mmWave hetnets: Hardware impairments and channel aging. *IEEE Transactions on Vehicular Technology*, 68(6):5657–5671, 2019.

[96] Kamran Keykhosravi, Musa Furkan Keskin, Satyam Dwivedi, Gonzalo Seco-Granados, and Henk Wymeersch. Semi-passive 3D positioning of multiple RIS-

enabled users. *IEEE Transactions on Vehicular Technology*, 70(10):11073–11077, 2021.

[97] Henk Wymeersch and Benoît Denis. Beyond 5G wireless localization with reconfigurable intelligent surfaces. In *ICC 2020 - 2020 IEEE International Conference on Communications (ICC)*, pages 1–6, 2020.

[98] Kamran Keykhosravi, Musa Furkan Keskin, Gonzalo Seco-Granados, and Henk Wymeersch. SISO RIS-enabled joint 3D downlink localization and synchronization. In *ICC 2021 - IEEE International Conference on Communications*, pages 1–6, 2021.

[99] Ahmed Elzanaty, Anna Guerra, Francesco Guidi, and Mohamed-Slim Alouini. Reconfigurable intelligent surfaces for localization: Position and orientation error bounds. *IEEE Transactions on Signal Processing*, 69:5386–5402, 2021.

[100] Fariba Ghaseminajm, Emad Saleh, Malek Alsmadi, and Salama S. Ikki. Localization error bounds for 5G mmwave systems under hardware impairments. In *2021 IEEE 32nd Annual International Symposium on Personal, Indoor and Mobile Radio Communications (PIMRC)*, pages 1228–1233, 2021.

[101] Anastasios Kakkavas, Mario H. Castañeda García, Gonzalo Seco-Granados, Henk Wymeersch, Richard A. Stirling-Gallacher, and Josef A. Nossek. Position information from reflecting surfaces. *IEEE Wireless Communications Letters*, 10(6):1300–1304, 2021.

[102] Alessio Fascista, Angelo Coluccia, Henk Wymeersch, and Gonzalo Seco-Granados. RIS-aided joint localization and synchronization with a single-antenna mmwave receiver. In *ICASSP 2021 - 2021 IEEE International Conference on Acoustics, Speech and Signal Processing (ICASSP)*, pages 4455–4459, 2021.

[103] Mingan Luan, Bo Wang, Yanping Zhao, Zhiyuan Feng, and Fengye Hu. Phase design and near-filed target localization for RIS-assisted regional localization system. *IEEE Transactions on Vehicular Technology*, pages 1–1, 2021.

[104] Davide Dardari, Nicoló Decarli, Anna Guerra, and Francesco Guidi. LOS/NLOS near-field localization with a large reconfigurable intelligent surface. *IEEE Transactions on Wireless Communications*, pages 1–1, 2021.

[105] Emrah Čišija, Aya Mostafa Ahmed, Aydin Sezgin, and Henk Wymeersch. RIS-aided mmwave MIMO radar system for adaptive multi-target localization. In *2021 IEEE Statistical Signal Processing Workshop (SSP)*, pages 196–200, 2021.

[106] Jiguang He, Henk Wymeersch, Tachporn Sanguanpuak, Olli Silven, and Markku Juntti. Adaptive beamforming design for mmwave RIS-aided joint localization and communication. In *2020 IEEE Wireless Communications and Networking Conference Workshops (WCNCW)*, pages 1–6, 2020.

[107] Yaoshen Cui and Haifan Yin. Channel estimation for RIS-aided mmwave communications via 3D positioning. In *2021 IEEE/CIC International Conference on Communications in China (ICCC Workshops)*, pages 399–404, 2021.

[108] Teng Ma, Yue Xiao, Xia Lei, Wenhui Xiong, and Yuan Ding. Indoor localization with reconfigurable intelligent surface. *IEEE Communications Letters*, 25(1):161–165, 2021.

[109] Henk Wymeersch, Jiguang He, Benoît Denis, Antonio Clemente, and Markku Juntti. Radio localization and mapping with reconfigurable intelligent surfaces. *Available: https://arxiv.org/abs/1912.09401v1*, 2019.

[110] Professor Peter J. Schreier and Professor Louis L. Scharf. *Statistical Signal Processing of Complex-Valued Data: The Theory of Improper and Noncircular Signals.* Cambridge University Press, 2010.

[111] Henk Wymeersch and Benoît Denis. Beyond 5G wireless localization with reconfigurable intelligent surfaces. In *ICC 2020 - 2020 IEEE International Conference on Communications (ICC)*, pages 1–6, 2020.